

MULTISCALE ANALYSES OF INLAND
TROPICAL CYCLONE–MIDLATITUDE JET INTERACTIONS:
CAMILLE (1969) AND DANNY (1997)

by

Matthew S. Potter

Abstract of

A Thesis

Submitted to the University at Albany, State University of New York

in Partial Fulfillment of

the Requirements for the Degree of

Master of Science

College of Arts & Sciences

Department of Atmospheric and Environmental Sciences

2012

ABSTRACT

TC Camille (1969) and TC Danny (1997) both interacted with the equatorward entrance region of an upper-tropospheric jet as they traversed the Appalachian Mountains; however, their societal impacts differed. During the 12-h period starting 0000 UTC 20 August 1969, 690 mm of rain fell over Massies Mill, Virginia, as TC Camille traversed the central Appalachian Mountains. On 24 July 1997, TC Danny underwent inland reintensification while moving across the Carolinas. TC Danny's minimum central mean sea level pressure decreased from 1012 hPa to 1000 hPa and its maximum sustained wind speed increased from 20 kt to 40 kt during the 18-h period starting 0000 UTC 24 July. The main objectives of this thesis are to document the synoptic-scale environments and underlying mesoscale processes responsible for each TC–jet interaction, and to document important mechanisms and processes that lead to inland flooding associated with TC–jet interactions and inland reintensifying TCs that interact with midlatitude jets.

Multiscale analyses are conducted using ERA-40 and the NCEP CFSR (Climate Forecast System Reanalysis) global gridded datasets, available at 1.125° and 0.5° resolution, for the TC Camille and TC Danny cases. Surface analyses are employed to identify and document the surface environment and significant mesoscale features associated with both storms. Radar data are used to supplement the mesoscale analysis of each case, and a potential vorticity (PV) perspective is employed to facilitate the interpretation of the multiscale analyses.

The multiscale analyses reveal that unlike the TC Camille case, synoptic-scale ascent arising from implied positive PV advection and minimized effects of vertical wind

shear associated with an upper-tropospheric positive PV anomaly enabled TC Danny to intensify inland. Frontogenetically forced ascent along a lower-tropospheric baroclinic zone and orographic enhancement of rainfall, induced by moist, upslope flow across the Blue Ridge Mountains, were the main contributors to the inland flooding associated with TC Camille. Convection that induced diabatically driven cyclonic relative vorticity and PV increases below the level of maximum diabatic heating at midlevels near the center of TC Danny strengthened the TC's circulation and led to its inland reintensification. The tropospheric features and processes for each case are graphically represented in conceptual models that forecasters can utilize when predicting the impacts associated with inland TC–jet interactions.

MULTISCALE ANALYSES OF INLAND
TROPICAL CYCLONE–MIDLATITUDE JET INTERACTIONS:
CAMILLE (1969) AND DANNY (1997)

by

Matthew S. Potter

A Thesis

Submitted to the University at Albany, State University of New York

in Partial Fulfillment of

the Requirements for the Degree of

Master of Science

College of Arts & Sciences

Department of Atmospheric and Environmental Sciences

2012

ACKNOWLEDGEMENTS

First, and foremost, I want to thank my family for their support throughout my two years of graduate school. I am truly blessed to have such a strong support system around me. I am forever grateful for my best friend Mel being with me every step of the way; her love, support, and comfort has always kept me positive.

I would like to thank my advisors, Dr. Lance Bosart and Dr. Daniel Keyser, for their guidance throughout the course of this research and giving me the tools for being a better professional and scientist. Many thanks goes out to previous Department of Atmospheric and Environmental Sciences (DAES) graduate students Heather Archambault, Jay Cordeira, Nick Metz, and Alan Srock for providing useful scripts and insight which benefited my research. I am very thankful for the assistance from Matt Janiga, who produced the reanalysis data files used in my TC Camille analysis and for giving me scripts to perform my diabatic heating analysis. My sincerest gratitude goes out to Kyle Griffin for answering all of my GEMPAK questions. I would like to thank my fellow colleagues, Chris Castellano and Dan Thompson, for their friendship and support. Thanks go to Kevin Tyle and David Knight for assisting with technical issues. I would also like to thank Barbara Zampella, Patty Seguin, and Maria Moon for their administrative assistance. Lastly, I want to acknowledge all the other DAES faculty and graduates students for making my two years at Albany an enjoyable experience.

This research was supported by the UCAR–NCEP (University Corporation for Atmospheric Research–National Centers for Environmental Prediction) Grant S1071092, and conducted under the umbrella of the CSTAR (Collaborative Science, Technology, and Applied Research) program.

TABLE OF CONTENTS

Abstract.....	ii
Acknowledgements.....	v
Table of Contents.....	vi
List of Tables.....	viii
List of Figures.....	ix
1. Introduction.....	1
1.1 General Purpose.....	1
1.2 Motivation and Overview.....	2
1.3 Interactions between TCs and Midlatitude Troughs and Jets.....	3
1.3.1 ET of TCs.....	3
1.3.2 Intensification Changes of TCs.....	6
1.3.3 Inland Flooding Associated with TCs.....	8
1.4 Documented Cases of Inland Reintensifying TCs.....	10
1.5 Goals and Organization of the Thesis.....	12
2. Data and Methodology.....	22
2.1 List of Inland Reintensifying TCs.....	22
2.2 Multiscale Analyses.....	24
3. TC Camille Multiscale Analysis.....	31
3.1 Introduction.....	31
3.1.1 TC Track.....	31
3.1.2 Inland Impacts.....	32
3.2 Synoptic Overview.....	32
3.2.1 Large-Scale Evolution.....	32
3.2.2 PV Analysis.....	34
3.2.3 Low-Level Structure and Moisture Evolution.....	37
3.3 Mesoscale Overview.....	40
3.3.1 Precipitation Evolution.....	40
3.3.2 Surface Analysis.....	42
3.3.3 Frontogenesis and Ageostrophic Circulation Analysis.....	44
3.4 Summary.....	45
4. TC Danny Multiscale Analysis.....	64
4.1 Introduction.....	64
4.1.1 TC Track.....	64
4.1.2 Inland Impacts.....	65
4.1.3 Historical Perspective.....	66

4.2 Synoptic Overview.....	67
4.2.1 Large-Scale Evolution.....	67
4.2.2 Satellite and Radar Observations.....	71
4.2.2.1 Satellite Observations.....	71
4.2.2.2 Radar Observations.....	71
4.2.2 PV Analysis.....	72
4.2.3 Low-Level Structure and Moisture Evolution.....	77
4.3 Mesoscale Overview.....	79
4.3.1 Precipitation Evolution.....	79
4.3.2 Diabatic Heating Analysis.....	82
4.3.3 Surface Analysis.....	84
4.3.4 Frontogenesis and Ageostrophic Circulation Analysis.....	86
4.4 Summary.....	88
5. Discussion, Conclusions, and Suggestions for Future Work.....	119
5.1 Discussion of Multiscale Analyses.....	119
5.2 Conclusions.....	126
5.3 Suggestions for Future Work.....	128
References.....	133

LIST OF TABLES

Table I: The 27 TC candidate cases during 1950–2010.

Table II: The 10 inland reintensifying TCs during 1950–2010. The second column identifies the state(s) over which each reintensification event took place. The third column identifies whether each respective TC was beneath the equatorward entrance region of an upper-tropospheric jet. The fourth and fifth columns document the observed increase in maximum sustained wind speed and decrease in central minimum MSLP, respectively, at the end of each TC's inland reintensification period.

LIST OF FIGURES

Fig. 1.1. Conceptual model of transformation stage of ET in the western North Pacific, with labeled areas as follows: 1) environmental equatorward flow of cooler, drier air (with corresponding open cell cumulus); 2) decreased TC convection in the western quadrant (with corresponding dry slot) in step 1, which extends throughout the southern quadrant in steps 2 and 3; 3) environmental poleward flow of warm, moist air is ingested into TC circulation, which maintains convection in the eastern quadrant and results in an asymmetric distribution of clouds and precipitation in steps 1 and 2; steps 2 and 3 also feature a southerly jet that ascends tilted isentropic surfaces; 4) ascent of warm, moist inflow over tilted isentropic surfaces associated with baroclinic zone (dashed line) in middle and lower panels; 5) ascent (undercut by dry-adiabatic descent) that produces cloudbands wrapping westward and equatorward around the storm center; dry-adiabatic descent occurs close enough to the circulation center to produce erosion of eyewall convection in step 3; 6) cirrus shield with a sharp cloud edge if confluent with polar jet. Caption and figure reproduced from Fig. 5 in Klein et al. (2000).

Fig. 1.2. Composite 500-hPa height (m) and sea level pressure (hPa, only below 1008 hPa with shading in 4-hPa increments starting at 1004 hPa) analyses based on grouping of cases in a northwest pattern at the (a) ET time, (b) ET + 24 h, and in a northeast pattern at the (c) ET time and (d) ET + 24 h. The composite northwest pattern is based on 13 cases and the northeast pattern is based in 17 cases. Caption and figure reproduced from Fig. 1 in Harr et al. (2000).

Fig. 1.3. Schematic representation of upper-tropospheric ridge amplification and jet streak intensification associated with divergent TC outflow impinging upon an upper-tropospheric jet stream (i.e., a meridional PV gradient). Caption and figure reproduced from Fig. 2.6 in Archambault (2011).

Fig. 1.4. (a) Schematic of transverse ageostrophic wind components and patterns of divergence associated with the entrance and exit regions of a straight jet streak [after Bjerknes (1951)]. (b) Vertical cross sections illustrating direct and indirect circulations in the entrance region [along dotted line labeled A–A' in (a)] and exit region [along dotted line labeled B–B' in (a)] of a jet streak. Cross sections include two representative isentropes (dotted), upper-level jet location (marked by a J), relative positions of cold and warm air, upper-level divergence, horizontal ageostrophic components, and vertical motion (arrows) within the plane of each cross section. (c) Schematic of maximum (cyclonic) and minimum (anticyclone) relative vorticity centers and associated advection patterns associated with a straight jet streak. (NVA represents negative or anticyclonic vorticity advection; PVA represents positive or cyclonic vorticity advection.) Caption and figure reproduced from Fig. 3 in Uccellini and Kocin (1987).

Fig. 1.5. (a) Eddy momentum flux at the 1500 km radius, plotted only for those times in which the storm remained over water 30 h later. (b) Deepening rate of the storm at times 30 h after those of part (a). Caption and figure reproduced from Fig. 4 in Molinari and Vollaro (1989).

Fig. 1.6. Horizontal plot on the 200-hPa surface for the favorable distant interaction composite containing cases with a total δp of more than 10 hPa. (a), (c), and (e) Vectors of the total wind [m s^{-1} , reference arrow indicated at bottom left of (e)] and Ertel PV (increment is 0.5 PVU and values greater than 1.5 PVU are shaded as indicated) at times $t_0 - 12$ h, t_0 , and $t_0 + 12$ h, respectively. (b), (d), and (f) Total wind speed (m s^{-1} , values greater than 15 m s^{-1} are shaded as indicated), velocity potential ϕ (solid lines, contour interval $6 \times 10^5 \text{ m}^2; \text{ths}^{-1}$), and divergent wind \mathbf{V}_d [m s^{-1} , reference arrow indicated at bottom left of (f)] at times $t_0 - 12$ h, t_0 , and $t_0 + 12$ h, respectively. Asterisk denotes the location of the composite tropical cyclone center, and the increment in latitude and longitude is 10° . Caption and figure reproduced from Fig. 5 in Hanley et al. (2001).

Fig. 1.7. Schematics for landfalling tropical cyclones for (a) the LOC composite and (b) the ROC composite. The curved black lines represent streamlines of the upper-tropospheric (i.e., 250 hPa) flow. Arrows represent motion and deep tropospheric shear with the relative magnitudes given by the length of the arrow. The curved green line represents the trajectory of a parcel starting near the surface in the warm sector and ending in the mid- to upper troposphere in the cool sector. The gray shaded area represents regions of precipitation and pluses and minuses represent the local PV tendency resulting from a combination of advection and the diabatic redistribution of PV. Caption and figure reproduced from Fig. 10 in Atallah et al. (2007).

Fig. 1.8. Schematic cross section of the warm-frontal boundary found in (a) LOT precipitation distribution cases and (b) ROT precipitation distribution cases. Cross section includes frontogenesis shaded in green and vertical velocity dashed contoured in red. Caption and figure reproduced from Fig. 4.3 in Klein (2007).

Fig. 1.9. Conceptual model of the synoptic-scale environment of (a) JR, (b) SJ, and (c) DC category PREs showing 200-hPa geopotential height (solid black contours), 200-hPa wind speed (gray shading; “J” symbol marks the location of maximum wind speed), low-level (i.e., 925-hPa) streamlines (red indicates warm advection, blue indicates cold advection), the low level jet (large red arrow), the low-level baroclinic zone (stationary front symbol), and PW (values > 50 mm shaded in blue). The position of the PRE is indicated by the green shading, the position of the TC is indicated by the tropical storm symbol, and the maxima and minima in low-level geopotential height are indicated by the “H” and “L” symbols, respectively. Caption and figures reproduced from Figs. 6.1, 6.2, and 6.3 in Moore (2010).

Fig. 2.1. Key displaying the symbols used for the adapted radar summary charts.

Fig. 2.2. Vertical cross section of PV (shaded every 1 potential vorticity unit [PVU; $10^{-6} \text{ m}^2 \text{ s}^{-1} \text{ K kg}^{-1}$]), potential temperature (solid black every 4 K), and the wind component normal to the cross section (dashed green every 5 m s^{-1} starting at 15 m s^{-1}) at 1800 UTC 24 July 1997 using the (a) ERA-40 and (b) NCEP CFSR.

Fig. 2.3. A $3^\circ \times 3^\circ$ computational box centered on the central circulation of TC Danny (green TC symbol) at 0600 UTC 24 July 1997.

Fig. 3.1. TC Camille track map displaying maximum sustained wind speed and minimum central MSLP observations at 0000 UTC for 17–22 August 1969. 0000 UTC locations are denoted by yellow circles with a red outline.

Fig. 3.2. Map of 250-hPa wind speed (shaded, m s^{-1}), 1000–500-hPa thickness (dashed red every 2 dam), and MSLP (solid black every 2 hPa) at 0600 UTC 19 August 1969. The green TC symbol denotes the position of TC Camille as depicted by the ERA-40.

Fig. 3.3. Same as Fig. 3.2., except at 1800 UTC 19 August 1969.

Fig. 3.4. Same as Fig. 3.2., except at 0600 UTC 20 August 1969.

Fig. 3.5. Same as Fig. 3.2., except at 1800 UTC 20 August 1969.

Fig. 3.6. (a) Map of potential temperature on the 2 PVU surface (shaded every 5 K; every 10 K below 340 K), 850–200-hPa wind shear (barbs, kt), and 925–850-hPa layer-averaged relative vorticity (solid black every $0.5 \times 10^{-4} \text{ s}^{-1}$ starting at $0.5 \times 10^{-4} \text{ s}^{-1}$) at 0600 UTC 19 August 1969. The yellow star denotes the position of TC Camille as depicted by the ERA-40. The black line denotes the location of the vertical cross section shown in Fig. 3.6b. (b) North–south vertical cross section of PV (shaded every 1 PVU), potential temperature (solid black every 4 K), and horizontal wind speed (dashed green every 5 m s^{-1} starting at 15 m s^{-1}) at 0600 UTC 19 August 1969. The yellow star denotes the location of TC Camille along the cross section.

Fig. 3.7. Same as Fig. 3.6, except at 1800 UTC 19 August 1969. The black line in (a) denotes the location of the vertical cross section shown in Fig. 3.7b.

Fig. 3.8. Same as Fig. 3.6, except at 0600 UTC 20 August 1969. The black line in (a) denotes the location of the vertical cross section shown in Fig. 3.8b.

Fig. 3.9. Same as Fig. 3.6, except at 1800 UTC 20 August 1969. The black line in (a) denotes the location of the vertical cross section shown in Fig. 3.9b.

Fig. 3.10. Map of PW (shaded, mm), 700-hPa vertical motion (light blue contour every $2 \times 10^{-3} \text{ hPa s}^{-1}$, negative values only), 925-hPa geopotential height (solid black every 3 dam), 925-hPa potential temperature (dashed pink every 2 K), and 925-hPa winds (barbs, kt) at 0600 UTC 19 August 1969. The green TC symbol denotes the position of TC Camille as depicted by the ERA-40.

Fig. 3.11. Same as Fig. 3.10, except at 1800 UTC 19 August 1969.

Fig. 3.12. Same as Fig. 3.10, except at 0600 UTC 20 August 1969. The black line denotes the location of the vertical cross section shown in Figs. 3.24–3.26.

Fig. 3.13. Same as Fig. 3.10, except at 1800 UTC 20 August 1969.

Fig. 3.14. Adapted radar summary chart at 2245 UTC 19 August 1969. The yellow star denotes the approximate location of Nelson County, Virginia. The green TC symbol denotes the position of TC Camille as depicted by the ERA-40.

Fig. 3.15. Same as Fig. 3.14, except at 0045 UTC 20 August 1969.

Fig. 3.16. Same as Fig. 3.14, except at 0245 UTC 20 August 1969.

Fig. 3.17. Same as Fig. 3.14, except at 0445 UTC 20 August 1969.

Fig. 3.18. Same as Fig. 3.14, except at 0645 UTC 20 August 1969.

Fig. 3.19. Same as Fig. 3.14, except at 0845 UTC 20 August 1969.

Fig. 3.20. Same as Fig. 3.14, except at 1045 UTC 20 August 1969.

Fig. 3.21. Surface analysis at 0000 UTC 20 August 1969 displaying MSLP (solid black every 2 hPa), wind (barbs, kt), dewpoint (dashed green every 2°C), and temperature (dashed red every 2°C). The yellow star denotes the approximate location of Nelson County, Virginia. The green TC symbol denotes the position of TC Camille as depicted by the ERA-40.

Fig. 3.22. Same as Fig. 3.21, except at 0600 UTC 20 August 1969.

Fig. 3.23. Same as Fig. 3.21, except at 1200 UTC 20 August 1969.

Fig. 3.24. North–south vertical cross section of Petterssen frontogenesis [shaded, $\text{K} (100 \text{ km})^{-1} (3 \text{ h})^{-1}$], potential temperature (solid black every 4 K), vertical motion (dashed red every $2 \times 10^{-3} \text{ hPa s}^{-1}$, negative values only), horizontal wind speed (solid orange every 5 m s^{-1} starting at 15 m s^{-1}) and the ageostrophic wind component tangential to the cross section (arrows, m s^{-1}) at 0000 UTC 20 August 1969. The yellow star denotes the approximate location of Nelson County along the cross section. The location of the vertical cross section is shown in Fig. 3.12.

Fig. 3.25. Same as Fig. 3.24, except at 0600 UTC 20 August 1969.

Fig. 3.26. Same as Fig. 3.24, except at 1200 UTC 20 August 1969.

Fig. 4.1. TC Danny track map displaying maximum sustained wind speed and minimum central MSLP observations at 0000 UTC for 17–27 July 1997. 0000 UTC locations are denoted by yellow circles with a red outline. 1800 UTC 24 July locations is denoted by a blue circle with a red outline.

Fig. 4.2. (a) Map of 250-hPa wind speed (shaded, m s^{-1}), 1000–500-hPa thickness (dashed red every 2 dam), and MSLP (solid black every 2 hPa) at 1800 UTC 22 July 1997. The green TC symbol denotes the location of TC Danny as depicted by the CFSR. (b) Map of 700-hPa vertical motion (shaded, Pa s^{-1}) at 1800 UTC 22 July 1997. The red TC symbol denotes the approximate location of TC Danny [Image produced using the ESRL (Earth System Research Laboratory) 6-h NCEP–NCAR Reanalysis Data Composite page available at <http://www.esrl.noaa.gov/psd/data/composites/hour/>.]

Fig. 4.3. Same as Fig. 4.2, except at 0600 UTC 23 July 1997.

Fig. 4.4. Same as Fig. 4.2, except at 1800 UTC 23 July 1997.

Fig. 4.5. Same as Fig. 4.2, except at 0600 UTC 24 July 1997.

Fig. 4.6. Same as Fig. 4.2, except at 1800 UTC 24 July 1997.

Fig. 4.7. GOES-8 infrared satellite images taken at (a) 2345 UTC 22 July 1997, (b) 1145 UTC 23 July 1997, (c) 2345 UTC 23 July 1997, and (d) 1145 UTC 24 July 1997. The yellow star denotes the approximate location of TC Danny. [Images courtesy of the NCDC GIBBS (Global ISCCP B1 Browse System) page available at <http://www.ncdc.noaa.gov/gibbs/>.]

Fig. 4.8. National radar summary composites (shaded every 5 dBZ) at (a) 0000 UTC 23 July 1997, (b) 1200 UTC 23 July 1997, (c) 0000 UTC 24 July 1997, and (d) 1200 UTC 24 July 1997. The “D” symbol denotes the rainfall region associated with TC Danny. [Images available at <http://www.mmm.ucar.edu/imagearchive/>.]

Fig. 4.9. (a) Map of potential temperature on the 2 PVU surface (shaded every 5 K), 850–200-hPa wind shear (barbs, kt), and 925–850-hPa layer-averaged relative vorticity (solid black every $1 \times 10^{-4} \text{ s}^{-1}$ starting at $1 \times 10^{-4} \text{ s}^{-1}$) at 1800 UTC 22 July 1997. The yellow star denotes the position of TC Danny as depicted by the CFSR. The black line denotes the location of the vertical cross section shown in Fig. 3.9b. (b) North–south vertical cross section of PV (shaded every 1 PVU), potential temperature (solid black every 4 K), and horizontal wind speed (dashed green every 5 m s^{-1} starting at 15 m s^{-1}) at 1800 UTC 22 July 1997. The yellow star denotes the location of TC Danny along the cross section.

Fig. 4.10. Same as Fig. 4.9, except at 0600 UTC 23 July 1997. The black line in (a) denotes the location of the vertical cross section shown in Fig. 4.10b.

Fig. 4.11. Same as Fig. 4.9, except at 1800 UTC 23 July 1997. The black line in (a) denotes the location of the vertical cross section shown in Fig. 4.11b and Fig. 4.33.

Fig. 4.12. Same as Fig. 4.9, except at 0600 UTC 24 July 1997. The black line in (a) denotes the location of the vertical cross section shown in Fig. 4.12b and Fig. 4.34.

Fig. 4.13. Same as Fig. 4.9, except at 1800 UTC 24 July 1997. The black line in (a) denotes the location of the vertical cross section shown in Fig. 4.13b and Fig. 4.35.

Fig. 4.14. Map of PW (shaded, mm), 700-hPa vertical motion (light blue contour every 5×10^{-3} hPa s⁻¹, negative values only), 925-hPa geopotential height (solid black every 3 dam), 925-hPa potential temperature (dashed pink every 2 K), and 925-hPa winds (barbs, kt) at 1800 UTC 22 July 1997. The green TC symbol denotes the position of TC Danny as depicted by the CFSR.

Fig. 4.15. Same as Fig. 4.14, except at 0600 UTC 23 July 1997.

Fig. 4.16. Observed Atlanta, Georgia (KFFC), sounding valid at 1200 UTC 23 July 1997.

Fig. 4.17. Same as Fig. 4.14, except at 1800 UTC 23 July 1997.

Fig. 4.18. Observed Greensboro, North Carolina (KGSO), sounding valid at 0000 UTC 24 July 1997.

Fig. 4.19. Same as Fig. 4.14, except at 0600 UTC 24 July 1997.

Fig. 4.20. Same as Fig. 4.14, except at 1800 UTC 24 July 1997.

Fig. 4.21. (a) WSR-88D 0.5° base reflectivity image from Birmingham, Alabama (KBMX), taken at 0013 UTC 23 July 1997. (b) GOES-8 visible satellite image taken at 2315 UTC 22 July 1997.

Fig. 4.22. (a) WSR-88D 0.5° base reflectivity image from Atlanta, Georgia (KFFC), taken at 1218 UTC 23 July 1997. (b) GOES-8 visible satellite image taken at 1215 UTC 23 July 1997.

Fig. 4.23. (a) WSR-88D 0.5° base reflectivity image from Greer, South Carolina (KGSP), taken at 0015 UTC 24 July 1997. (b) GOES-8 visible satellite image taken at 2315 UTC 23 July 1997.

Fig. 4.24. (a) WSR-88D 0.5° base reflectivity image from Wakefield, Virginia (KAKQ), taken at 1318 UTC 24 July 1997. (b) GOES-8 visible satellite image taken at 1315 UTC 24 July 1997.

Fig. 4.25. (a) WSR-88D 0.5° base reflectivity image from Wakefield, Virginia (KAKQ), taken at 1814 UTC 24 July 1997. (b) GOES-8 visible satellite image taken at 1815 UTC 24 July 1997.

Fig. 4.26. Vertical profiles of diabatic heating averaged in a $3^\circ \times 3^\circ$ box around TC Danny valid between 0000 UTC 23 July and 1200 UTC 24 July. Each colored line represents the valid forecast time (DD/HH format).

Fig. 4.27. Map of 250-hPa wind speed (shading, kt), 250-hPa PV (solid gray every 1 PVU), 250-hPa relative humidity (gray shading, %), 600–400-hPa layer-averaged vertical motion (solid red every 4×10^{-3} hPa s^{-1} , negative values only), and 300–200-hPa layer-averaged irrotational wind (vectors starting at 5 m s^{-1}) at 1800 UTC 23 July 1997. The green TC symbol denotes the position of TC Danny as depicted by the CFSR.

Fig. 4.28. Same as Fig. 4.27, except at 0600 UTC 24 July 1997.

Fig. 4.29. Same as Fig. 4.27, except at 1800 UTC 24 July 1997.

Fig. 4.30. Surface analysis at 1200 UTC 23 July 1997 displaying MSLP (solid black every 2 hPa), winds (barbs, kt), dewpoint (dashed green every 2°C), and temperature (dashed red every 2°C). The green TC symbol denotes the position of TC Danny as depicted by the CFSR.

Fig. 4.31. Same as Fig. 3.30, except at 0000 UTC 24 July 1997.

Fig. 4.32. Same as Fig. 3.30, except at 1200 UTC 24 July 1997.

Fig. 4.33. North–south vertical cross section of Petterssen frontogenesis [shaded, $\text{K} (100 \text{ km})^{-1} (3 \text{ h})^{-1}$], potential temperature (solid black every 4 K), vertical motion (dashed red every 4×10^{-3} hPa s^{-1} , negative values only), horizontal wind speed (solid orange every 5 m s^{-1} starting at 15 m s^{-1}), and the ageostrophic wind component tangential to the cross section (arrows, m s^{-1}) at 1800 UTC 23 July 1997. The yellow star denotes the position of TC Danny as depicted by the CFSR. The location of the vertical cross section is shown in Fig. 4.11.

Fig. 4.34. Same as Fig. 4.33, except a north-northwest–south-southeast vertical cross section at 0600 UTC 24 July 1997. The location of the vertical cross section is shown in

Fig. 4.35. Same as Fig. 4.33, except a north-northwest–south-southeast vertical cross section at 1800 UTC 24 July 1997. The location of the vertical cross section is shown in

Fig. 5.1. Conceptual models depicting important mechanisms and processes leading to (a) “Camille-like” and (b) “Danny-like” events. For both conceptual models, 500-hPa geopotential height is indicated by solid black contours, the positive PV anomaly is shaded in orange, the upper-tropospheric jet is shaded in light blue, regions of warm-air advection and cold-air advection are indicated by red and blue shaded regions, respectively, and areas of PW exceeding 50 mm are shaded in light green. The red TC symbol indicates the position of the TC. (a) Low-level jet is indicated by the orange arrow. The placement of orography is indicated by the triangular symbols. The approximate area of heaviest rainfall is indicated by dark green shading. (b) Diabatically driven outflow is indicated by the black arrows emanating from the TC.

I. Introduction

1.1 General Purpose

The purpose of this thesis is to present two multiscale analyses of inland tropical cyclone (TC)–midlatitude jet interactions. More specifically, the main focus will be to document the synoptic-scale environment and underlying mesoscale processes responsible for inland flooding associated with TC Camille (1969) and the inland reintensification of TC Danny (1997). The interaction of each storm with an equatorward entrance region of an upper-tropospheric jet links the two cases; however, TC Camille did not undergo inland reintensification. TC Camille will serve as a null case of an inland reintensifying TC in an equatorward entrance region of an upper-tropospheric jet to identify synoptic-scale influences that limit a TC from undergoing inland reintensification. For historical context, the TC Danny inland reintensification case will be compared with other cases of inland reintensifying TCs east of the Rocky Mountains from 1950 through 2010. Similarities and differences between TC Camille and TC Danny will be discussed toward the end of this thesis, which will be beneficial in understanding the specific conditions needed to bring about various inland TC impacts. These similarities and differences will provide forecasters information they can utilize to predict the threats associated with inland TC–midlatitude jet interactions. To provide further background on this research topic, the rest of this chapter will discuss previous research documenting the various interactions that take place between TCs and the midlatitude flow. Topics from the previous research will include interactions during extratropical transition (ET), TC intensification, and interactions associated with inland flooding.

1.2 Motivation and Overview

A growing awareness of societal impacts associated with landfalling and transitioning TCs in recent decades has led to increasing attention to the interactions between TCs and the midlatitude flow. Although our understanding of these interactions has improved, research is needed to provide additional insight into localized effects of inland-moving TCs. Accurate numerical forecasts continue to be a problem because of the relatively small scale of TCs and the complex physical processes that occur during the interactions between a TC and the midlatitude environment (Jones et al. 2003). Forecast challenges include cases which undergo strong ET in the midlatitudes, result in reintensification prior to landfall or over the ocean where shipping lanes are impacted, and produce severe inland flooding. According to Rappaport (2000), in a 30-yr (1970–1999) study of fatality statistics associated with TCs and their remnants, more than half of the 600 U.S. deaths were caused by freshwater flooding. Most of these freshwater fatalities were located inland.

One of the most severe cases of inland flooding can be attributed to TC Camille, which has not been given as much retrospective scrutiny as TC Connie (1955; Dunn et al. 1955; Namias and Dunn 1955), TC Diane (1955; Dunn et al. 1955; Namias and Dunn 1955), TC Agnes (1972; Carr and Bosart 1978; Bosart and Dean 1991), TC Fran (1996; Pasch and Avila 1999), and TC Floyd (1999; Atallah and Bosart 2003; Colle 2003). TC Camille is unique since the severe localized flooding observed in the mountains of west-central Virginia occurred while TC Camille was weakly transitioning into an extratropical cyclone as identified by Chien and Smith (1977). Therefore, an examination

of this event would be beneficial to understanding the specific setup needed to produce severe inland flooding.

When a TC moves over land, the surface sensible and latent heat fluxes are greatly reduced, which weakens the TC. In special circumstances, a TC can reintensify while over land: TC David (1979; Bosart and Lackmann 1995), TC Danny (1997; Bassill and Morgan 2006), and TC Erin (2007; Arndt et al. 2009; Monteverdi and Edwards 2010; Evans et al. 2011). The lack of documentation of inland reintensifying TCs provides an opportunity to better understand the mechanisms and processes that lead to such an event, which gives motivation for analyzing the TC Danny case more in depth. Whereas Bassill and Morgan (2006) provided a first-look analysis of the inland reintensification of TC Danny, a more complete and detailed analysis will be conducted in this thesis.

1.3 Interactions between TCs and Midlatitude Troughs and Jets

1.3.1 ET of TCs

As a TC moves from the tropics into the midlatitudes, it may interact with the midlatitude flow and undergo ET. The ET process was split into two stages by Klein et al. (2000): 1) the transformation and 2) the reintensification stages. The transformation stage of ET has been well documented (e.g., DiMego and Bosart 1982a,b; Sinclair 1993; Harr and Elsberry 2000; Klein et al. 2000; Atallah and Bosart 2003; Jones et al. 2003) and is described by Klein et al. (2000) as the process where the TC circulation becomes tilted and transforms from a barotropic to a baroclinic system (Fig. 1.1). In this process, a lower-tropospheric temperature advection dipole develops, where cold, dry air wraps into the TC circulation from the west, and warm, moist air moves poleward east of the

circulation and ascends over tilted isentropic surfaces associated with a preexisting baroclinic zone. In the latter region, typically northeast of the TC circulation, there is enhanced precipitation. Although the process of ET is well understood, defining the exact onset of ET is still problematic. Recent studies have suggested that the onset of ET may occur when the rate of increase in frontogenesis peaks (Harr et al. 2000) or can be detected by using a phase diagram of thermal wind and thermal asymmetry (Hart 2003).

After the transformation stage is complete, intensification of the prior TC as an extratropical cyclone may take place. Most studies have acknowledged that the structure of the midlatitude circulation affects whether an extratropical cyclone will intensify or weaken (e.g., Harr et al. 2000; Klein et al. 2002; Sinclair 2002; Ritchie and Elsberry 2003; Sinclair 2004; Hart et al. 2006; Ritchie and Elsberry 2007). In the North Pacific, Harr et al. (2000) found that a northwest (northeast) pattern is typically associated with ET in that region. A northwest pattern is characterized by a midlatitude trough that is located northwest of a poleward-moving TC, whereas a northeast pattern is characterized by a large quasi-stationary midlatitude cyclone that is located northeast of a poleward-moving TC. Harr et al. (2000) found that a northwest (northeast) pattern is typically associated with a strengthening (weakening) extratropical cyclone after ET (Fig. 1.2). Harr et al. (2000) diagnosed the differences between the two patterns by evaluating low-level eddy heat fluxes and an energy budget. Simulations conducted by Ritchie and Elsberry (2003) found that the strength of a midlatitude trough had no impact on the final intensification of a transitioned TC after ET. Expanding upon the research conducted by Ritchie and Elsberry (2003), Ritchie and Elsberry (2007) investigated whether the phasing between a remnant TC and an upper-tropospheric trough had an impact on the

final intensification of the transitioned TC after ET. Ritchie and Elsberry (2007) showed that the phasing of the remnant TC with an upstream midlatitude trough was important for enabling extratropical cyclogenesis.

In addition to a midlatitude trough, the interaction of a transitioning TC with a midlatitude upper-tropospheric jet has been documented. The diabatically driven outflow associated with a TC has been shown to impact the magnitude of an upper-tropospheric midlatitude jet and downstream geopotential height field (e.g., Archambault 2011; Fig. 1.3). In a climatology of recurving Northwest Pacific TCs, Archambault (2011, chapter 2) explains that the upper-tropospheric irrotational wind, indicative of the diabatically driven outflow, is directed radially outward from the ascent region associated with a recurving TC and into the meridional potential vorticity (PV) gradient. Lower values of PV are advected by the upper-tropospheric irrotational wind towards higher values of PV, which tightens the meridional PV gradient. As a result, jet streak intensification and upper-tropospheric ridge amplification may occur. The locations of these recurving TCs were generally found to be in the equatorward entrance region of an upper-tropospheric jet, which corresponds to a region of upper-level divergence and, therefore, with tropospheric-deep ascent (Uccellini and Kocin 1987; Fig. 1.4). The jet-entrance region is typically associated with a thermally direct secondary circulation, where divergent (convergent) ageostrophic winds are found on the equatorward (poleward) side of the jet-entrance region.

1.3.2 Intensification Changes of TCs

A TC may intensify when the system is in a favorable environment (e.g., low vertical wind shear, warm sea surface temperatures, moist conditions in the lower-to-middle troposphere). However, studies have shown that TCs can intensify when interacting with midlatitude troughs and jets, which are associated with higher wind shear than observed during TC development (e.g., Molinari and Vollaro 1989; Molinari and Vollaro 1990; Shi et al. 1990; Molinari et al. 1995; Shi et al. 1997; Molinari et al. 1998; Bosart et al. 2000; Hanley et al. 2001; Hanley 2002; Kimball and Evans 2002; Yu and Kwon 2005; Rappin et al. 2011). Among these cited studies, the interactions between TCs and troughs have been analyzed using diagnostics [eddy flux convergence (EFC; e.g., Molinari and Vollaro 1989; Yu and Kwon 2005); Ertel PV (e.g., Molinari et al. 1995; Hanley et al. 2001)], observations [satellite imagery (e.g., Bosart et al. 2000; Hanley 2002)], and three-dimensional models (e.g., Kimball and Evans 2002; Rappin et al. 2011).

Molinari and Vollaro (1989) used calculations of EFC to diagnose the rapid intensification of Hurricane Elena (1985) over the Gulf of Mexico. When analyzing the calculated values of EFC, Molinari and Vollaro (1989) found a high correlation between the angular momentum fluxes by azimuthal eddies at large radii and central pressure changes in the storm 27–33 h later (Fig 1.5). Molinari and Vollaro (1989) also noted an inward shift of cyclonic eddy momentum that was produced by the passage of a midlatitude trough poleward of Hurricane Elena. Sources of anticyclonic eddy momentum removal from the TC circulation included the west-southwesterly flow ahead of the trough and the outflow jet equatorward of the TC. A subsequent study by Molinari

and Vollaro (1990) would argue the trough was not a direct cause of the deepening, but a catalyst that produced locally enhanced surface fluxes and associated convection that supported the formation of a contracting secondary eyewall.

Upper-tropospheric jets have also been documented to impact TC intensification. Simulations of a TC–jet interaction conducted by Rappin et al. (2011) show that the convective outflow associated with a TC modifies an upper-tropospheric jet, resulting in a weaker shear environment and rapid intensification of the TC–jet couplet. Shi et al. (1997) observed a high correlation between an approaching upper-tropospheric jet with a sudden burst of inner-core convection associated with Hurricane Florence (1988). The increased convection was said to be crucial to the intensification of Hurricane Florence, which is similar to the argument made by Bosart et al. (2000) documenting the rapid intensification of Hurricane Opal (1995).

In the 12-yr period from 1985 through 1996, Hanley et al. (2001) used values of EFC greater than $10 \text{ (m s}^{-1}\text{) day}^{-1}$ to identify TC–trough interactions. A total of 146 interactions were identified and sorted into four distinct composites of TC–trough interactions: favorable distant interaction, favorable superposition, unfavorable distant interaction, and unfavorable superposition. Distant interactions were identified when an upper-tropospheric PV maximum was between 1000 km and 400 km from the TC center, while a superposition was deemed to take place when a PV maximum was within 400 km of the TC center. A composite of the favorable distant interactions shows a PV trough well to the west of and comparable in size to the TC (Fig. 1.6). The TC is located underneath the entrance region of an upper-tropospheric jet, where upper-level divergence is occurring. The comparable size of the PV trough to the size of the TC was

believed to be important in enabling a favorable interaction between the two features. The effect of reduced vertical wind shear over the TC circulation was thought to be the main reason for the favorable interaction. Similar arguments concerning the comparable trough to TC size have been made in previous studies (Molinari et al. 1995; Bosart et al. 2000).

1.3.3 Inland Flooding Associated with TCs

As previously mentioned, flooding associated with TCs is the largest contributor to TC-related fatalities, which are mainly located inland (Rappaport 2000). A 49-yr (1950–1998) climatology of precipitation distributions associated with landfalling TCs was conducted by Atallah et al. (2007). Their climatology was split into left-of-center (LOC) and right-of-center (ROC) composites showing the environmental setup favoring each distribution pattern (Fig. 1.7). LOC precipitation distributions are identified to have an upper-tropospheric trough upstream of the TC circulation, with positive (negative) PV advection tendencies southwest (northeast) of the TC. ROC precipitation distributions are associated with a TC embedded upstream of an upper-tropospheric ridge axis and downstream of a weak and shallow upper-tropospheric trough. Only a negative PV advection tendency is seen to the northeast of the TC, resulting from latent heat release associated with precipitation.

Heavy precipitation associated with TCs has been documented to occur in the presence of surface frontogenesis (e.g., Bosart and Dean 1991), upper-level divergence associated with an upper-tropospheric jet (e.g., DeLuca 2004), and cold-air damming (e.g., Srock and Bosart 2009). Mesoscale distributions of heavy rainfall associated with TCs over the Northeast U.S. were documented by Klein (2007). In similar fashion to

Atallah et al. (2007), Klein (2007) broke down precipitation distributions into left-of-track (LOT) and right-of-track (ROT) distributions. The LOT distributions were associated with an upper-tropospheric jet poleward of the TC center, whereas ROT distributions had an upper-tropospheric jet farther downstream and to the northeast of the TC. Klein (2007) noted that the heaviest rainfall occurs along and on the cold side of mesoscale surface boundaries in both LOT and ROT distributions. Vertical cross sections of frontogenesis and upward vertical motion for LOT and ROT distributions are shown in Fig. 1.8. For LOT distributions, tropospheric-deep frontogenesis and the ascent pattern tilts towards the cold air with increasing height with ascent maximized in the midtroposphere on the warm side of the frontogenesis maximum. For ROT distributions, surface frontogenesis is dominant and the ascent pattern is upright and located on the warm side of the frontogenesis maximum with ascent maximized above the boundary layer. For both LOT and ROT distributions, the presence of a cyclonically curved lower-tropospheric jet to the east side of the TC enhances the poleward flux of tropical air from the Atlantic into the surface frontal boundary.

In the past five years, research has gone into understanding a newly identified contributor to inland flooding associated with TCs. The term “predecessor rain event (PRE)” was first coined by Cote (2007), where he documented the spatial structure and temporal evolution of a mesoscale region of heavy rainfall separate from the main TC rain shield that develops poleward of landfalling or coastal-tracking Atlantic basin TCs. Based on his 9-yr climatology, from 1998 through 2006, Cote (2007) noted that PREs are associated with the transport of anomalously high moisture directed towards a lower-tropospheric baroclinic zone underneath an equatorward entrance region an upper-

tropospheric jet. Most PREs were located approximately 1000 km poleward of the TC and occurred 36 h before the arrival of the TC. After Cote (2007), several studies have verified the findings of his research and have provided more case-specific analyses of PREs (e.g., Galarneau et al. 2010; Moore 2010; Schumacher et al. 2011; Bosart et al. 2012). In an extended climatology (1988–2008), Moore (2010) stratified PREs into three categories based upon the upper-tropospheric setup within which the PRE and TC were embedded: jet in ridge (JR), southwesterly jet (SJ), and downstream confluence (DC) (Fig. 1.9). An overriding characteristic of each conceptual model is the presence of a moist, lower-tropospheric jet east of the TC that is directed towards a lower-tropospheric baroclinic zone underneath an equatorward entrance region of an upper-tropospheric jet.

1.4 Documented Cases of Inland Reintensifying TCs

As previously stated, there have been only three documented cases of an inland reintensifying TC: TC David (1979; Bosart and Lackmann 1995), TC Danny (1997; Bassill and Morgan 2006), and TC Erin (2007; Arndt et al. 2009; Monteverdi and Edwards 2010; Evans et al. 2011). Although each case reintensified while over land, the mechanisms and processes that led to the strengthening of each TC differ.

The reintensification of TC David occurred over the Northeast U.S. about 36 h after making a final landfall over southeast Georgia. As TC David traversed poleward across Pennsylvania, it reintensified in response to tropopause lifting ahead of a weak upper-tropospheric trough due to diabatic heating from deep convection associated with the TC (Bosart and Lackmann 1995). Reduction of the upper-tropospheric trough wavelength occurred in conjunction with diabatically driven down-shear ridge building,

which led to increased cyclonic vorticity advection over TC David as this trough approached from the southwest. The associated ascent and low-level horizontal convergence created a favorable environment for generating cyclonic vorticity within the moist neutral thermodynamic environment around TC David. The development of an upper-tropospheric jet poleward of TC David also aided in the ascent around the TC circulation.

The inland reintensification of TC Danny over the Carolinas occurred approximately four days after making a final landfall in southern Alabama. Cyclonic vorticity advection from an approaching upstream trough, upper-level divergence situated in the equatorward entrance region of an upper-tropospheric jet, and vortex tube stretching as the storm traversed the southern Appalachian Mountains were the main reasons for the inland reintensification of TC Danny (Bassill and Morgan 2006). All of these factors, in addition to the moist neutral thermodynamic environment surrounding TC Danny, were important in the generation of near-surface cyclonic vorticity. Bassill and Morgan (2006) found that low values of PV generated above and poleward of TC Danny was associated with latent heat release in the presence of deep convection. The generation of low values of PV ahead of the upstream trough, characterized by higher values of PV, tightened the meridional PV gradient and led to an intensification of the upper-tropospheric jet poleward of TC Danny. The low values of PV also served to decrease the vertical wind shear above the TC, which was conducive for intensification.

The reintensification of TC Erin over Oklahoma is unique because of its location over the southern Plains and the dense observational network provided by the Oklahoma Mesonet during the event (Arndt et al. 2009). In addition, TC Erin did not have the

upper-level support seen in the TC David and TC Danny cases. However, the moist neutral thermodynamic environment surrounding TC Erin favored low-level convergence, deep rising motion, and near-surface cyclonic vertical vorticity generation (Evans et al. 2011). A southerly lower-tropospheric jet extending from the Gulf of Mexico provided moisture and generated instability in the region ahead of TC Erin. Evans et al. (2011) further showed that anomalously wet months (March through July 2007) preceding TC Erin had the greatest positive impact on its reintensification among three analyzed soil moisture-related signals: a seasonal signal, an along-track rainfall signal, and an early postlandfall rainfall signal. The high soil moisture content resulting from the anomalously wet months provided moisture and greater instability in the boundary layer. Inland TC reintensification has been found to occur in situations where the underlying surface has high heat conductivity and is relatively moist (Shen et al. 2002), and when rainfall ahead of a TC falls on desert soils and provides sufficient surface heat fluxes for a TC to reintensify (Emanuel et al. 2008).

1.5 Goals and Organization of Thesis

The main goals of this thesis are to: (1) document the synoptic-scale environment and underlying mesoscale processes responsible for inland flooding associated with TC Camille (1969) and the inland reintensification of TC Danny (1997); (2) explain similarities and differences between the TC Camille and TC Danny cases; and (3) document important mechanisms and processes that lead to various impacts associated with inland TC–midlatitude jet interactions.

The remainder of this thesis will be organized as follows. Chapter 2 will discuss the data and methods used to construct the list of inland reintensifying TCs and to conduct the two multiscale analyses. The multiscale analyses of TC Camille and TC Danny will be documented in Chapter 3 and Chapter 4, respectively. Chapter 5 will compare and contrast the two TC cases, and provide concluding remarks and suggestions for future work.

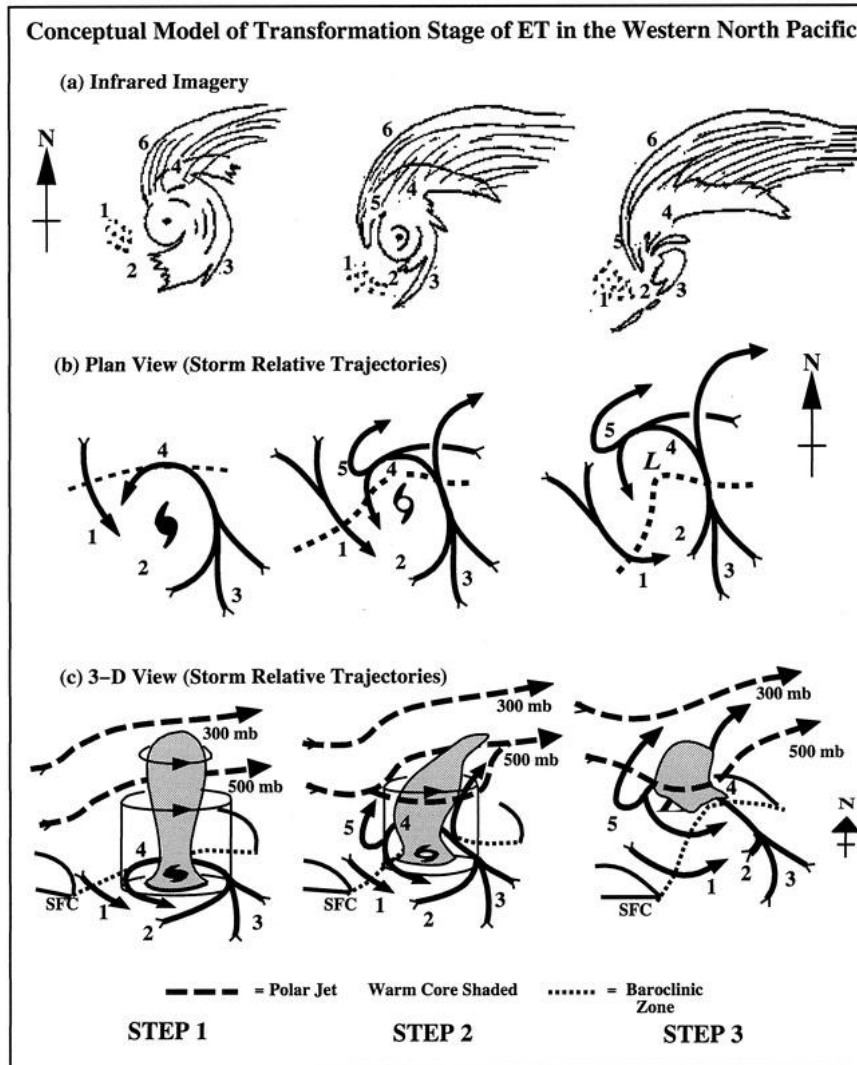


Fig. 1.1. Conceptual model of transformation stage of ET in the western North Pacific, with labeled areas as follows: 1) environmental equatorward flow of cooler, drier air (with corresponding open cell cumulus); 2) decreased TC convection in the western quadrant (with corresponding dry slot) in step 1, which extends throughout the southern quadrant in steps 2 and 3; 3) environmental poleward flow of warm, moist air is ingested into TC circulation, which maintains convection in the eastern quadrant and results in an asymmetric distribution of clouds and precipitation in steps 1 and 2; steps 2 and 3 also feature a southerly jet that ascends tilted isentropic surfaces; 4) ascent of warm, moist inflow over tilted isentropic surfaces associated with baroclinic zone (dashed line) in middle and lower panels; 5) ascent (undercut by dry-adiabatic descent) that produces cloudbands wrapping westward and equatorward around the storm center; dry-adiabatic descent occurs close enough to the circulation center to produce erosion of eyewall convection in step 3; 6) cirrus shield with a sharp cloud edge if confluent with polar jet. Caption and figure reproduced from Fig. 5 in Klein et al. (2000).

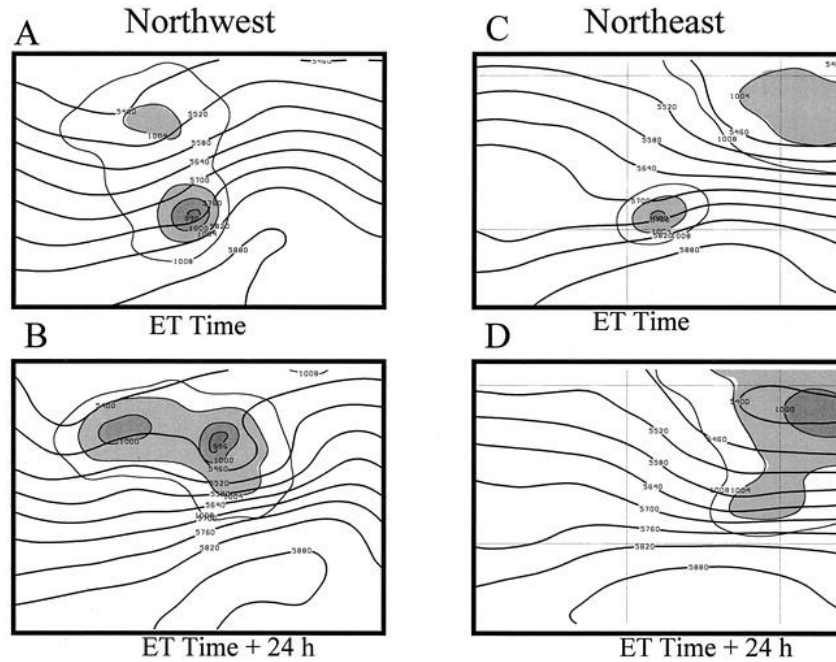


Fig. 1.2. Composite 500-hPa height (m) and sea level pressure (hPa, only below 1008 hPa) analyses based on grouping of cases in a northwest pattern at the (a) ET time, (b) ET + 24 h, and in a northeast pattern at the (c) ET time and (d) ET + 24 h. The composite northwest pattern is based on 13 cases and the northeast pattern is based in 17 cases. Caption and figure reproduced from Fig. 1 in Harr et al. (2000).

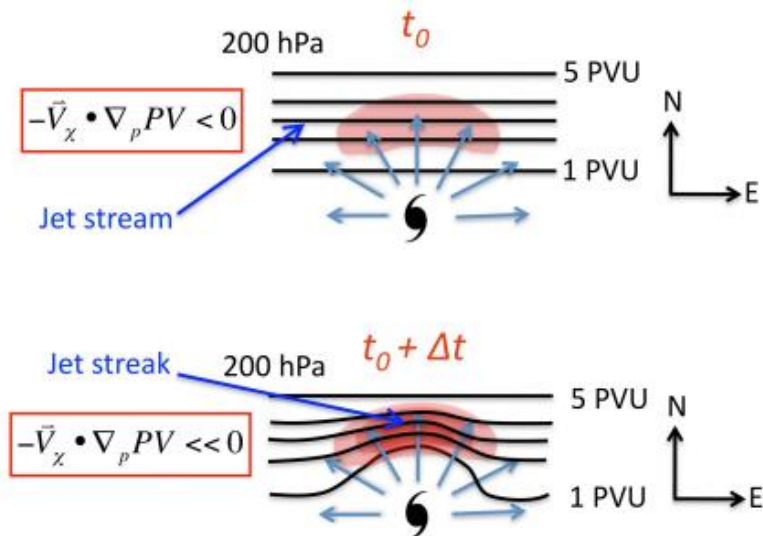


Fig. 1.3. Schematic representation of upper-tropospheric ridge amplification and jet streak intensification associated with divergent TC outflow impinging upon an upper-tropospheric jet stream (i.e., a meridional PV gradient). Caption and figure reproduced from Fig. 2.6 in Archambault (2011).

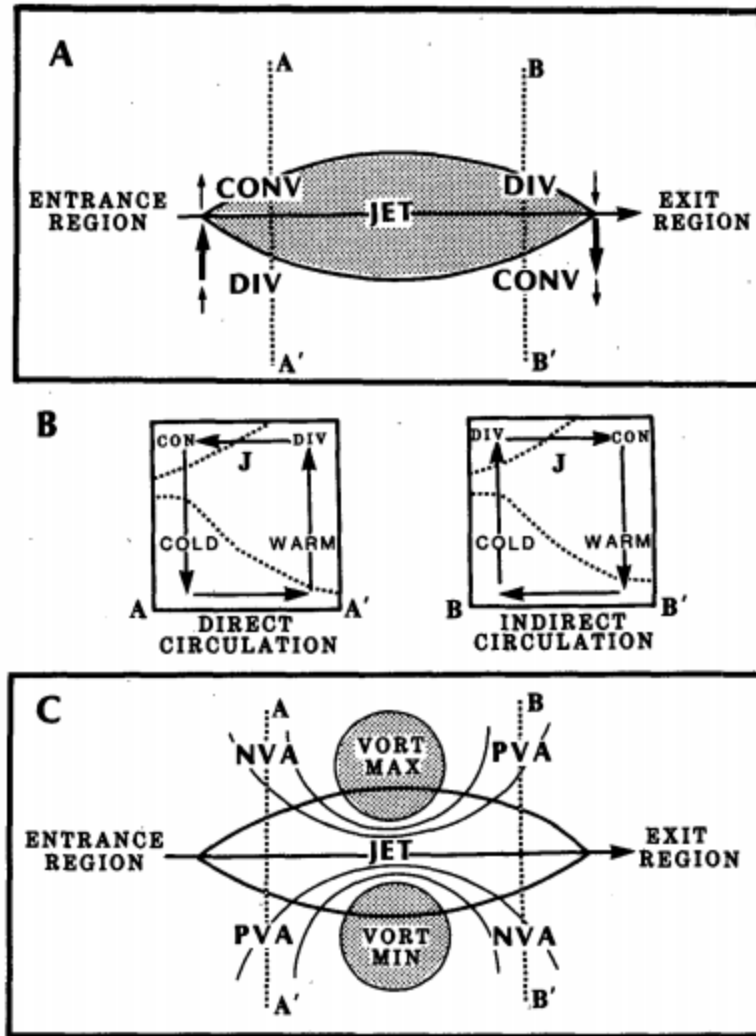


Fig. 1.4. (a) Schematic of transverse ageostrophic wind components and patterns of divergence associated with the entrance and exit regions of a straight jet streak [after Bjerknes (1951)]. (b) Vertical cross sections illustrating direct and indirect circulations in the entrance region [along dotted line labeled A–A' in (a)] and exit region [along dotted line labeled B–B' in (a)] of a jet streak. Cross sections include two representative isentropes (dotted), upper-tropospheric jet location (marked by a J), relative positions of cold and warm air, upper-level divergence, horizontal ageostrophic components, and vertical motion (arrows) within the plane of each cross section. (c) Schematic of maximum (cyclonic) and minimum (anticyclone) relative vorticity centers and associated advection patterns associated with a straight jet streak. (NVA represents negative or anticyclonic vorticity advection; PVA represents positive or cyclonic vorticity advection.) Caption and figure reproduced from Fig. 3 in Uccellini and Kocin (1987).

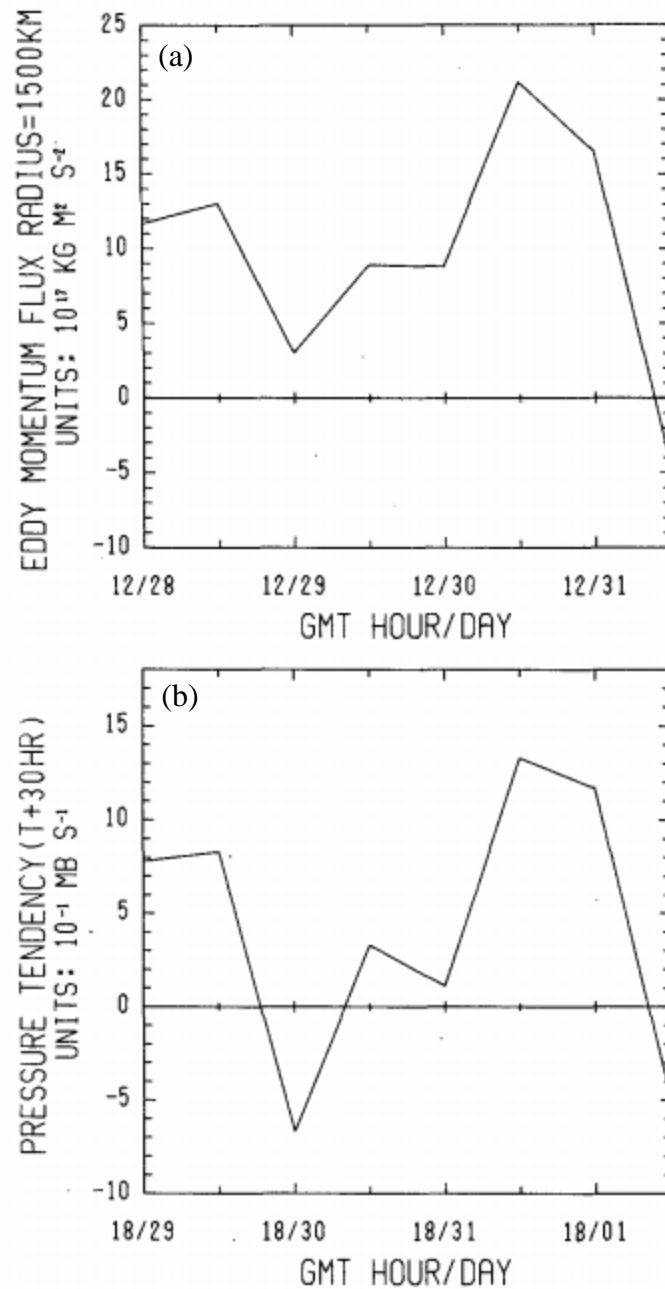


Fig. 1.5. (a) Eddy momentum flux at the 1500 km radius, plotted only for those times in which the storm remained over water 30 h later. (b) Deepening rate of the storm at times 30 h after those of part (a). Caption and figure reproduced from Fig. 4 in Molinari and Vollaro (1989).

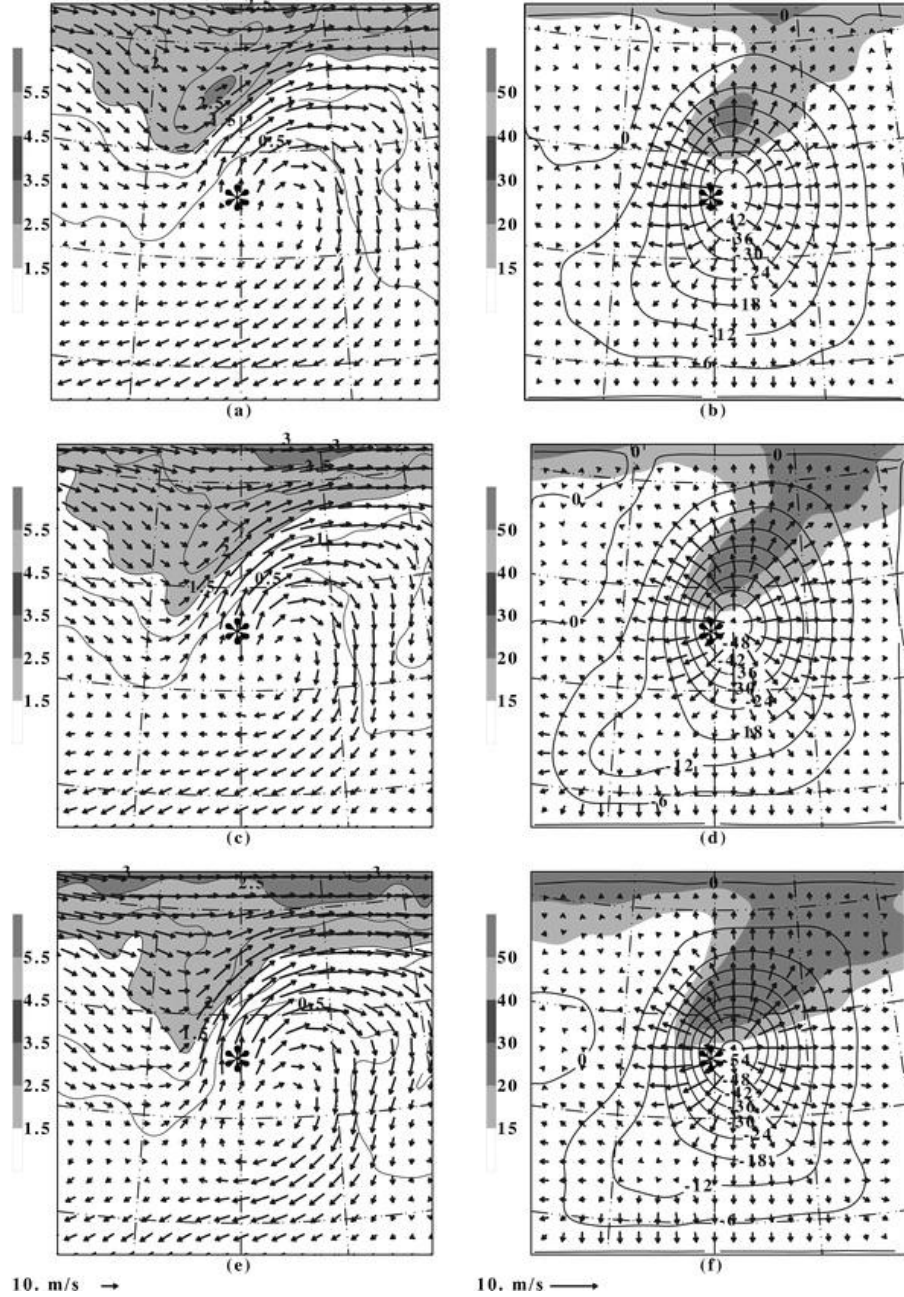


Fig. 1.6. Horizontal plot on the 200-hPa surface for the favorable distant interaction composite containing cases with a total δp of more than 10 hPa. (a), (c), and (e) Vectors of the total wind [m s^{-1} , reference arrow indicated at bottom left of (e)] and Ertel PV (increment is 0.5 PVU and values greater than 1.5 PVU are shaded as indicated) at times $t_0 - 12$ h, t_0 , and $t_0 + 12$ h, respectively. (b), (d), and (f) Total wind speed (m s^{-1} , values greater than 15 m s^{-1} are shaded as indicated), velocity potential ϕ (solid lines, contour interval $6 \times 10^5 \text{ m}^2 \text{ s}^{-1}$), and divergent wind \mathbf{V}_d [m s^{-1} , reference arrow indicated at bottom left of (f)] at times $t_0 - 12$ h, t_0 , and $t_0 + 12$ h, respectively. Asterisk denotes the location of the composite TC center, and the increment in latitude and longitude is 10° . Caption and figure reproduced from Fig. 5 in Hanley et al. (2001).

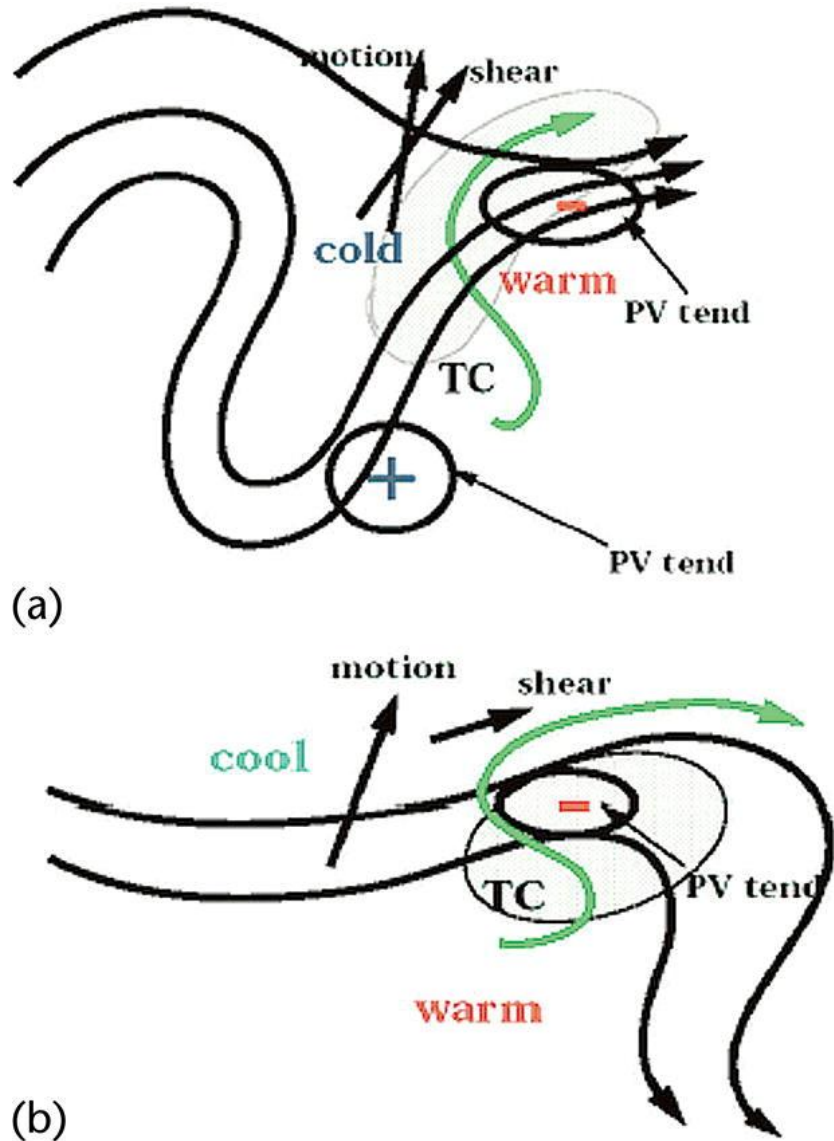


Fig. 1.7. Schematics for landfalling TCs for (a) the LOC composite and (b) the ROC composite. The curved black lines represent streamlines of the upper-tropospheric (i.e., 250 hPa) flow. Arrows represent motion and deep tropospheric shear with the relative magnitudes given by the length of the arrow. The curved green line represents the trajectory of a parcel starting near the surface in the warm sector and ending in the mid- to upper troposphere in the cool sector. The gray shaded area represents regions of precipitation and pluses and minuses represent the local PV tendency resulting from a combination of advection and the diabatic redistribution of PV. Caption and figure reproduced from Fig. 10 in Atallah et al. (2007).

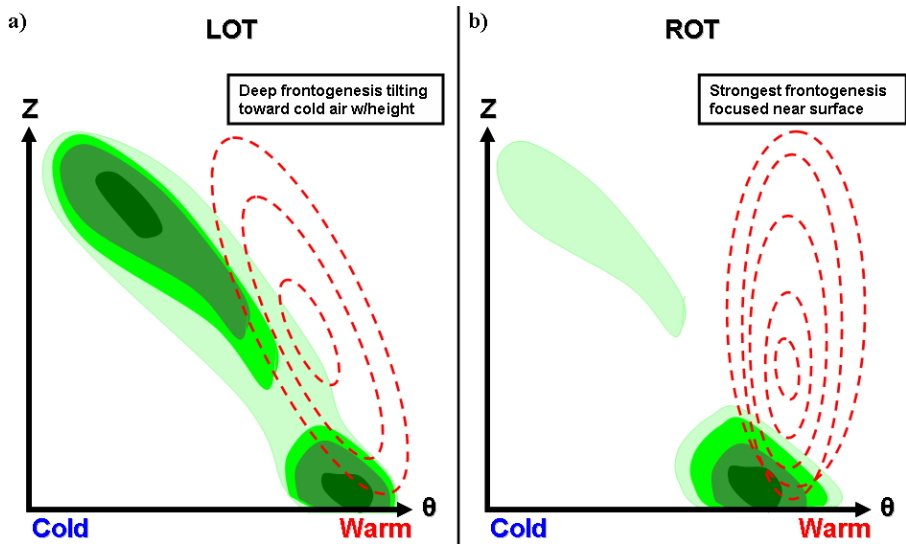


Fig. 1.8. Schematic cross section of the warm-frontal boundary found in (a) LOT precipitation distribution cases and (b) ROT precipitation distribution cases. Cross section includes frontogenesis shaded in green and vertical velocity dashed contoured in red. Caption and figure reproduced from Fig. 4.3 in Klein (2007).

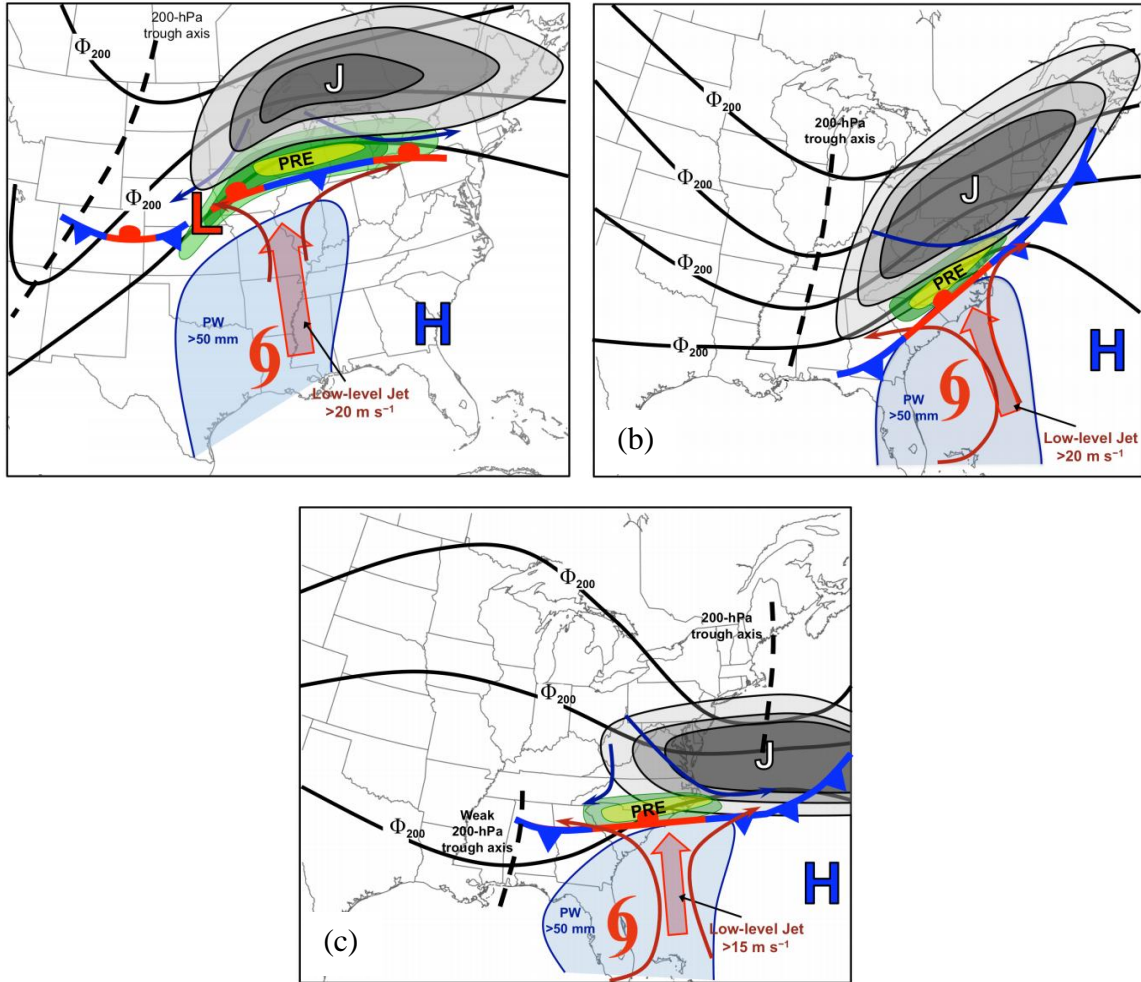


Fig. 1.9. Conceptual model of the synoptic-scale environment of (a) JR, (b) SJ, and (c) DC category PREs showing 200-hPa geopotential height (solid black contours), 200-hPa wind speed (gray shading; “J” symbol marks the location of maximum wind speed), low-level (i.e., 925-hPa) streamlines (red indicates warm advection, blue indicates cold advection), the lower-tropospheric jet (large red arrow), the lower-tropospheric baroclinic zone (stationary front symbol), and precipitable water (PW; values > 50 mm shaded in blue). The position of the PRE is indicated by the green shading, the position of the TC is indicated by the tropical storm symbol, and the maxima and minima in low-level geopotential height are indicated by the “H” and “L” symbols, respectively. Caption and figures reproduced from Figs. 6.1, 6.2, and 6.3 in Moore (2010).

2. Data and Methodology

2.1. List of Inland Reintensifying TCs

Potential cases of inland reintensifying TCs from 1950 through 2010, identified herein as “candidate cases,” are identified using the National Hurricane Center (NHC) best track dataset at 6-h time intervals (0000, 0600, 1200, and 1800 UTC; available at <http://www.nhc.noaa.gov/pastall.shtml>). Candidate cases included TCs whose tracks may have ended, as analyzed by the NHC best track, over land or where the NHC best track indicates a TC strengthened inland.

Archived surface analyses, produced by the then National Meteorological Center (NMC) that became the National Centers for Environmental Prediction (NCEP), and displayed on 35-mm microfilm at the University at Albany Science Library are used to review surface analyses produced during the inland passage of TCs identified as candidate cases that occurred from 1962 through 1995. Candidate cases that occurred prior to 1962 and after 1995 are assessed using *Daily Weather Maps* stored in an online archive by the National Oceanic and Atmospheric Administration (NOAA) Central Library Data Imaging Project (available at http://docs.lib.noaa.gov/rescue/dwm/data_rescue_daily_weather_maps.html). National Weather Service (NWS) *Digital Facsimile* (DIFAX) surface maps archived by Colorado State University (available at <http://ldm.atmos.colostate.edu/>) are used in conjunction with the NOAA *Daily Weather Maps* to evaluate candidate cases occurring after 2000.

The four times daily (0000, 0600, 1200, and 1800 UTC) $2.5^{\circ} \times 2.5^{\circ}$ National Centers for Environmental Prediction–National Center for Atmospheric Research (NCEP–NCAR) Reanalysis dataset (Kalnay et al. 1996) is used to examine synoptic-scale

flow patterns within which the candidate TC cases were embedded. Higher-resolution, four times daily (0000, 0600, 1200, and 1800 UTC) $1.125^\circ \times 1.125^\circ$ 40-yr ECMWF Re-Analysis (ERA-40) (Uppala et al. 2005) and four times daily (0000, 0600, 1200, and 1800 UTC) $0.5^\circ \times 0.5^\circ$ NCEP Climate Forecast System Reanalysis (CFSR) (Saha et al. 2010) datasets are used to analyze mesoscale details of each candidate TC case. The ERA-40 and NCEP CFSR datasets contain 23 and 37 levels, respectively, on constant pressure surfaces. Candidate cases that occurred prior to 1979 are analyzed using the ERA-40 dataset, while cases since 1979 are analyzed using the NCEP CFSR dataset.

Using information obtained from the previously mentioned observational and reanalysis datasets in this chapter, subjective criteria are implemented for each candidate TC case to create a list of inland reintensifying TCs. To ensure that these candidate TC cases were not undergoing ET or influenced by ocean surface sensible and latent heat fluxes, the following subjective criteria are used to evaluate each candidate TC case:

- A vertically stacked, warm-core structure has to be maintained or enhanced during reintensification.
- The minimum central mean sea level pressure (MSLP) has to decrease by 2 hPa and/or the maximum sustained wind speed has to increase by 5 kt in a 6-h period.
- The central circulation (i.e., eye) of the candidate TC case has to remain over land during reintensification.
- The 500-hPa wind speed has to be less than or equal to 30 kt over the TC center.

Vertical cross sections taken from north to south through the center of each candidate TC, displaying PV and potential temperature, are created to evaluate whether a vertically stacked, warm-core structure was maintained or enhanced as a candidate TC traveled over land. The vertically stacked, warm-core structure of each candidate TC is subjectively determined to be maintained or enhanced during reintensification if the bowing down of isentropes is apparent in the central axis of a vertical or near-vertical PV tower associated with each candidate TC, which is indicative of a warm-core structure. For each candidate TC, NHC best track data and archived surface analyses are used to determine whether the second and third listed criteria are met. The last criterion is determined by analyzing 500-hPa wind maps produced from the ERA-40 and NCEP CFSR datasets for each candidate TC.

2.2. Multiscale Analyses

To conduct the multiscale analysis of TC Camille, reanalysis and observational datasets are used to diagnose the synoptic and mesoscale processes associated with the storm-related inland flooding. The $1.125^\circ \times 1.125^\circ$ ERA-40 dataset is used to generate synoptic-scale charts and to calculate diagnostic quantities that are produced using the General Meteorology Package (GEMPAK; desJardins et al. 1991).

The evolution of precipitation across west-central Virginia that occurred with the passage of TC Camille is tracked using hourly radar summary charts. These radar summary charts, originally hand drawn and produced by the NMC, were obtained from the National Climatic Data Center (NCDC) and then further analyzed by the author. To be more visually appealing, the radar summary charts have been adapted from their

original format and are reproduced following a key created to interpret the radar summary charts (Fig 2.1).

Surface data in Surface Airways Observations (SAO) format obtained from the NCDC Integrated Surface Database (<http://www.ncdc.noaa.gov/oa/climate/isd/index.php>) are plotted in GEMPAK and hand analyzed to track the surface evolution of the inland flooding event associated with TC Camille. The surface analyses include surface temperature and dew point, wind, and MSLP. A caveat for the surface analyses is that a lack of observations across west-central Virginia during the inland flooding event led to an uncertainty in the mesoscale details of the surface analyses.

The multiscale analysis of TC Danny uses a similar combination of reanalysis and observational datasets as for the TC Camille case to diagnose the synoptic and mesoscale processes associated with the inland reintensification event. The gridded $0.5^\circ \times 0.5^\circ$ NCEP CFSR dataset is used to generate synoptic-scale charts and calculate diagnostic quantities similar to the TC Camille case. Unfortunately, using two datasets with different spatial resolutions limits the capability of making exact comparisons between the TC Camille and TC Danny cases. Since the NCEP CFSR dataset only goes back to 1979, this dataset could not be used for the TC Camille case. The TC Danny case could have been conducted using the lower-resolution ERA-40; however, high-resolution details produced by the NCEP CFSR are more realistic than the ERA-40 as illustrated in Fig. 2.2. Figure 2.2a, derived from the ERA-40 dataset, depicts a weak vertical structure of TC Danny for 1800 UTC 24 July 1997, whereas Fig. 2.2b, obtained from the NCEP CFSR reanalysis, shows a more realistic vertical structure for TC Danny as evident in surface wind speeds of approximately 15 m s^{-1} on the southern side of the TC at 1800 UTC 24 July. When

comparing the reanalysis depiction of the surface wind with the observed 20 m s^{-1} maximum sustained wind speed in the NHC best track data at 1800 UTC 24 July, the NCEP CFSR underestimates the surface wind speed. The ERA-40 does not depict a surface wind at or above 15 m s^{-1} around the circulation of TC Danny, which makes the NCEP CFSR more appropriate to use for the TC Danny analysis.

Structural changes in convective and stratiform precipitation around TC Danny are documented prior to and during its inland reintensification using Weather Surveillance Radar–1988 Doppler (WSR-88D) base reflectivity datasets obtained from NCDC (<http://www.ncdc.noaa.gov/nexradinv/>) for multiple WSR-88D locations: Birmingham, Alabama (KBMX); Atlanta, Georgia (KFFC); Greer, South Carolina (KGSP); Columbia, South Carolina (KCAE); and Wakefield, Virginia (KAKQ) . The radar data are then plotted using Gibson Ridge Level 2 Analyst software (GR2Analyst; software can be downloaded at <http://www.grlevelx.com/gr2analyst/>). Visible and infrared satellite imagery obtained from the Unidata–Wisconsin datastream is used in conjunction with the radar data to facilitate the TC Danny analysis.

Standard hourly Automated *Surface Observing System* (ASOS) observations are obtained from an archive at the University at Albany, and are plotted in GEMPAK and hand analyzed to track the surface evolution of TC Danny and its environment as it reintensified inland. Similar to the TC Camille analysis, surface analyses include surface temperature and dew point, wind, and MSLP.

Diabatic heating rates are calculated from $1.0^\circ \times 1.0^\circ$ NCEP CFSR 3-D Diabatic Heating Data 6-h forecasts (Saha et al. 2010) and used to monitor the evolution of the vertical heating distribution prior to and during the inland reintensification of TC Danny.

The diabatic heating rates are calculated in a $3^{\circ}\times 3^{\circ}$ box centered on the central circulation of TC Danny. A visual depiction of this computational box around TC Danny is shown for 0600 UTC 24 July 1997 (Fig. 2.3). The diabatic heating rate calculation includes a shallow convective heating rate, a deep convective heating rate, and a large-scale condensation heating rate (Saha et al. 2010). A caveat to using the NCEP CFSR diabatic heating dataset is that the forecasted placement of convection may be incorrect (M. Janiga 2012, personal communication). A visual check of the forecasted placement of convection shows that it approximately resembles the convection observed around TC Danny during its inland reintensification, which gives confidence in the diabatic heating rate calculations.

The “PV thinking” perspective (e.g., Hoskins et al. 1985; Morgan and Nielsen-Gammon 1998) is used to assist in the diagnosis and interpretation of the TC Danny and TC Camille cases. The utility of using a PV perspective is twofold: (1) identifying sources of diabatic heating that may lead to generation (destruction) of lower- (upper-) tropospheric cyclonic (anticyclonic) PV and reduction of wind shear aloft, and (2) evaluating vertical and horizontal interactions between PV anomalies to diagnose synoptic and mesoscale processes. The analyses for TC Camille and TC Danny calculated Ertel PV, which is conserved following flow that is adiabatic and frictionless, and is evaluated as

—

Changes in PV can be evaluated by using the Lagrangian rate of change of PV, and is approximated as [adapted from Martin 2006, his Eq. (9.23)]:

— —

where \dot{Q} is the diabatic heating rate. A qualitative assessment of Eq. (2) is used in the TC Danny case to infer changes in PV based on changes in \dot{Q} with pressure. Where \dot{Q} increases (decreases) with decreasing pressure, a corresponding increase (decrease) of PV ensues. Calculations of the irrotational wind are produced as a supplementary tool for the PV analysis in the TC Danny case to document the influence of the upper-tropospheric divergent outflow associated with regions of diabatic heating on the upper-tropospheric distribution of PV.

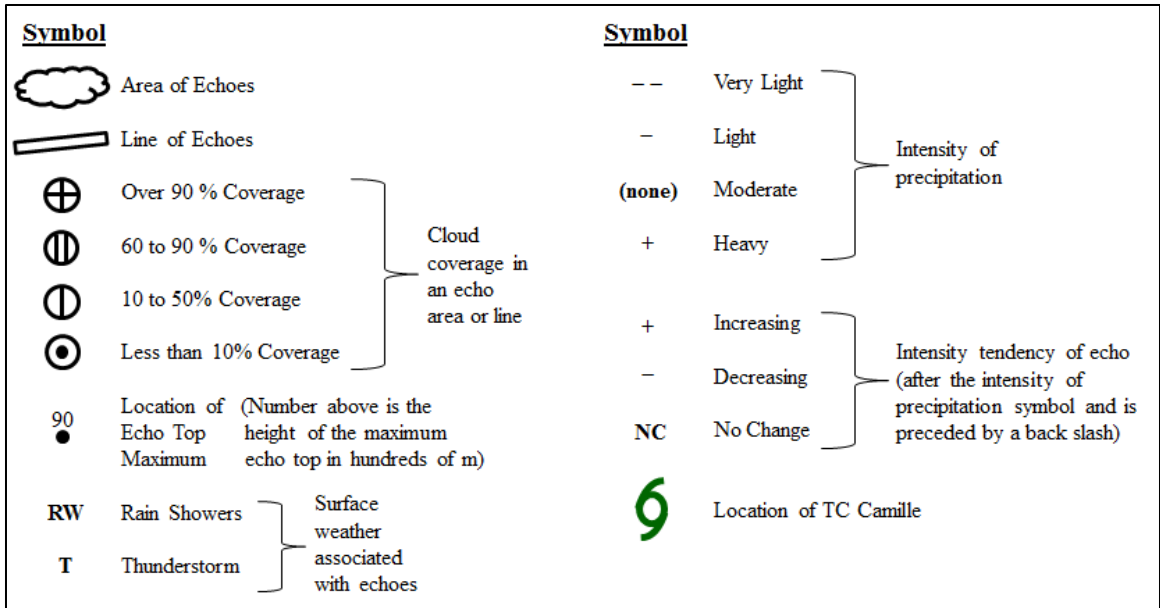


Fig. 2.1. Key displaying the symbols used for the adapted radar summary charts.

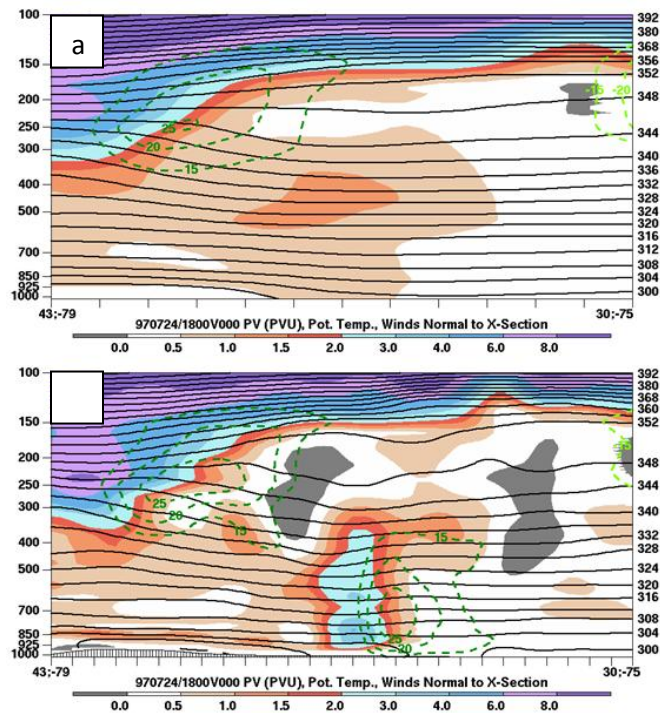


Fig. 2.2. Vertical cross section of PV (shaded every 1 potential vorticity unit [PVU; $10^{-6} \text{ m}^2 \text{ s}^{-1} \text{ K kg}^{-1}$]), potential temperature (solid black every 4 K), and the wind component normal to the cross section (dashed green every 5 m s^{-1} starting at 15 m s^{-1}) at 1800 UTC 24 July 1997 using the (a) ERA-40 and (b) NCEP CFSR.

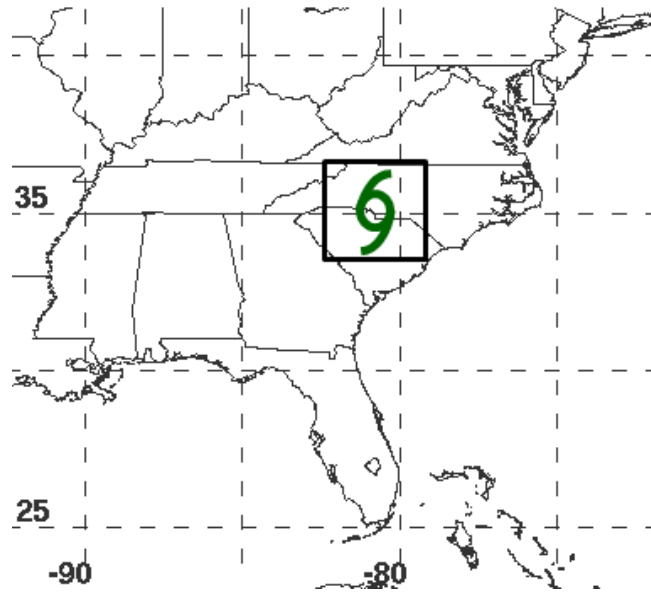


Fig. 2.3. A $3^{\circ}\times 3^{\circ}$ computational box centered on the central circulation of TC Danny (green TC symbol) at 0600 UTC 24 July 1997.

3. TC Camille Multiscale Analysis

3.1. Introduction

3.1.1. TC Track

TC Camille formed and was classified as a tropical storm at 1800 UTC 14 August 1969 in the western Caribbean Sea. TC Camille traveled towards the north-northwest in the coming days and rapidly intensified into a category 5 hurricane as it made its way across the Gulf of Mexico. As indicated by a track map of TC Camille (Fig. 3.1), the category 5 hurricane made landfall in southeastern Louisiana on 0000 UTC 18 August with a minimum central MSLP of 909 hPa and a maximum sustained wind speed of 165 kt. TC Camille weakened rapidly into a tropical depression by 0000 UTC 19 August as it continued to move poleward toward the Ohio River Valley (Fig. 3.1). By 0000 UTC 20 August, TC Camille's minimum central MSLP had risen to 1005 hPa while its maximum sustained wind speed had decreased to 25 kt (Fig. 3.1). TC Camille was downgraded to a tropical depression (TD) at this time as a result of this decrease in wind speed. At 0000 UTC 20 August, the midlatitude flow enabled TC Camille to travel due east across the southern Ohio River Valley. During 20 August, TC Camille traversed the Appalachian Mountains of West Virginia and Virginia, and crossed the Piedmont and Tidewater regions of Virginia thereafter (Fig. 3.1), where TC Camille started undergoing ET at 1200 UTC 20 August. By 1800 UTC 20 August, TC Camille had exited the eastern coast of Virginia and strengthened to 1003 hPa with a maximum sustained wind speed of 40 kt at 0000 UTC 21 August (Fig. 3.1) as the ET process continued. At 0000 UTC 22 August, TC Camille fully transitioned into an extratropical cyclone with a minimum central MSLP of approximately 1000 hPa and a maximum sustained wind speed of 60 kt (Fig.

3.1). Additional details on the track and evolution of TC Camille can be found in Simpson et al. (1970).

3.1.2. Inland Impacts

As TC Camille crossed the Appalachian Mountains early on 20 August, copious amounts of rain fell from southeastern West Virginia through central Virginia and southern Maryland and Delaware, where more than 75 mm of rain fell throughout this region. In a 12-h period from 0000 UTC 20 August–1200 UTC 20 August, the heaviest rainfall occurred over the mountainous region of west-central Virginia, which contains part of the Blue Ridge Mountains, where sloping terrain toward the south and southeast created favorable conditions for upslope precipitation. In the 12-h period starting at 0000 UTC 20 August, approximately 690 mm of rain fell near Massies Mill in Nelson County, which is located in west-central Virginia. The worst flash flooding occurred in areas along the Davis Creek in Nelson County, where multiple families were displaced from their homes. As a result of the flash flooding in this region, 153 fatalities occurred.

3.2. Synoptic Overview

3.2.1. Large-Scale Evolution

The relative position of TC Camille with respect to an equatorward entrance region of an upper-tropospheric jet at 0600 UTC 19 August is depicted in Fig 3.2 using ERA-40 reanalysis data. An analysis of 250-hPa wind speed, 1000–500-hPa thickness, and MSLP shows that the location of TC Camille was approximately 1000 km equatorward of a 45 m s^{-1} upper-tropospheric jet as the TC began to enter the lower Ohio

River Valley (Fig. 3.2). A broad 1018-hPa anticyclone positioned off the southeastern United States coast (Fig. 3.2) worked in tandem with TC Camille to provide a broad low-level southerly flow from the Gulf of Mexico into the southeastern United States (not shown). A near-perpendicular orientation of the 578-dam and 576-dam thickness contours with respect to the sea level isobars over Alabama, Kentucky, and Tennessee implies that warm-air advection was taking place over that area (Fig. 3.2). Poleward of this region, a well-defined lower-tropospheric baroclinic zone, indicated by a thermal gradient of the 1000–500-hPa thickness field, was positioned across the Great Lakes region, which was associated with a 1000-hPa extratropical cyclone centered in south-central Quebec (Fig. 3.2).

As TC Camille traveled across the Ohio River Valley at 1800 UTC 19 August, the TC became juxtaposed with the equatorward entrance region of the 45 m s^{-1} upper-tropospheric jet (Fig. 3.3). The aforementioned 1018-hPa anticyclone off the southeastern United States coast remained in that location (Fig. 3.3) and continued to work in tandem with TC Camille to provide low-level southwesterly flow from the Gulf of Mexico toward West Virginia and Virginia (not shown). A northeastward movement of the 578-dam and 576-dam thickness contours compared to their location in Fig. 3.2 confirms the presence of warm-air advection ahead of TC Camille, which was occurring in West Virginia and Virginia (Fig. 3.3). The surface baroclinic zone poleward of the TC had moved southward into the northeastern United States, and the extratropical cyclone associated with the surface baroclinic zone had deepened to 990 hPa and was centered over southeastern Quebec (Fig. 3.3).

By 0600 UTC 20 August, the aforementioned surface baroclinic zone was quasi-stationary across the mid-Atlantic, and TC Camille continued to be juxtaposed with the equatorward entrance region of the 45 m s^{-1} upper-tropospheric jet (Fig. 3.4). A quasi-perpendicular orientation of thickness contours with respect to sea level isobars beneath the equatorward entrance region of the upper-tropospheric jet (Fig. 3.4) suggests that cold-air advection acted to suppress ascent poleward of TC Camille. The 578-dam and 576-dam thickness contours were positioned in West Virginia and Virginia, indicative of the warm-air advection that took place in the last 12 h (Fig. 3.4). The poleward surface baroclinic zone appeared to be consolidating with the TC Camille circulation in central Virginia (Fig. 3.4), an area that was a focus of heavy rainfall during the flooding event.

TC Camille took on extratropical characteristics by 1800 UTC 20 August, indicated by cold-air advection in the northwest quadrant of the TC circulation as a broad 1022-hPa anticyclone built into the Great Lakes region (Fig. 3.5). The cold-air advection poleward of a surface trough extending southwestward from the central circulation of TC Camille suggests that this feature was a cold front (Fig. 3.5). The maximum wind speed of the upper-tropospheric jet poleward of TC Camille had strengthened to 55 m s^{-1} (Fig. 3.5), which was a response to an increase in the upper-level PV gradient over the Canadian Maritimes (not shown).

3.2.2. PV Analysis

As previously discussed in Chapter 1, the structure of the midlatitude circulation into which a TC travels has been shown to determine whether the TC strengthens or weakens as it undergoes ET (e.g., Harr et al. 2000). To analyze the midlatitude

circulation observed in the TC Camille case, maps of potential temperature on the dynamic tropopause (DT), 850–200-hPa wind shear, and 925–850-hPa layer-averaged relative vorticity are displayed in Figs 3.6a, 3.7a, 3.8a, and 3.9a. The 350 K potential temperature contour separates the red from the blue shadings.

The orientation of the 350 K isentrope displays a zonal configuration of the DT poleward of TC Camille at 0600 UTC 19 August (Fig. 3.6a). A positive PV anomaly lies poleward of the 350 K isentrope in southeastern Canada (Fig. 3.6a). This positive PV anomaly was associated with the extratropical cyclone analyzed in Fig. 3.2. The position of TC Camille was approximated by the location of the $2.0 \times 10^{-4} \text{ s}^{-1}$ relative vorticity center around the Arkansas–Tennessee border (Fig. 3.6a). The quasi-symmetric structure of the relative vorticity field suggests that TC Camille was unaffected by vertical wind shear at this juncture of its lifetime over land, which is consistent with an analyzed 5 m s^{-1} value of wind shear across its circulation (Fig. 3.6a). The anticyclonic curvature of the shear vectors around TC Camille indicates that the TC warm-core structure was intact at this time. A north–south vertical cross section taken through the center of TC Camille at the same time displays PV, potential temperature, and horizontal wind speed (Fig. 3.6b). These fields show the vertical warm-core structure of TC Camille and areas where the tropopause was vertically tilted, which indicates the location of the upper-tropospheric jet core. The 1 PVU color fill extending from 925–300 hPa in the center of the cross section denotes the location of the PV column associated with TC Camille (Fig. 3.6b), which indicates a near-vertical warm-core structure of the TC. The core of the upper-tropospheric jet was still far enough to the north of TC Camille for the effect of vertical wind shear to be minimal.

By 1800 UTC 19 August, the vertical wind shear across TC Camille (7.5 m s^{-1}) (Fig. 3.7a) had increased compared to the analyzed value of vertical wind shear 12 h earlier (Fig. 3.6a). Compared to 12 h earlier (Fig. 3.6a), a less symmetric structure of the relative vorticity field associated with the TC (Fig. 3.7a) was also evident. In addition, the DT became more amplified poleward of TC Camille (Fig. 3.7a), in response to the strengthening extratropical cyclone analyzed in Fig. 3.3. The corresponding vertical cross section of PV and potential temperature shows that the vertical structure of TC Camille began to tilt and weaken (Fig. 3.7b) as the TC entered the higher shear environment observed in Fig. 3.7a. The core of the upper-tropospheric jet, which was characterized by a maximum wind speed of 30 m s^{-1} at approximately 200 hPa, was analyzed poleward of TC Camille, as indicated by the vertically tilted tropopause centered around 200 hPa (Fig. 3.7b).

Compared to 12 h earlier (Fig. 3.7a), the vertical wind shear (10 m s^{-1}) analyzed across TC Camille at 0600 UTC 20 August (Fig. 3.8a) had increased. As a result of the increased vertical wind shear over TC Camille, the low-level circulation of TC Camille weakened, as indicated by the reduced magnitude of the relative vorticity field centered along the central Appalachian Mountains (Fig. 3.8a). A quasi-stationary positive PV anomaly associated with the extratropical cyclone northeast of the TC was centered over Quebec at this time (Fig. 3.7a). Compared to 12 h earlier (Fig. 3.7b), the PV column associated with TC Camille continued to weaken and tilt as the core of the upper-tropospheric jet at 200 hPa strengthened to 35 m s^{-1} and moved to within 550 km of TC Camille (Fig. 3.8b). Wind speed values up to 20 m s^{-1} were situated at 200 hPa above the

central circulation of TC Camille (Fig. 3.8b), indicative of the increasing shear affecting the TC compared to 12 h earlier (Fig. 3.7b).

The quasi-stationary positive PV anomaly continued to be centered in Quebec at 1800 UTC 20 August, and the low-level circulation of TC Camille strengthened compared to 12 h earlier (Fig. 3.8a) as the TC exited the East Coast of the United States (Fig. 3.9a). However, the structure of the low-level circulation associated with TC Camille suggests that the TC was undergoing ET as indicated by the increasingly asymmetric structure of the relative vorticity field associated with the TC (Fig. 3.9a). Although the corresponding vertical cross section is similar to that in Fig. 3.8b, the core of the upper-tropospheric jet poleward of TC Camille had strengthened to 40 m s^{-1} at 200 hPa (Fig. 3.9b). In addition, the upper-tropospheric jet core was approximately 450 km from the TC Camille circulation (Fig. 3.9b), which is closer than displayed in Fig. 3.8b.

The position of the PV anomaly to the northeast of TC Camille is consistent with the northeast pattern documented by Harr et al. (2000), which results in a poleward-moving TC weakening or remaining the same intensity as it undergoes ET. In this pattern, there is typically a quasi-stationary extratropical cyclone to the northeast of the TC, which is similar to that observed in the TC Camille case.

3.2.3. Low-Level Structure and Moisture Evolution

The low-level structure and moisture evolution of TC Camille is documented using maps of precipitable water (PW), 925-hPa geopotential height, 925-hPa wind, 925-hPa potential temperature, and 700-hPa upward vertical motion (Figs. 3.10–3.13). At 0600 UTC 19 August, a closed, symmetric circulation associated with TC Camille was

analyzed at 925 hPa near the junction of the Mississippi River and Ohio River (Fig. 3.10). In addition, PW values in excess of 50 mm were analyzed in and around the TC circulation (Fig. 3.10). Values of PW in excess of 50 mm, likely transported from the Gulf of Mexico towards the Ohio River Valley and mid-Atlantic regions, were associated with southerly flow ahead of TC Camille and behind a broad anticyclonic circulation off the coast of the southeastern United States (Fig. 3.10). A baroclinic zone at 925 hPa, indicated by the tight packing of isentropes in the Great Lakes region (Fig. 3.10), is associated with the aforementioned lower-tropospheric baroclinic zone analyzed in Fig. 3.2. The edge of this lower-tropospheric baroclinic zone is approximated by the 300 K isentrope (Fig. 3.10)

By 1800 UTC 19 August, the lower-tropospheric baroclinic zone in the Great Lakes had moved southeastward into the northeastern United States, and the southerly flow from the Gulf of Mexico likely continued to transport high values of moisture toward west-central Virginia (Fig. 3.11). The 300 K isentrope associated with the lower-tropospheric baroclinic zone was 400 km closer to TC Camille (Fig. 3.11) compared to 12 h earlier (Fig. 3.10), which shows the TC was approaching a baroclinic environment. A broad area of upward vertical motion observed over and to the northeast of TC Camille (Fig. 3.11) was associated with ascent in the equatorward entrance region of the upper-tropospheric jet poleward of the TC. In addition, a broad area of stratiform precipitation in Indiana, Ohio, Kentucky, and West Virginia (not shown) likely contributed to the broad area of upward vertical motion (Fig. 3.11).

As TC Camille crossed the Appalachian Mountains at 0600 UTC 20 August, the heaviest rainfall occurred over west-central Virginia. Compared to 12 h earlier (Fig.

3.11), increased baroclinicity was analyzed at 925 hPa across northern Virginia as the edge of the lower-tropospheric baroclinic zone, indicated by the 300 K isentrope, moved into northern Virginia (Fig. 3.12). The closed circulation associated with TC Camille became elongated and exhibited a southwest–northeast tilt at this time (Fig. 3.12). Southerly flow ahead of TC Camille was associated with a rich moisture supply (PW values greater than 50 mm) in west-central Virginia (Fig. 3.12). In this region, the Blue Ridge Mountains induced an upslope component of the wind, and the moist environment already present allowed for heavy rainfall to be generated over west-central Virginia. A thermodynamic diagram from Sterling, Virginia, at 0700 UTC 20 August, presented in Schwartz (1970), shows a moist neutral thermodynamic environment over the region (not shown), which supported deep rising motion and convection. Convergence of the flow at 925 hPa is implied over this region, where northerly winds on the cold side of the lower-tropospheric baroclinic zone converged with the southerly winds on the warm side of this baroclinic zone (Fig. 3.12). This implied convergence, the upslope component of the wind induced by the Blue Ridge Mountains, and the ascent located underneath the equatorward entrance region of the upper-tropospheric jet, worked in concert to support the heavy rainfall observed across west-central Virginia.

As previously mentioned, at 1800 UTC 20 August, TC Camille was already undergoing ET, and Fig. 3.13 shows the cooler air being advected into the northwest quadrant of TC Camille. The PW field indicated the ongoing ET process as well, where dry (moist) air was analyzed west (east) of TC Camille (Fig. 3.13). Fig. 3.13 shows that the TC circulation at 925 hPa continued to exhibit a southwest–northeast tilt and had not intensified when compared to 12 h earlier (Fig. 3.12), which was consistent with the

minimal strengthening of TC Camille as it moved off the East Coast of the United States (Fig. 3.13).

3.3. Mesoscale Overview

3.3.1. *Precipitation Evolution*

The evolution of heavy rainfall over Nelson County, Virginia, whose location is denoted by a yellow star on the following radar summary charts (Figs. 3.14–3.20), is documented for the 12-h period of heaviest rainfall (stated in section 3.1.2) across Nelson County. At 2245 UTC 19 August, showers and thunderstorms were observed over the central mid-Atlantic (Fig. 3.14). This area of rainfall was associated with the southward-moving lower-tropospheric baroclinic zone (Figs. 3.10–3.12). A line of showers and thunderstorms west of the central Appalachian Mountains (left side of Fig. 3.14) was indicated as an echo area and was associated with the TC Camille circulation. Although not shown in Fig. 3.14, much of the rainfall associated with TC Camille was shifted towards the northeast side of the circulation as a result of synoptic-scale forcing for ascent beneath the equatorward entrance region of the upper-tropospheric jet poleward of the TC (Fig. 3.4).

At 0045 UTC 20 August, the showers and thunderstorms associated with the lower-tropospheric baroclinic zone were situated over west-central Virginia (Fig. 3.15). In this region, rainfall was observed in 60–90% of an echo area and was identified as an area of heavy showers and thunderstorms (Fig. 3.15). A maximum echo top of approximately 10.7 km was observed around the Nelson County area, which confirmed the presence of convection (Fig. 3.15). Meanwhile, the rainfall west of the central

Appalachian Mountains showed signs of weakening, as indicated by reports of light rain showers in eastern Kentucky (Fig. 3.15).

Heavy showers and thunderstorms continued in west-central Virginia at 0245 UTC 20 August, where four maximum echo tops were observed near the Nelson County area (Fig 3.16). Two of these maximum echo tops extended to 11.3 km, while one of these echo tops was observed to be approximately 10.7 km. A 10.4 km echo top was observed in eastern Virginia (Fig. 3.16). An area of showers and thunderstorms covering 30–50% of an echo area southwest of west-central Virginia was observed (Fig. 3.16), but was weakening after developing just an hour earlier (not shown). An analysis of subsequent radar summary charts from 0645 UTC 20 August–0845 UTC 20 August (Figs. 3.17–3.19) shows this area of rainfall to be quasi-stationary and rather weak. Although synoptic-scale forcing for ascent was focused poleward of this area of rainfall (Fig. 3.12), the presence of this rainfall suggests that instability provided by the warm, moist environment in this region ahead of TC Camille was sufficient to produce this area of rainfall.

By 0445 UTC 20 August, heavy showers and thunderstorms were evident across west-central Virginia (Fig. 3.17). Maximum echo tops of 12.2 km were being observed to the east of Nelson County (Fig. 3.17) as the lower-tropospheric baroclinic zone in northern Virginia (Fig. 3.12) continued to be a focus for heavy rainfall. At this time, the central circulation of TC Camille began crossing the central Appalachian Mountains in southern West Virginia (Fig. 3.17).

Ending at 0645 UTC 20 August, the rainfall associated with the TC finished consolidating with the rainfall associated with the lower-tropospheric baroclinic zone

(Fig. 3.18), which had started at 2245 UTC 19 August (Fig. 3.14). Heavy showers and thunderstorm continued to be indicated in west-central Virginia; however, a maximum echo top of 9.1 km observed to the north of the Nelson County area was the closest maximum echo top (Fig. 3.18).

The western edge of rainfall was located in western Virginia at 0845 UTC 20 August as TC Camille was crossing south-central Virginia (Fig. 3.19). The coverage of rainfall across Nelson County was greater than 90%, with heavy showers and thunderstorms being indicated in the area, and 11.9 km maximum echo tops were observed east of Nelson County (Fig. 3.19).

By 1045 UTC 20 August, the rainfall in west-central Virginia had ended as TC Camille moved away from the region (Fig. 3.20). Heavy showers and thunderstorms were indicated in eastern Virginia, Maryland, and Delaware, where an echo area in that region had 60–90% echo coverage (Fig. 3.20). Echo tops of 11.9 km continued to be observed, but were east of the Nelson County area and were located in eastern Virginia and southern Maryland (Fig. 3.20).

3.3.2. Surface Analysis

A surface baroclinic zone, which strengthened due to differential surface heating during the day of 19 August, was observed across west-central Virginia at 0000 UTC 20 August, whereas a synoptically-produced surface baroclinic zone was positioned across central Pennsylvania and northern Ohio (Fig. 3.21). Observed dewpoint depressions of 0–1°C at various stations throughout West Virginia and northern Virginia (Fig. 3.21) indicate the presence of rainfall at this time, as shown in Fig. 3.14. Warm, moist south-

southeasterly flow ahead of TC Camille, which was positioned in central Kentucky at this time, provided an upslope component of the wind across Nelson County (Fig. 3.21). This stream of warm, moist flow provided sufficient instability to maintain convection in west-central Virginia over the next 12 h.

The surface map for 0600 UTC 20 August indicates that the synoptically-produced surface baroclinic zone moved south across northwest Virginia, where it merged with the circulation of TC Camille (Fig. 3.22). Compared with Fig. 3.21, an increase of the surface temperature gradient associated with the surface baroclinic zone implied that frontogenesis had occurred in northwest Virginia during the 6-h period ending 0600 UTC 20 August (Fig. 3.22). The position of the surface baroclinic zone with respect to Nelson County put it at the edge of the surface baroclinic zone, where surface temperature and dewpoint values were approximately 24°C and 22°C, respectively, at this time (Fig. 3.22). The approximate location of TC Camille, as indicated by the MSLP field, was in southwestern Virginia (Fig. 3.22). The southerly winds observed at various stations in North Carolina continued to transport warm, moist air towards the surface baroclinic zone (Fig. 3.22). The surface flow across Nelson County is difficult to assess since the Lynchburg, Virginia, observation is not available, so station observations close to Nelson County were used. The light northeasterly surface wind at Roanoke, Virginia, southwest of Nelson County, indicates the passage of the surface baroclinic zone, whereas a south-southeasterly surface wind observed at Richmond, Virginia, east-southeast of Nelson County, supports the idea that an upslope component of the wind continues to be directed towards Nelson County (Fig. 3.22).

By 1200 UTC 20 August, TC Camille was located over eastern Virginia, and its minimum central MSLP had decreased to 1004 hPa (Fig. 3.23). TC Camille had started ET at this time, as indicated by an intrusion of cool, dry air into the northwest quadrant of the circulation, as well as implied warm-air advection, shown by the quasi-perpendicular orientation of isotherms with respect to sea level isobars, ahead of TC Camille (Fig. 3.23). The surface baroclinic zone situated over eastern Virginia, southern Maryland, and southern Delaware, implied as the surface warm front, continued to be a focus for heavy rainfall, as indicated by the heavy showers and thunderstorms observed over the region (Fig. 3.20).

3.3.3. *Frontogenesis and Ageostrophic Circulation Analysis*

North–south vertical cross sections taken through Nelson County during the 12-h period of heaviest rainfall (stated in section 3.1.2) depict Petterssen frontogenesis, potential temperature, horizontal wind speed, and the ageostrophic wind component tangential to the cross section (Figs. 3.24–3.26). Starting at the time when heavy rainfall began across Nelson County at 0000 UTC 20 August, a 45 m s^{-1} upper-tropospheric jet was observed poleward of Nelson County (Fig. 3.24). Lower-tropospheric frontogenesis, indicated by values of $2 \text{ K (100 km)}^{-1} (3 \text{ h})^{-1}$, was observed poleward of Nelson County. The axis of frontogenesis tilted towards colder air, with maximum frontogenesis observed at 700 hPa and 250 hPa (Fig. 3.24). The surface baroclinic zone was observed poleward of Nelson County, as indicated by a gradient of isentropes at the surface (Fig. 3.24).

An environment favorable for heavy rainfall over Nelson County peaked at 0600 UTC 20 August (Fig. 3.25). Frontogenesis located over the area again tilted toward cold

air and was maximized at 850 hPa and 300 hPa (Fig. 3.25). The warm edge of the surface baroclinic zone, located near Nelson County as depicted in the vertical cross section (Fig. 3.25), is consistent with the surface analysis in Fig. 3.22. The location of the upper-tropospheric jet poleward of Nelson County placed this location in the equatorward entrance region of the upper-tropospheric jet, where observed diverging ageostrophic winds at 200 hPa imply upward vertical motion below this level (Fig. 3.25). The lower-tropospheric frontogenesis and the position of Nelson County in the equatorward entrance region of an upper-tropospheric jet combined to produce tropospheric-deep ascent over this location, which was maximized at 700 hPa (Fig. 3.25). The presence of this tropospheric-deep ascent in a warm, moist environment provided support for the generation of heavy rainfall over west-central Virginia.

By 1200 UTC 20 August, lower values of upward vertical motion and frontogenesis were observed over Nelson County (Fig. 3.26) compared to 6 h earlier at 0600 UTC 20 August. The surface baroclinic zone, indicated by the gradient of isentropes at the surface, was positioned farther south as cool air wrapped into the northwest quadrant of TC Camille, indicating that the TC was starting ET at this time (Fig. 3.26).

3.4. Summary

After making landfall in southeastern Louisiana as a category 5 hurricane, TC Camille weakened rapidly into a tropical depression as it tracked northward towards the Ohio River Valley (Fig. 3.1). By 0000 UTC 20 August, TC Camille had made an eastward turn toward west-central Virginia (Fig. 3.1) as it became influenced by the

midlatitude flow poleward of the TC. As TC Camille interacted with a lower-tropospheric baroclinic zone moving south from the northeastern United States early on 20 August, inland flooding ensued as copious amounts of rain fell over Nelson County, Virginia. In the 12-h period ending 1200 UTC 20 August, nearly 690 mm of rain fell over Massies Mill in Nelson County, leading to severe inland flooding, and resulting in 153 fatalities.

An analysis of the inland flooding associated with the passage of TC Camille shows that the heavy rainfall over west-central Virginia can be attributed to several factors. First, tropospheric-deep ascent beneath the equatorward entrance region of a downstream 45 m s^{-1} upper-tropospheric jet (Fig. 3.4) provided support for heavy rainfall over west-central Virginia. Second, frontogenesis and mesoscale ascent associated with the lower-tropospheric baroclinic zone poleward of TC Camille (Fig. 3.25) provided additional support for heavy rainfall. Third, a warm, moist lower-tropospheric southerly flow ahead of TC Camille (Fig. 3.12) ascended the lower-tropospheric baroclinic zone and sustained the convection observed across west-central Virginia. This setup is similar to a training line/adjoining stratiform mode of MCS organization that forms in a very moist, unstable environment on the cool side of a preexisting slow-moving surface boundary (Schumacher and Johnson 2005). Fourth, surface analyses confirmed the presence of an upslope component of the surface wind directed towards the Blue Ridge Mountains of west-central Virginia (Figs. 3.21–3.22), which contributed to the heavy rainfall during the passage of TC Camille across the Appalachian Mountains during 20 August.

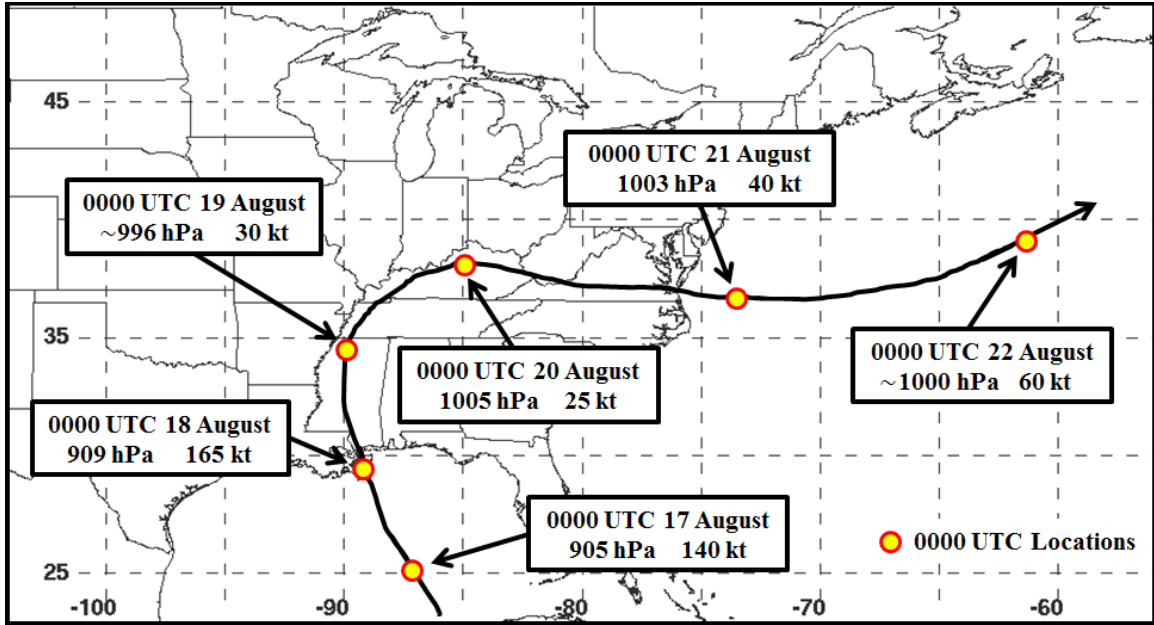


Fig. 3.1. TC Camille track map displaying maximum sustained wind speed and minimum central MSLP observations at 0000 UTC for 17–22 August 1969. 0000 UTC locations are denoted by yellow circles with a red outline.

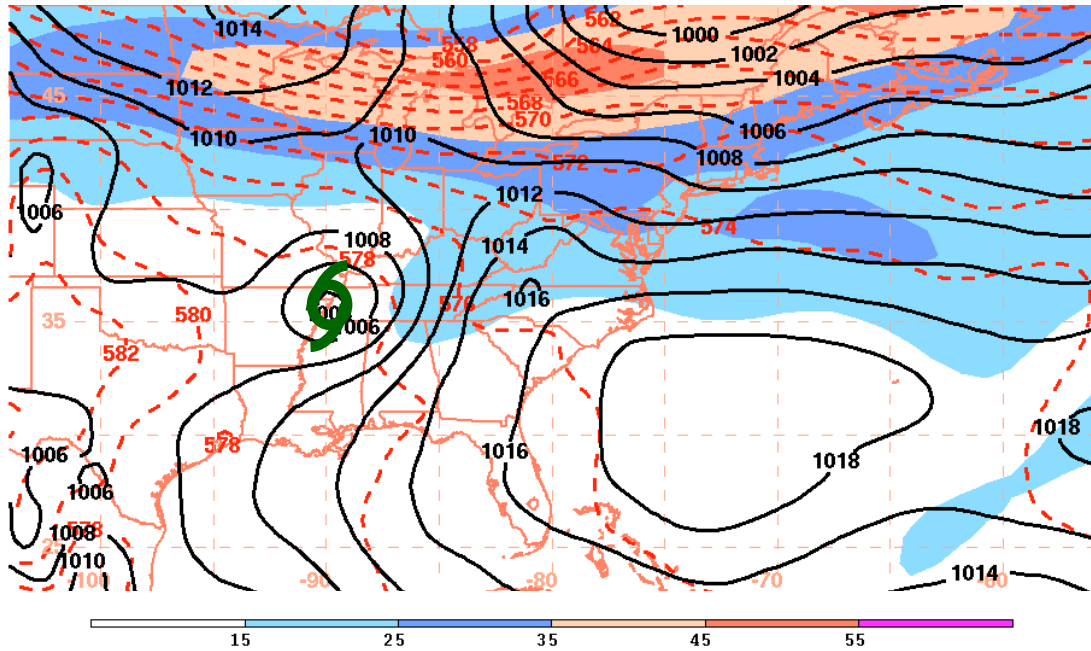


Fig. 3.2. Map of 250-hPa wind speed (shaded, m s^{-1}), 1000–500-hPa thickness (dashed red every 2 dam), and MSLP (solid black every 2 hPa) at 0600 UTC 19 August 1969. The green TC symbol denotes the position of TC Camille as depicted by the ERA-40.

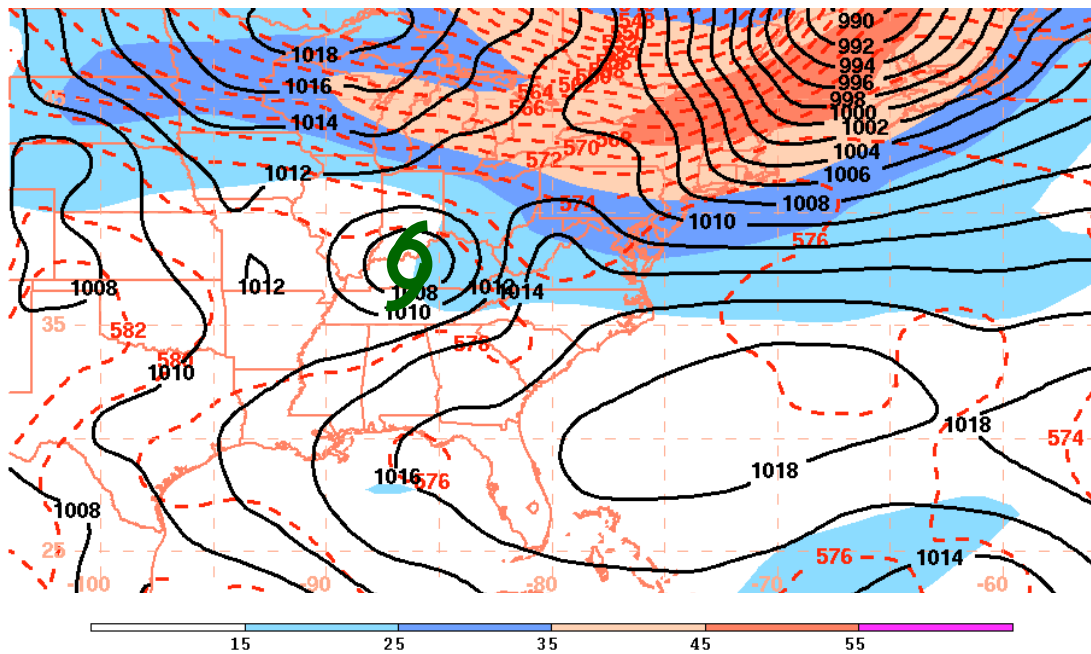


Fig. 3.3. Same as Fig. 3.2., except at 1800 UTC 19 August 1969.

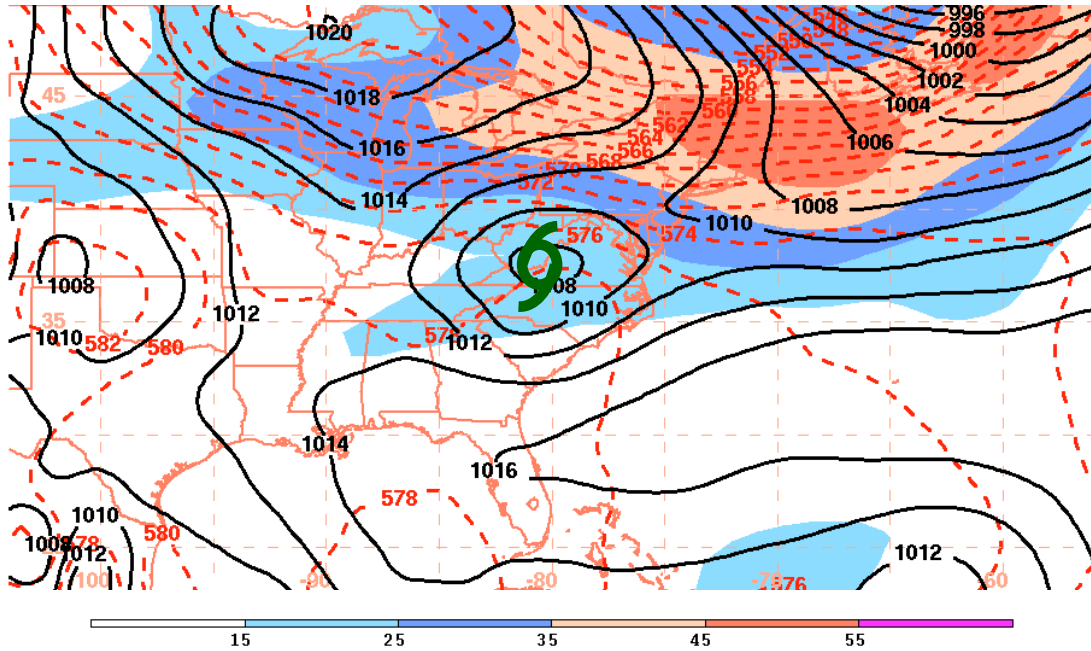


Fig. 3.4. Same as Fig. 3.2., except at 0600 UTC 20 August 1969.

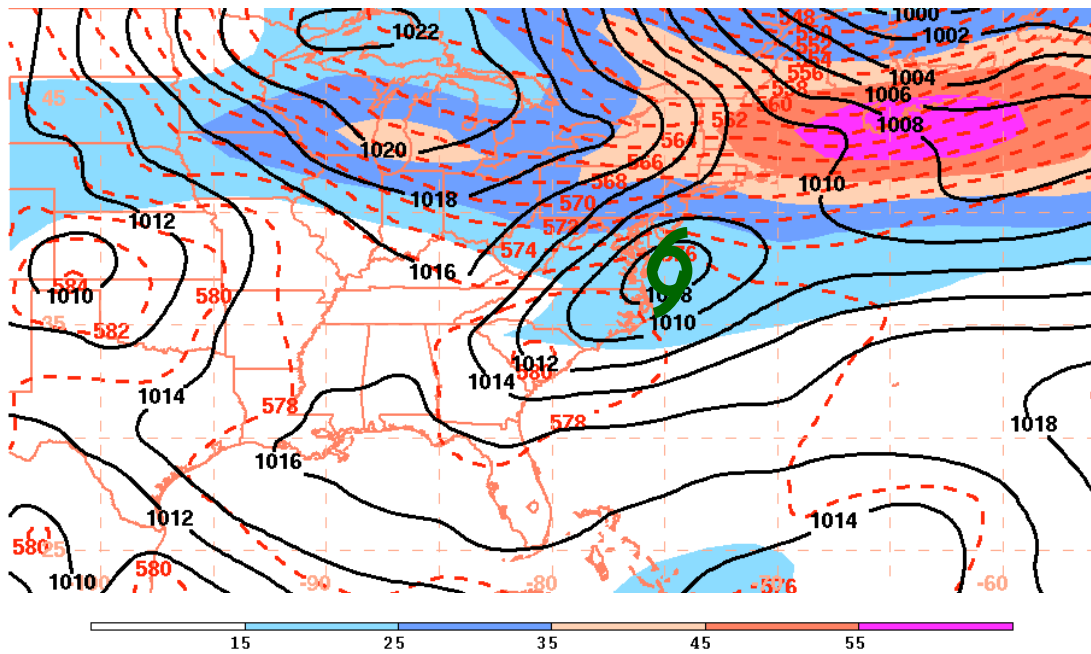


Fig. 3.5. Same as Fig. 3.2., except at 1800 UTC 20 August 1969.

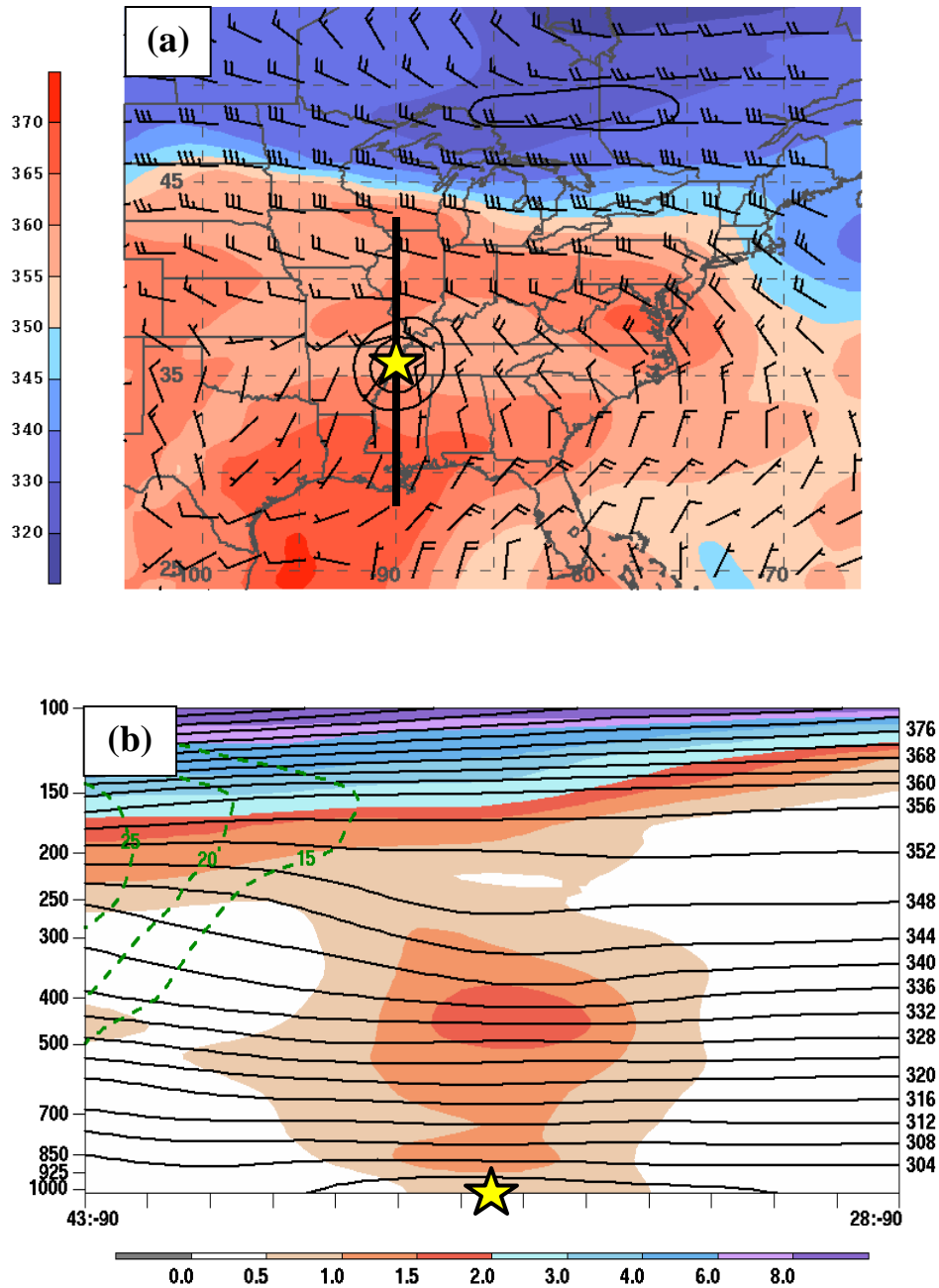


Fig. 3.6. (a) Map of potential temperature on the 2 PVU surface (shaded every 5 K; every 10 K below 340 K), 850–200-hPa wind shear (barbs, kt), and 925–850-hPa layer-averaged relative vorticity (solid black every $0.5 \times 10^{-4} \text{ s}^{-1}$ starting at $0.5 \times 10^{-4} \text{ s}^{-1}$) at 0600 UTC 19 August 1969. The yellow star denotes the position of TC Camille as depicted by the ERA-40. The black line denotes the location of the vertical cross section shown in Fig. 3.6b. (b) North–south vertical cross section of PV (shaded every 1 PVU), potential temperature (solid black every 4 K), and horizontal wind speed (dashed green every 5 m s^{-1} starting at 15 m s^{-1}) at 0600 UTC 19 August 1969. The yellow star denotes the location of TC Camille along the cross section.

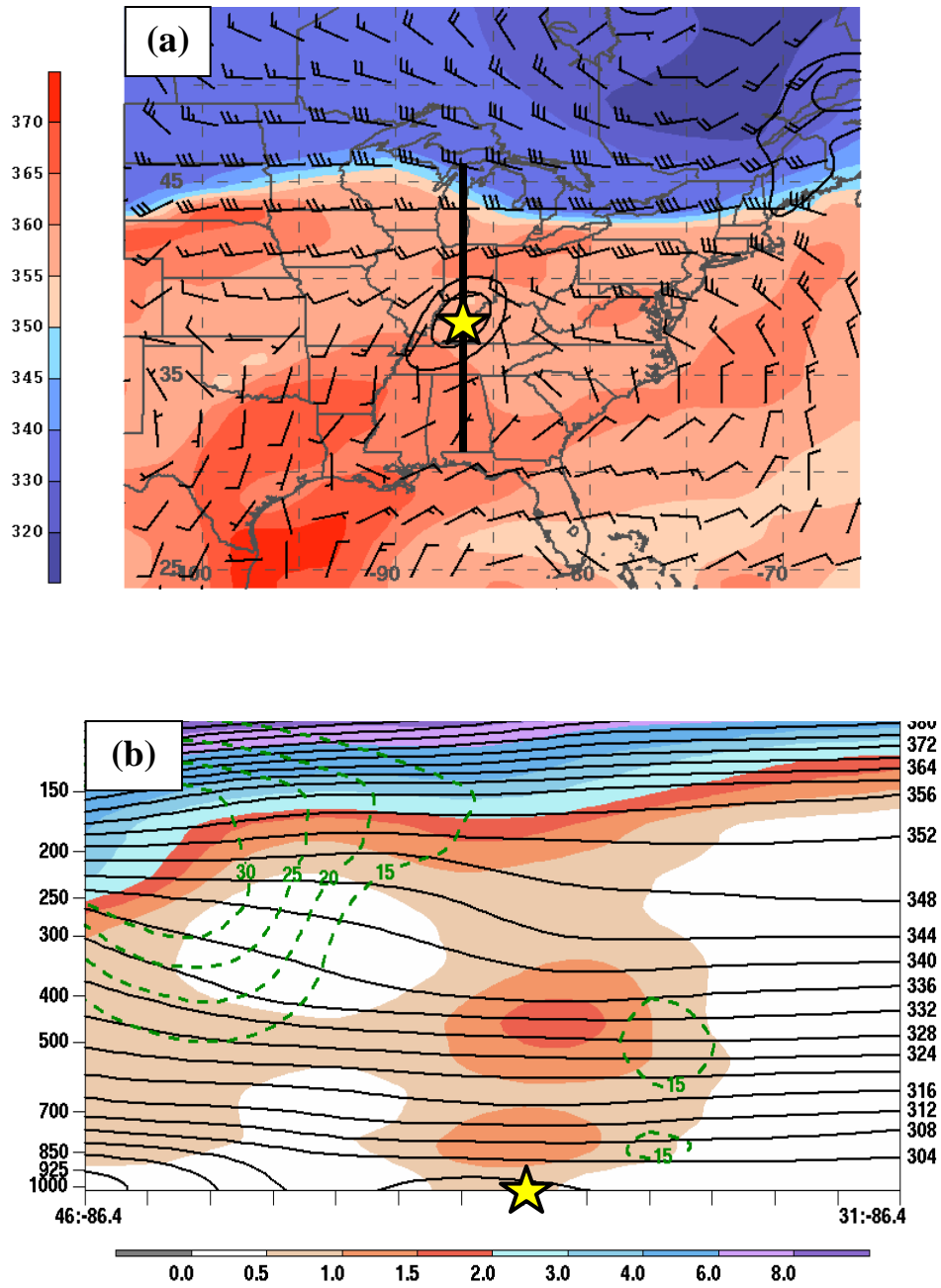


Fig. 3.7. Same as Fig. 3.6, except at 1800 UTC 19 August 1969. The black line in (a) denotes the location of the vertical cross section shown in Fig. 3.7b.

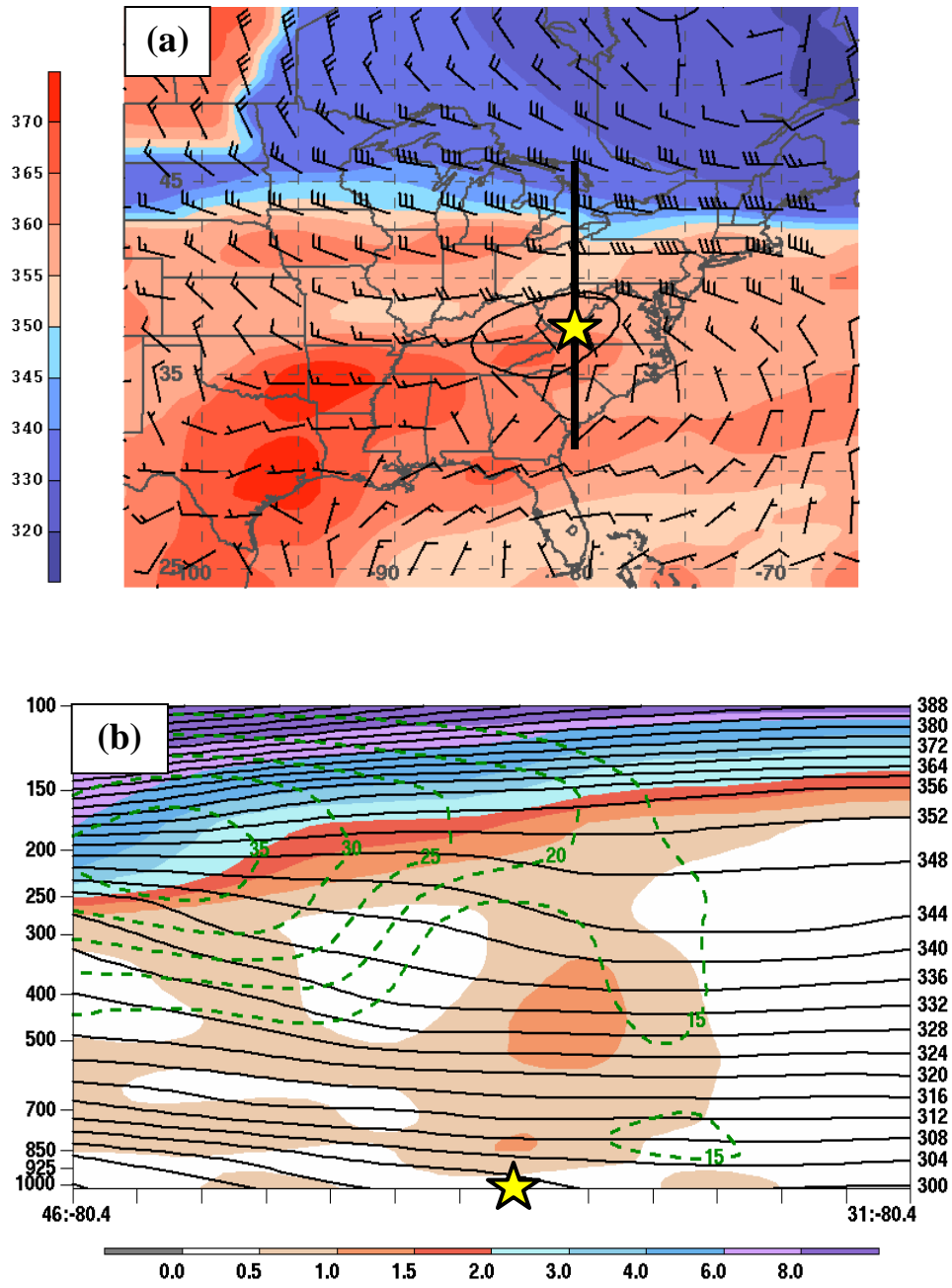


Fig. 3.8. Same as Fig. 3.6, except at 0600 UTC 20 August 1969. The black line in (a) denotes the location of the vertical cross section shown in Fig. 3.8b.

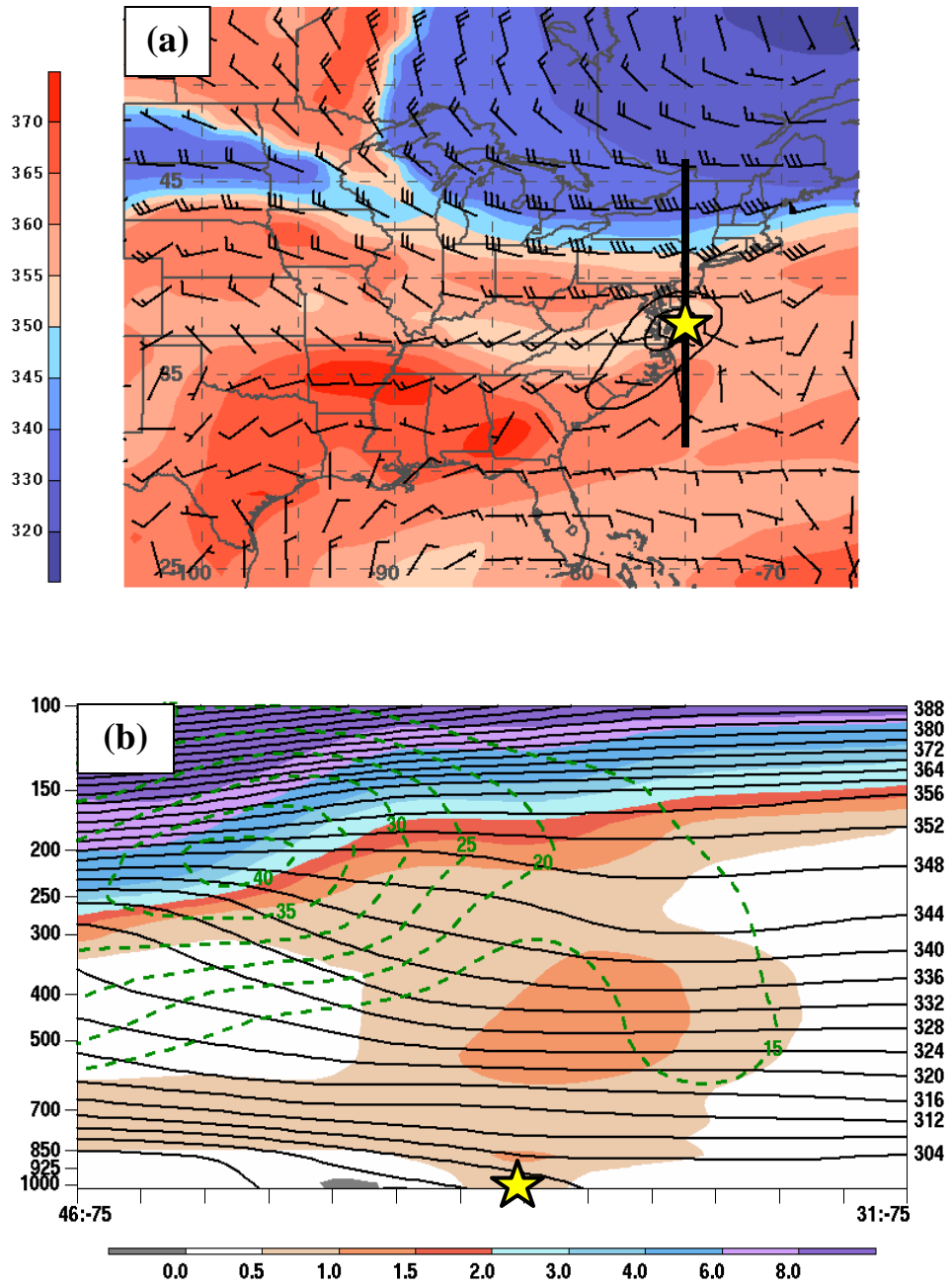


Fig. 3.9. Same as Fig. 3.6, except at 1800 UTC 20 August 1969. The black line in (a) denotes the location of the vertical cross section shown in Fig. 3.9b.

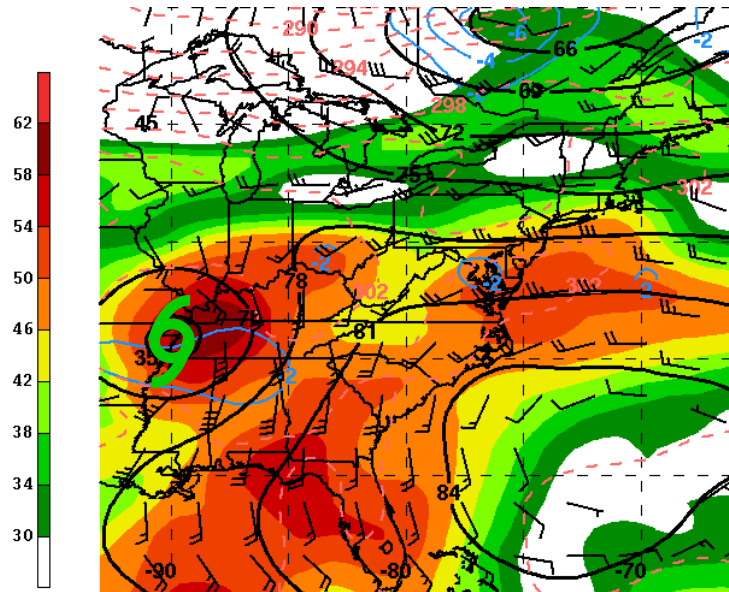


Fig. 3.10. Map of PW (shaded, mm), 700-hPa vertical motion (light blue contour every $2 \times 10^{-3} \text{ hPa s}^{-1}$, negative values only), 925-hPa geopotential height (solid black every 3 dam), 925-hPa potential temperature (dashed pink every 2 K), and 925-hPa winds (barbs, kt) at 0600 UTC 19 August 1969. The green TC symbol denotes the position of TC Camille as depicted by the ERA-40.

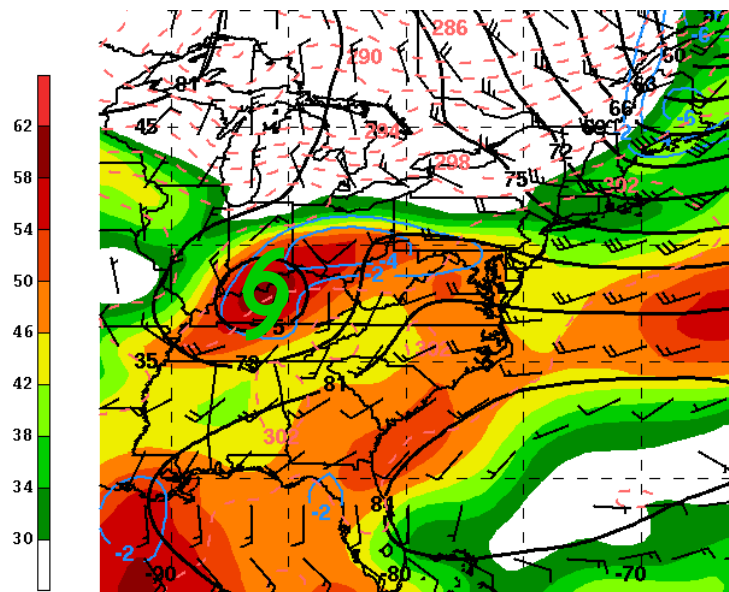


Fig. 3.11. Same as Fig. 3.10, except at 1800 UTC 19 August 1969.

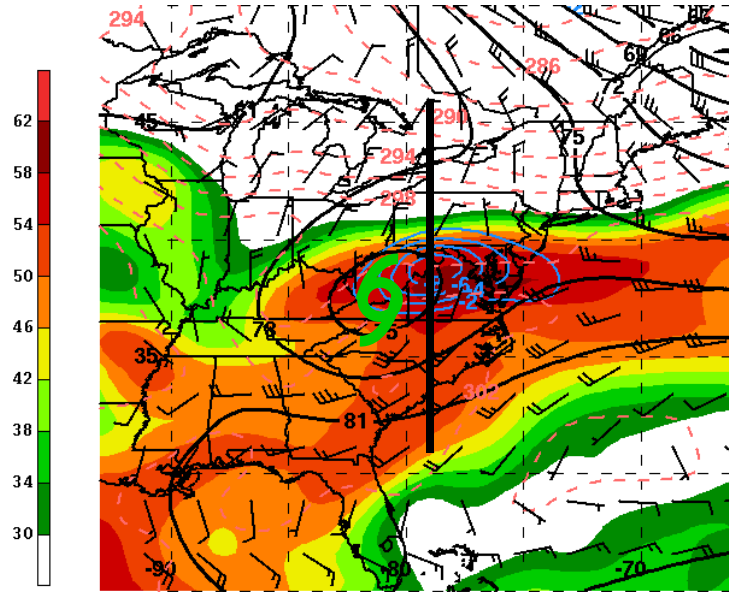


Fig. 3.12. Same as Fig. 3.10, except at 0600 UTC 20 August 1969. The black line denotes the location of the vertical cross section shown in Figs. 3.24–3.26.

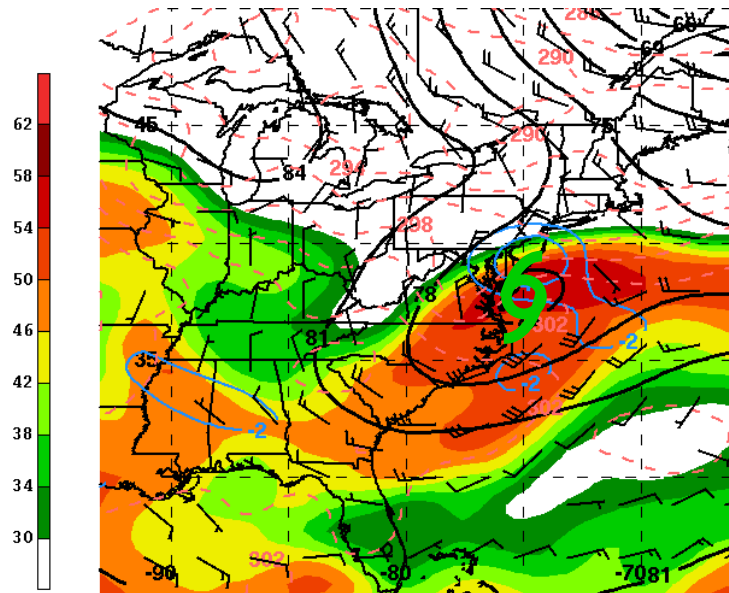


Fig. 3.13. Same as Fig. 3.10, except at 1800 UTC 20 August 1969.

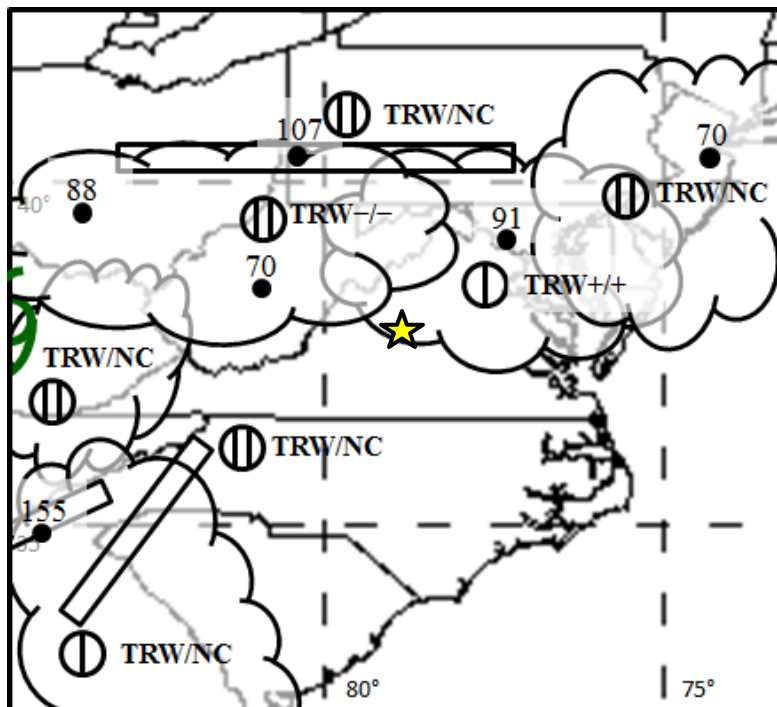


Fig. 3.14. Adapted radar summary chart at 2245 UTC 19 August 1969. The yellow star denotes the approximate location of Nelson County, Virginia. The green TC symbol denotes the position of TC Camille as depicted by the ERA-40.

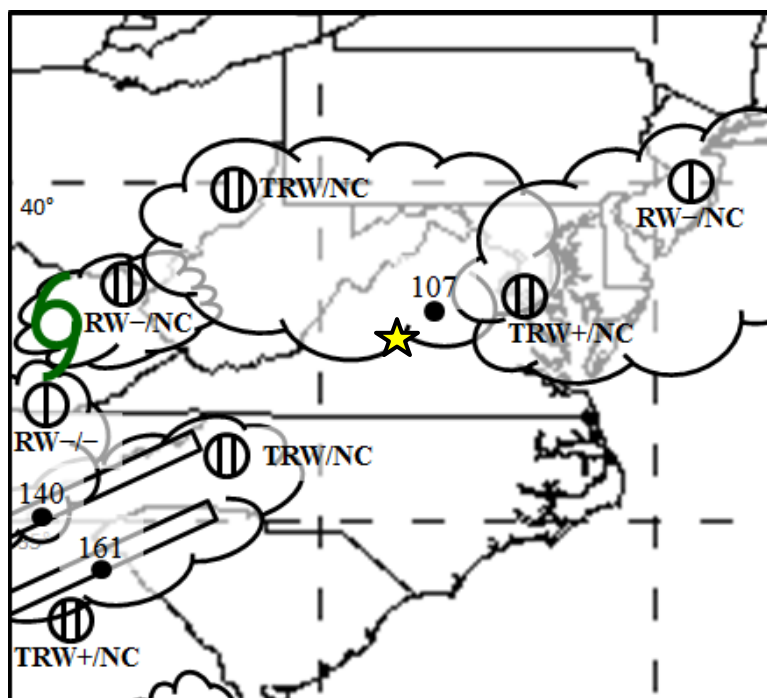


Fig. 3.15. Same as Fig. 3.14, except at 0045 UTC 20 August 1969.

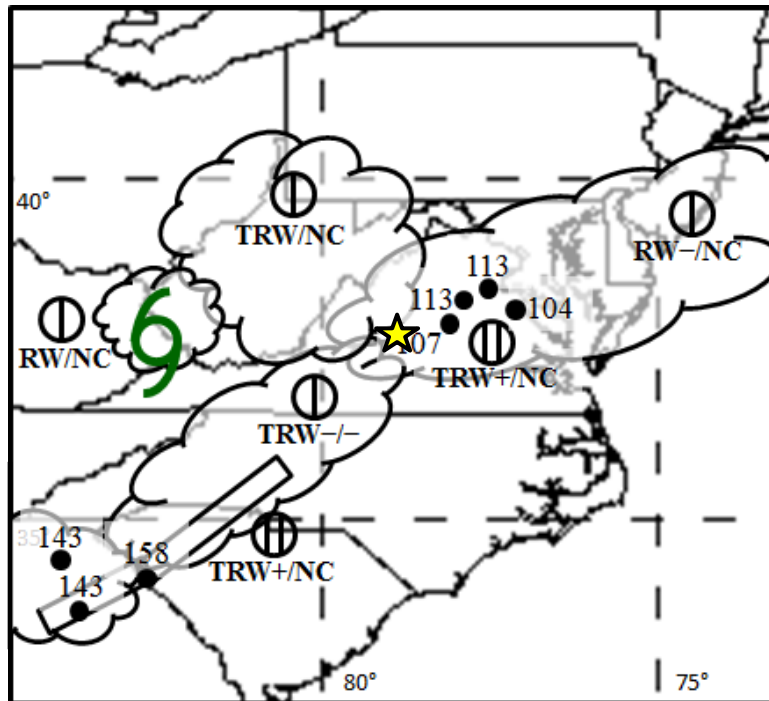


Fig. 3.16. Same as Fig. 3.14, except at 0245 UTC 20 August 1969.

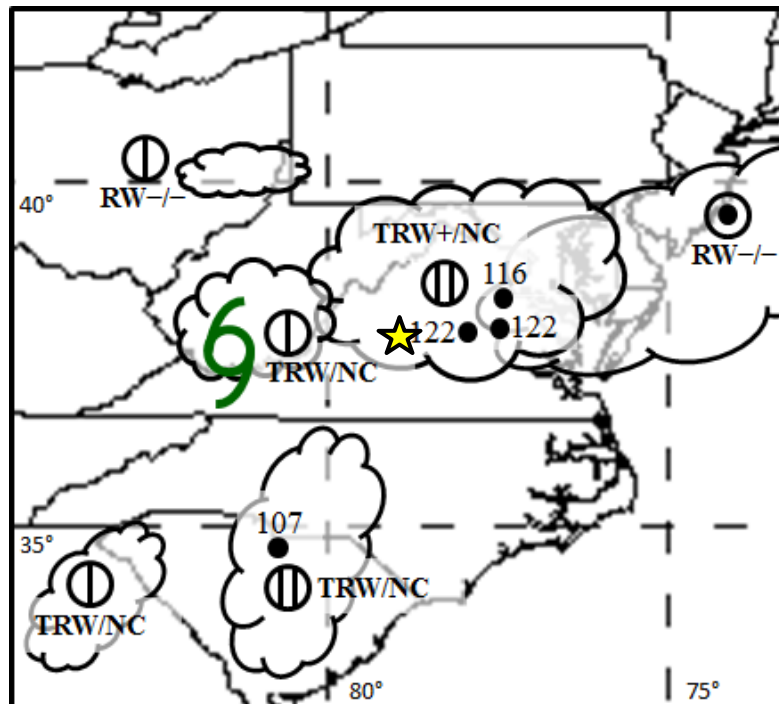


Fig. 3.17. Same as Fig. 3.14, except at 0445 UTC 20 August 1969.

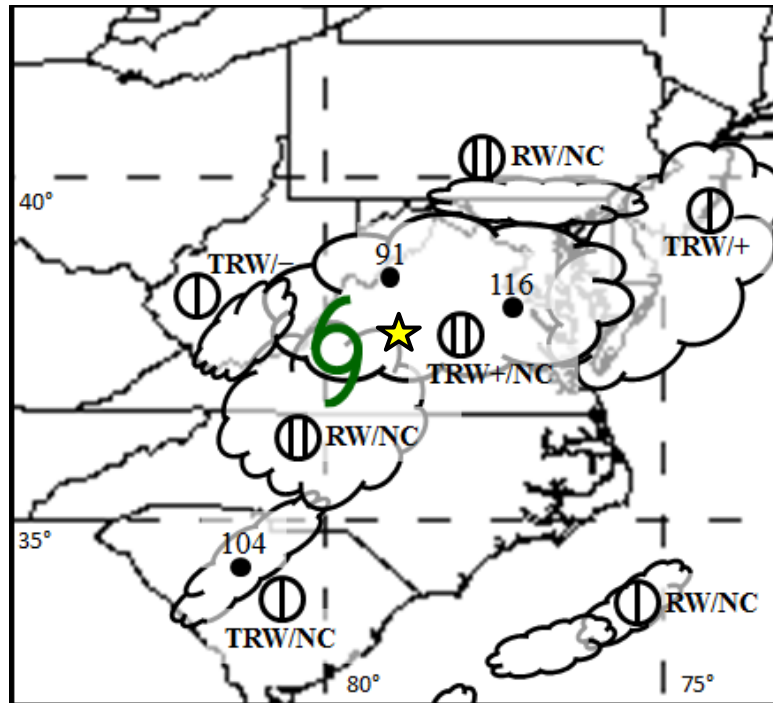


Fig. 3.18. Same as Fig. 3.14, except at 0645 UTC 20 August 1969.

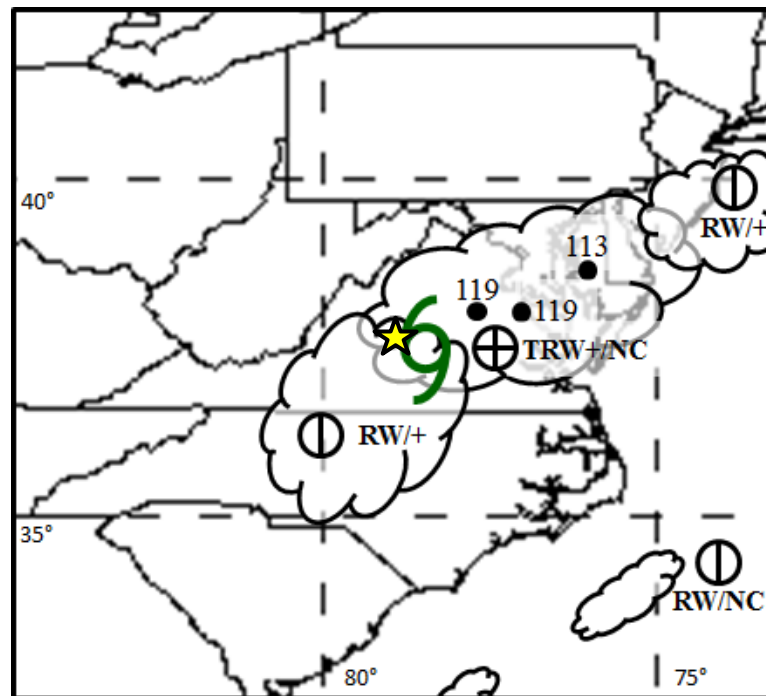


Fig. 3.19. Same as Fig. 3.14, except at 0845 UTC 20 August 1969.

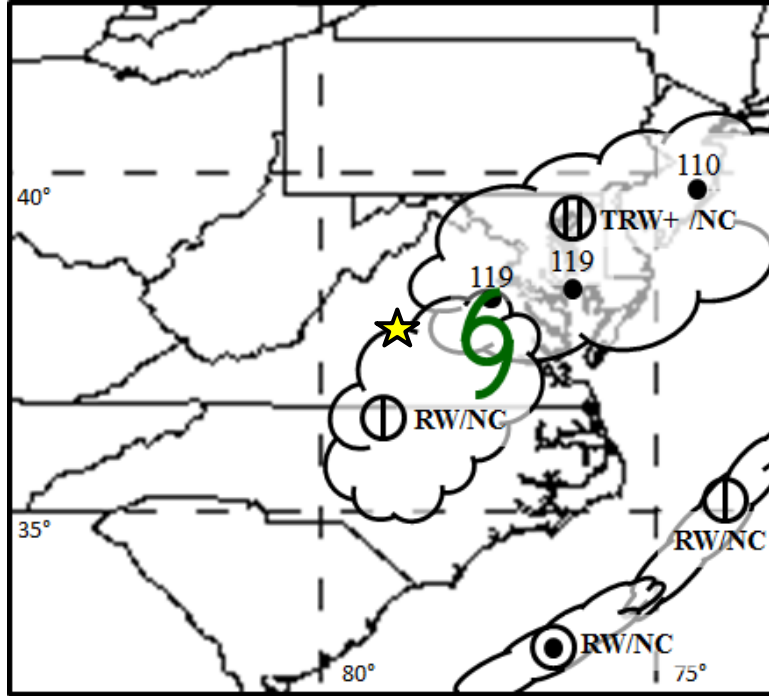


Fig. 3.20. Same as Fig. 3.14, except at 1045 UTC 20 August 1969.

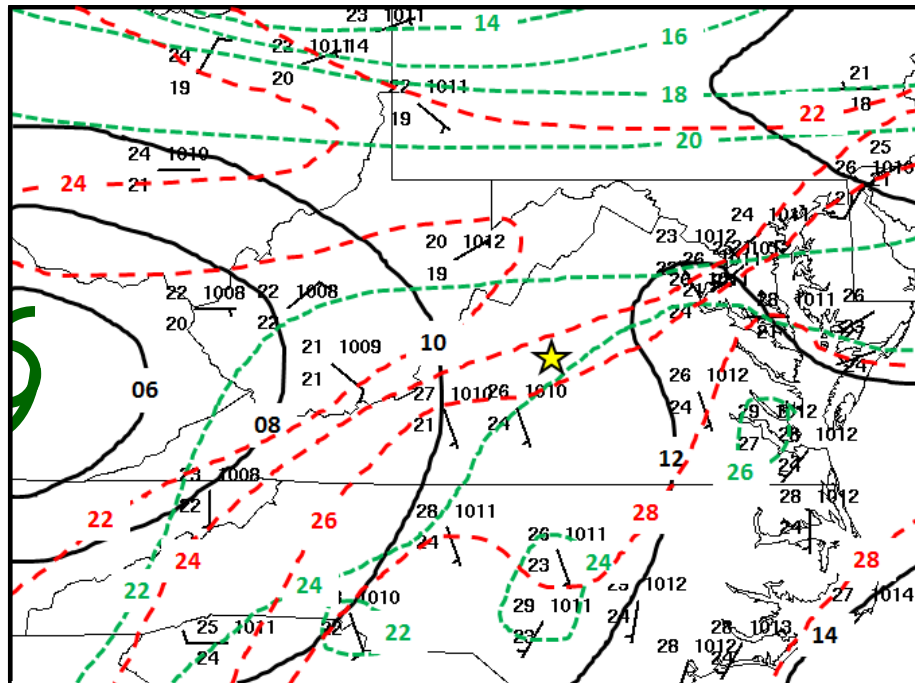


Fig. 3.21. Surface analysis at 0000 UTC 20 August 1969 displaying MSLP (solid black every 2 hPa), wind (barbs, kt), dewpoint (dashed green every 2°C), and temperature (dashed red every 2°C). The yellow star denotes the approximate location of Nelson County, Virginia. The green TC symbol denotes the position of TC Camille as depicted by the ERA-40.

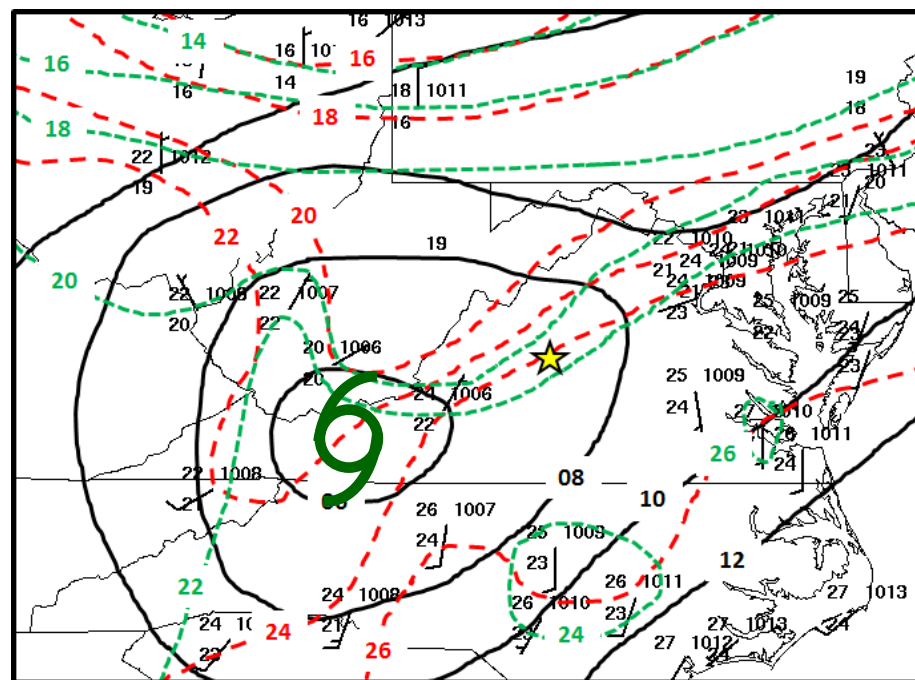


Fig. 3.22. Same as Fig. 3.21, except at 0600 UTC 20 August 1969.

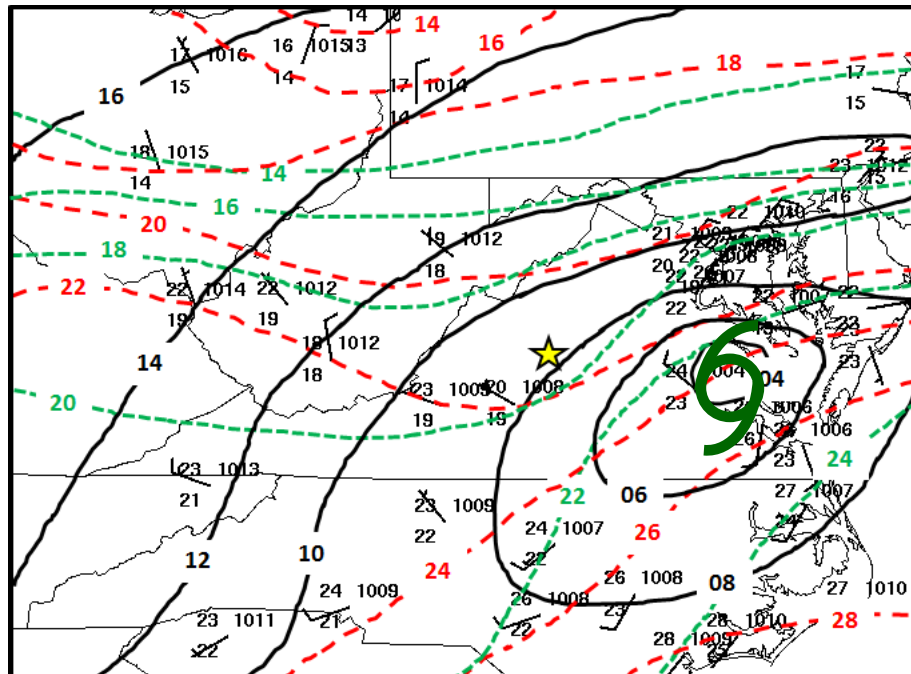


Fig. 3.23. Same as Fig. 3.21, except at 1200 UTC 20 August 1969.

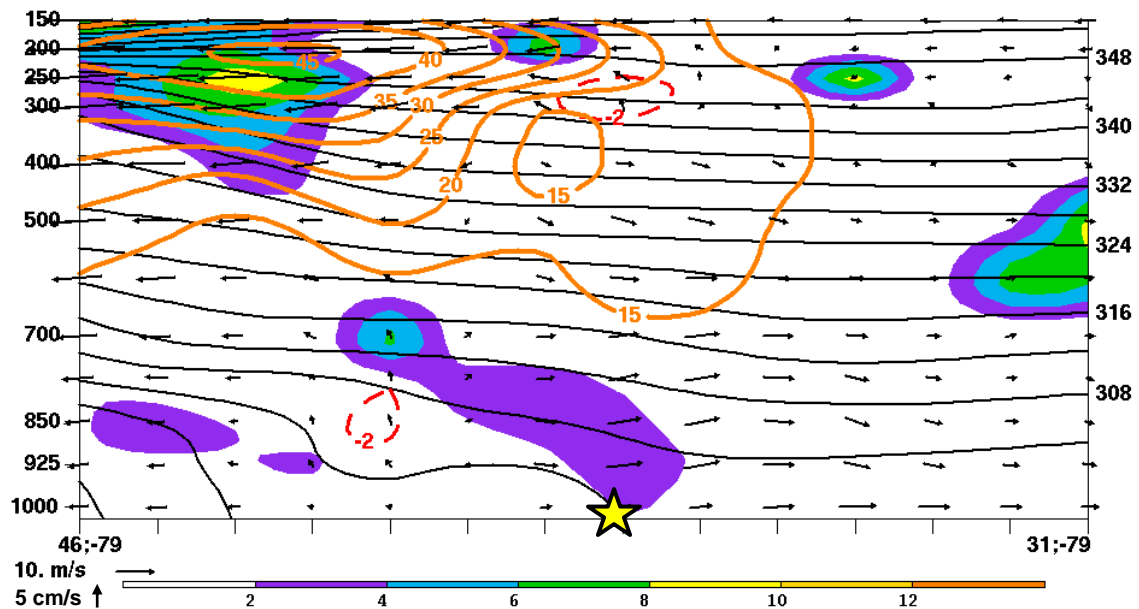


Fig. 3.24. North-south vertical cross section of Petterssen frontogenesis [shaded, $\text{K} (100 \text{ km})^{-1} (3 \text{ h})^{-1}$], potential temperature (solid black every 4 K), vertical motion (dashed red every $2 \times 10^{-3} \text{ hPa s}^{-1}$, negative values only), horizontal wind speed (solid orange every 5 m s^{-1} starting at 15 m s^{-1}) and the ageostrophic wind component tangential to the cross section (arrows, m s^{-1}) at 0000 UTC 20 August 1969. The yellow star denotes the approximate location of Nelson County along the cross section. The location of the vertical cross section is shown in Fig. 3.12.

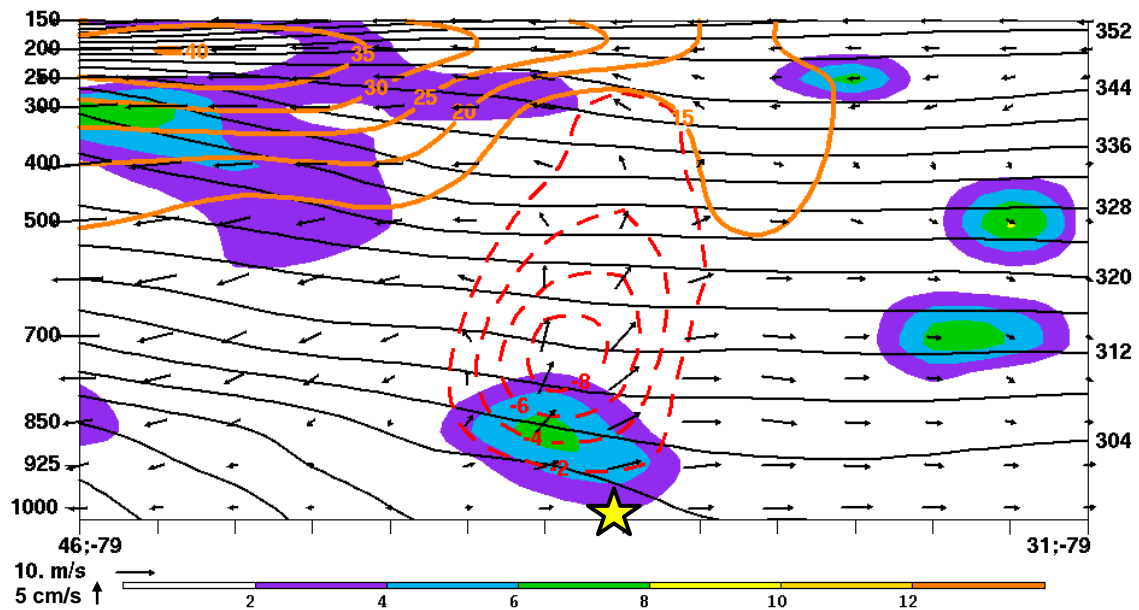


Fig. 3.25. Same as Fig. 3.24, except at 0600 UTC 20 August 1969.

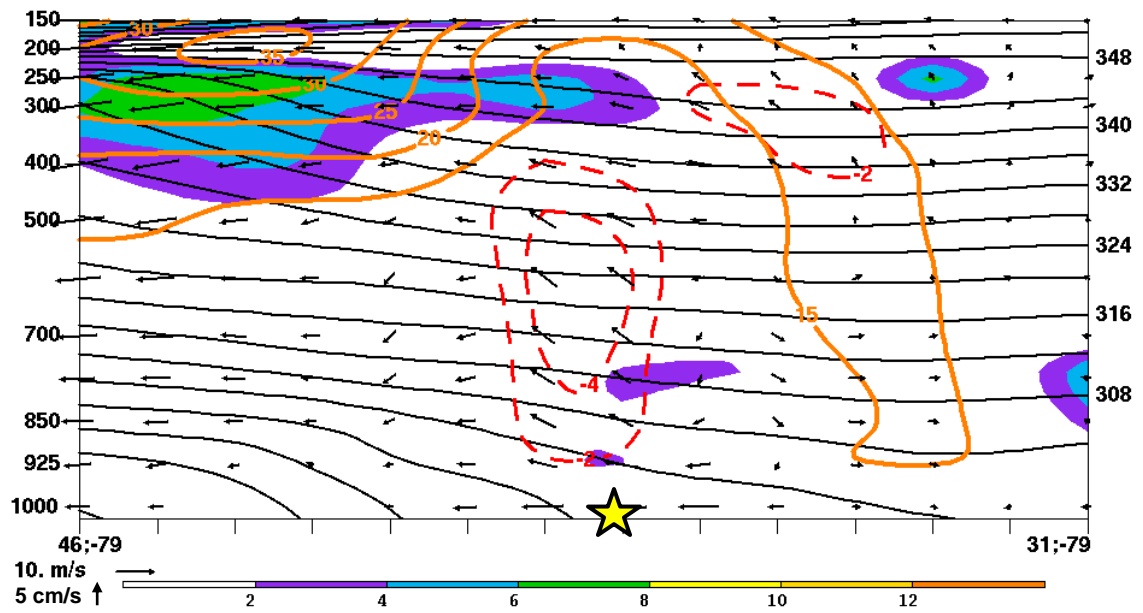


Fig. 3.26. Same as Fig. 3.24, except at 1200 UTC 20 August 1969.

4. TC Danny Multiscale Analysis

4.1. Introduction

4.1.1. TC Track

TC Danny formed as a tropical depression in the northern Gulf of Mexico at 1200 UTC 16 July 1997 and then slowly moved toward the northeast (Fig. 4.1). TC Danny quickly developed into a category 1 hurricane by 0600 UTC 18 July and subsequently made its first landfall over southeastern Louisiana approximately 6 h later (Fig. 4.1). TC Danny quickly reemerged over water and strengthened to 984 hPa with a maximum sustained wind speed of 70 kt at 0000 UTC 19 July before making its second landfall in Mobile, Alabama, later that day (Fig. 4.1). Weak steering flow around TC Danny (not shown) caused Danny to stall over southern Alabama for the next two days. By 0000 UTC 21 July, TC Danny weakened to a tropical depression and started to move towards northern Alabama (Fig. 4.1). On 23 July, TC Danny was influenced by the poleward midlatitude flow and accelerated eastward across northern Georgia. At 0000 UTC 24 July, TC Danny entered northwestern South Carolina and had an observed minimum central MSLP of 1012 hPa and a maximum sustained wind speed of 20 kt (Fig. 4.1). After 0000 UTC 24 July, TC Danny underwent inland reintensification and moved northeastward across the Carolinas. Before exiting the southeastern coast of Virginia, TC Danny regained tropical storm strength at 1800 UTC 24 July, and its minimum central MSLP decreased from 1012 hPa to 1000 hPa and its maximum sustained wind speed increased from 20 kt to 40 kt in the 18 h after 0000 UTC 24 July (Fig. 4.1). TC Danny continued to strengthen as it moved northeastward in close proximity to the coast of the northeastern United States and eventually underwent ET as it merged with an upper-level

trough off Cape Cod at about 0000 UTC 26 July (not shown). By 0000 UTC 26 July, TC Danny strengthened from 1000 hPa to 995 hPa and its maximum sustained wind speed increased from 40 kt to 45 kt in the 30 h after 1800 UTC 24 July (Fig. 4.1). Additional details on the track and evolution of TC Danny can be found in Pasch (1997) and Rappaport (1999).

4.1.2. Inland Impacts

Severe inland flooding associated with TC Danny occurred after its second landfall over southern Alabama. When Danny stalled over Mobile Bay, copious amounts of rain fell over the area. In the 72-h period starting at 1200 UTC 18 July, approximately 960 mm of rain was observed at Dauphin Island. While TC Danny was located over northern Alabama early on 23 July, a heavy rainfall event occurred in the Charlotte, North Carolina, metro area where, in the 24-h period starting 0000 UTC 23 July, over 250 mm of rain fell. The North Carolina rain event was likely associated with a PRE (Cote 2007; Galarneau et al. 2010; Moore 2010). Southerly flow ahead of TC Danny likely transported moisture from the Gulf of Mexico toward a lower-tropospheric baroclinic zone that was positioned across North Carolina (refer to section 4.2.1). In addition, the North Carolina rain area was located underneath an equatorward entrance region of a poleward upper-tropospheric jet (refer to section 4.1.4). As TC Danny traversed across the Carolinas on 23–24 July, an additional 50–100 mm of rain fell in direct association with TC Danny. These rainfall amounts were much less than those observed during the PRE event due to an acceleration of TC Danny across the Carolinas. As mentioned in section 4.1.1, TC Danny underwent inland reintensification after 0000

UTC 24 July while traversing across the Carolinas. Although the maximum sustained wind speed of TC Danny reached 40 kt before exiting the East Coast of the United States (Fig. 4.1), there were no widespread wind damage reports.

4.1.3. Historical Perspective

To assess the historical perspective of the inland reintensification of TC Danny over the Carolinas, a list of inland reintensifying TCs was produced during the 61-yr period from 1950 through 2010. A total of 27 TC candidate cases were identified subjectively to determine whether each TC underwent inland reintensification (Table I). Implementing the criteria described in chapter 2 (section 2.1) yielded a list of 10 inland reintensifying TCs (Table II). The average time between inland reintensification TC events is approximately 5 years; however, five inland reintensifying TC events occurred during the most recent 15 years of the period from 1950 through 2010. Spatially, most inland reintensifying TC events have occurred over South Carolina, North Carolina, and Virginia (Table II), a region where TCs commonly traverse when moving into the midlatitudes. The majority of inland reintensifying TC events occurred beneath an equatorward entrance region of an upper-tropospheric jet (Table II). The only TC that reintensified inland without the presence of an upper-tropospheric jet was TC Erin over Oklahoma (Evans et al. 2011). TC Erin redeveloped in the presence of a moist neutral thermodynamic environment and a southerly lower-tropospheric jet that provided moisture and generated instability in the region ahead of TC Erin. When comparing the inland reintensification of TC Danny to nine other TCs (Table II), TC Danny had the second largest decrease in minimum central MSLP (12 hPa) and second largest increase

in maximum sustained wind speed (20 kt) among the nine other inland reintensifying TCs (Table II). The largest decrease in minimum central MSLP (13 hPa) and largest increase in maximum sustained wind speed (30 kt) during inland reintensification occurred in TC Erin (Table II).

4.2. Synoptic Overview

4.2.1. Large-Scale Evolution

The relative position of TC Danny with respect to the upper-level flow and areas of synoptic-scale vertical motion (700-hPa vertical motion derived from the 2.5° NCEP–NCAR reanalysis) were analyzed for the 48-h period from 1800 UTC 22 July to 1800 UTC 24 July (Figs. 4.2–4.6). An analysis of 250-hPa wind speed, 1000–500-hPa thickness, and MSLP shows that the location of TC Danny at 1800 UTC 22 July was over north-central Alabama (Fig. 4.2a). The upper-level flow was characterized by an elongated, zonal upper-tropospheric jet about 750 km northeast of TC Danny. This upper-tropospheric jet stretched from the northern third of the United States to the northwest Atlantic Ocean (Fig. 4.2a) and was characterized by a 55 m s^{-1} wind speed maximum off the coast of the Canadian Maritimes (Fig. 4.2a). The equatorward entrance region of this upper-tropospheric jet was characterized by a broad area of upward vertical motion that was maximized to the northeast of TC Danny (Fig. 4.2b). Associated with the upper-tropospheric jet was an elongated lower-tropospheric baroclinic zone across the northern two-thirds of the United States through the northwest Atlantic Ocean, as indicated by the packing of the 1000–500-hPa thickness field in Fig. 4.2a. A 1022-hPa anticyclone, located over southern Ontario poleward of the lower-tropospheric baroclinic zone, was

positioned west of an extratropical cyclone over the Labrador Sea (not shown). Along the southern edge of the lower-tropospheric baroclinic zone was an associated surface front that extended southwestward from the extratropical cyclone as a cold front and then westward into the Ohio River Valley as a stationary surface front (not shown).

The location of TC Danny and the synoptic pattern analyzed 12 h earlier (Fig. 4.2a) remained similar at 0600 UTC 23 July (Fig. 4.3a); however, an area of synoptic-scale descent was analyzed over TC Danny at this time (Fig. 4.3b). A 1022-hPa anticyclone was located over southern Quebec, which induced a cold-air damming signature in the MSLP and 1000–500 hPa thickness fields across the lee side of the northern Appalachian Mountains (Fig. 4.3a). An inverted surface trough off the Virginia–North Carolina coast (Fig. 4.3a) indicates the location of the stationary surface front, which extended from the Virginia–North Carolina border toward the northwest Atlantic Ocean (not shown). A near-perpendicular orientation of the thickness contours with respect to the sea level isobars over North Carolina and Virginia (Fig. 4.3a) suggests that weak warm-air advection was developing over that area (Fig. 4.3a).

By 1800 UTC 23 July, TC Danny was located over northern Georgia, indicative of the start of the eastward progression of the storm toward the Carolinas (Fig. 4.4a). The westward extension of the upper-tropospheric jet off the coast of the Canadian Maritimes was now characterized by a developing upper-tropospheric jet streak approximately 500 km poleward of TC Danny (Fig. 4.4a). As indicated by the 700-hPa vertical motion field (Fig. 4.4b), TC Danny was entering into the area of maximum upward vertical motion values (-0.2 Pa s^{-1}) over Virginia and North Carolina. This area of synoptic-scale ascent was likely associated with rising motion in the equatorward entrance region of the upper-

tropospheric jet and warm-air advection over Virginia and North Carolina (Fig. 4.4a). A relative minimum in MSLP over the Ohio River Valley (Fig. 4.4a) developed in response to an amplifying upper-tropospheric trough over the Midwest (not shown). The aforementioned anticyclone shifted southeastward over northern New England during the 12-h period between 0600 UTC 23 July (Fig. 4.3a) and 1800 UTC 23 July (Fig. 4.4a), and had strengthened from 1022 hPa (Fig. 4.3a) to 1024 hPa (Fig. 4.4a). The cold-air damming signature remained in place over the lee side of the northern Appalachian Mountains (Fig. 4.4a), which anchored the stationary surface front over the Virginia–North Carolina border (not shown). The inverted surface trough analyzed off the Virginia–North Carolina coast (Fig. 4.4a) indicated the position of the stationary surface front.

By 0600 UTC 24 July, TC Danny progressed to the South Carolina–North Carolina border and was now juxtaposed with the equatorward entrance region of the upper-tropospheric jet 400 km poleward of the TC (Fig. 4.5a). The upper-tropospheric jet strengthened to 35 m s^{-1} over Long Island (Fig. 4.5a) in the 12 h after 1800 UTC 23 July (Fig. 4.4a). In conjunction with the strengthening upper-tropospheric jet, 700-hPa vertical motion values increased to over -0.35 Pa s^{-1} around the Virginia–North Carolina coast (Fig. 4.5b) in the 12 h after 1800 UTC 23 July (Fig. 4.4b). Continued weak warm-air advection over Virginia and North Carolina was acting to induce ascent northeast of TC Danny (Fig. 4.5a) and contributed to the synoptic-scale ascent analyzed over that area (Fig. 4.5b). The relative MSLP minimum over the Ohio River Valley at 1800 UTC 23 July (Fig. 4.4a) was located over eastern Kentucky at 0600 UTC 24 July (Fig. 4.5a) as the upper-tropospheric trough positioned itself over the northern Ohio River Valley (not

shown). Cold-air damming associated with the anticyclone off the coast of Nova Scotia (Fig. 4.5a), which strengthened to 1026 hPa in the 12 h after 1800 UTC 23 July (Fig. 4.4a), was better defined in the MSLP field than 12 h earlier (Fig. 4.4a). This setup is consistent with a Miller (1946) type B cyclone development, where secondary cyclogenesis occurs along a warm front associated with a primary low-pressure system dissipating west of the Appalachian Mountains. Cold-air damming on the lee side of the Appalachian Mountains is common to these Miller (1946) type B cyclone developments as well.

TC Danny continued to be juxtaposed with the equatorward entrance region of the poleward upper-tropospheric jet at 1800 UTC 24 July as the storm reached northeastern North Carolina (Fig. 4.6a). The wind speed maximum of the upper-tropospheric jet (35 m s^{-1}) became concentrated over southeastern Pennsylvania (Fig. 4.6a) in the 12 h after 0600 UTC 24 July (Fig. 4.5a). Weak warm-air advection continued to be implied beneath the equatorward entrance region of the upper-tropospheric jet (Fig. 4.6a) and corresponded to an area of 700-hPa ascent maximized off the Virginia–North Carolina coast (Fig. 4.6b). The axis of the upstream upper-tropospheric trough was positioned just west of the Appalachian Mountains (not shown). The relative minimum in MSLP over Kentucky was no longer analyzed at 1800 UTC 24 July (Fig. 4.6a) since TC Danny became the primary circulation downstream of the trough axis, consistent with a Miller (1946) type B cyclone development. The 1026-hPa anticyclone northeast of TC Danny continued to shift eastward in the 12 h after 0600 UTC 24 July (Fig. 4.5a), and the associated cold-air damming signature remained in place on the lee side of the northern Appalachian Mountains (Fig. 4.6a). This cold-air damming continued to anchor lower-

tropospheric baroclinicity and its associated stationary surface front (not shown) across the Virginia–North Carolina border, with which TC Danny consolidated at 1800 UTC 24 July (Fig. 4.6a).

4.2.2. Satellite and Radar Observations

4.2.2.1 Satellite Observations

An infrared satellite image at 2345 UTC 22 July indicates disorganized cloud cover associated with TC Danny over Alabama (Fig. 4.7a). An expansive cloud shield observed over the Mid-Atlantic region (Fig. 4.7a) corresponds with the area of synoptic-scale ascent and warm-air advection analyzed in Figs. 4.3b and 4.3a, respectively. During the subsequent 24 h, the cloud shield associated with TC Danny organized and consolidated with the cloud shield centered over the Mid-Atlantic region (Figs. 4.7a–c) as the TC moved closer toward the area of enhanced synoptic-scale ascent and warm-air advection analyzed at 1800 UTC 23 July (Figs. 4.4a,b). By 1145 UTC 24 July, much of the cloud shield observed over the East Coast of the United States was displaced to the north and east of TC Danny (Fig. 4.7d), where synoptic ascent was maximized and warm-air advection was present about 6 h earlier (Figs. 4.5a,b). In addition, a baroclinic leaf cloud structure observed over New England (Fig. 4.7d) implies that warm air was ascending to jet level and expanding the cloud shield poleward of TC Danny.

4.2.2.2 Radar Observations

A national radar composite at 0000 UTC 23 July depicts a disorganized area of rainfall over Alabama associated with TC Danny (Fig. 4.8a). A large area of stratiform

and convective precipitation over Virginia and North Carolina (Fig. 4.8a) was associated with the lower-tropospheric baroclinic zone analyzed across the area 6 h earlier (Fig. 4.2a). The presence of this area of rainfall can be attributed to the warm-air advection and synoptic-scale ascent analyzed across Virginia and North Carolina in Figs. 4.3a and 4.3b, respectively. During the subsequent 24 h (Figs. 4.8a–c), the rainfall associated with TC Danny had become more organized and had shifted toward the eastern flank of the circulation. This shift in rainfall can be attributed to the warm-air advection and synoptic-scale ascent to the northeast of TC Danny analyzed at 1800 UTC 23 July (Figs. 4.4a,b). At 0000 UTC 24 July, base reflectivity values near 50 dBZ on the eastern flank of TC Danny were associated with the development of convection near the TC circulation (Fig. 4.8c). By 1200 UTC 24 July, as TC Danny was undergoing inland reintensification, base reflectivity values greater than 50 dBZ were observed around the inner core of TC Danny (Fig. 4.8d), indicative of deep convection. In addition, the rainfall associated with TC Danny had consolidated with the rainfall over the Mid-Atlantic (Fig. 4.8d), which was supported by synoptic-scale ascent and warm-air advection in the region at 0600 UTC 24 July (Figs. 4.5a,b).

4.2.3. PV Analysis

To analyze the position of an upper-level positive PV anomaly with respect to TC Danny, maps of potential temperature on the 2 PVU surface [identified as the dynamic tropopause (DT)], 850–200-hPa wind shear, and 925–850-hPa layer-averaged relative vorticity are displayed in Figs 4.9a–4.13a. Two large-scale positive PV anomalies are analyzed at 1800 UTC 22 July (Fig. 4.9a). One PV anomaly, located over central Quebec,

was associated with the aforementioned extratropical cyclone over the Labrador Sea (section 4.2.1), whereas the second positive PV anomaly was centered over the northern Great Plains (Fig. 4.9a). This second positive PV anomaly was associated with the upper-tropospheric trough mentioned in section 4.2.1. The location of TC Danny was about 1700 km equatorward of the positive PV anomaly in the northern Great Plains (Fig. 4.9a), likely far enough to avoid a direct interaction between the TC and this upper-tropospheric positive PV anomaly. The shear vectors around TC Danny show that the TC was in a low-shear (2.5 m s^{-1}) environment, and the anticyclonic curvature of the shear vectors (Fig. 4.9a) indicated that a warm-core structure was associated with TC Danny from 850 to 250 hPa (Fig. 4.9b). The relative vorticity field associated with TC Danny shows that the TC was quasi-symmetric as well (Fig. 4.9a). A north–south vertical cross section taken through the center of TC Danny at the same time displays PV, potential temperature, and horizontal wind speed (Fig. 4.9b). The western extension of the zonal upper-tropospheric jet (Fig. 4.2a) was indicated by the 25 m s^{-1} wind speed maximum at 200 hPa (Fig. 4.9b). PV values of 1.5 PVU were oriented near vertically from 850 to 400 hPa, which marked the PV column or tower associated with TC Danny (Fig. 4.9b).

By 0600 UTC 23 July, the positive PV anomaly in the northern Great Plains had moved farther south into northwest Wisconsin (Fig. 4.10a) in the 12 h after 1800 UTC 22 July (Fig. 4.9a), likely still far enough from TC Danny (1500 km) to not influence on the TC (Fig. 4.10a). The magnitude and orientation of the shear vectors and relative vorticity field around TC Danny (Fig. 4.10a) remained the same as 12 h earlier (Fig. 4.9a), consistent with the warm-core structure from 600 to 200 hPa associated with the TC (Fig. 4.10b). The corresponding vertical cross section resolved the upper-tropospheric jet

poleward of TC Danny, which strengthened to 30 m s^{-1} at 200 hPa (Fig. 4.10b) in the 12 h after 0600 UTC 23 July (Fig. 4.9b). The PV column associated with TC Danny remained vertical at this time and PV values had increased to 2 PVU from 650 to 400 hPa (Fig. 4.10b) in the 12 h after 0600 UTC 23 July (Fig. 4.9b).

By 1800 UTC 23 July, the positive PV anomaly poleward of TC Danny started to amplify over Lake Michigan as an upstream negative PV anomaly amplified over the northern Great Plains (Fig. 4.11a) in the 12 h after 0600 UTC 23 July (Fig. 4.10a). The amplifying positive PV anomaly, about 1000 km poleward of TC Danny, likely enabled the TC to accelerate toward the east into northern Georgia by 1800 UTC 23 July (Fig. 4.11a). The anticyclonic curvature of the shear vectors around TC Danny (Fig. 4.11a) remained the same as 12 h earlier (Fig. 4.10a); however, the magnitude of the shear increased to 5 m s^{-1} (Fig. 4.11a). An increase in the magnitude of the 925–850-hPa layer-averaged relative vorticity field (Fig. 4.11a) associated with TC Danny corresponded to an increase of the PV in the same layer (Fig. 4.11b) in the 12 h after 0600 UTC 23 July (Fig. 4.10b). Above this layer, PV values of 2 PVU were maximized at 800 hPa and throughout 700–400 hPa layer (Fig. 4.11b). Associated with the increased PV in the 700–400 hPa layer, a wind speed maximum of 15 m s^{-1} at 600 hPa was located south of the PV column (Fig. 4.11b). The maximum wind speed of 30 m s^{-1} at 200 hPa poleward of TC Danny (Fig. 4.11b) was associated with the aforementioned upper-tropospheric jet analyzed in Fig. 4.4a, and a tropopause fold was analyzed at the location of the upper-tropospheric jet (Fig. 4.11b).

As TC Danny moved from South Carolina into North Carolina at 0600 UTC 24 July, the TC was in the process of inland reintensification. The DT map shows that the

positive PV anomaly northwest of TC Danny continued to amplify (Fig. 4.12a) in the 12 h after 1800 UTC 23 July (Fig. 4.11a) while the negative PV anomaly farther west amplified over the upper Great Plains (Fig. 4.12a). The positive PV anomaly over the eastern Great Lakes was 750 km away from TC Danny at 0600 UTC 24 July (Fig. 4.12a), which implies that an interaction between the TC and the upper-tropospheric jet was occurring. Implied ascent downstream of this positive PV anomaly may have accounted for the increase in synoptic-scale ascent over the Virginia–North Carolina coast from 1800 UTC 23 July to 0600 UTC 24 July (Figs. 4.4b–4.5b). The anticyclonic curvature of the shear vectors around TC Danny (Fig. 4.12a) was indicative of the warm-core structure from 850 to 200 hPa associated with the TC (Fig. 4.12b), and the magnitude of the shear vectors continued to be 5 m s^{-1} (Fig. 4.12a). An increase in the relative vorticity associated with TC Danny was evident (Fig. 4.12a) in the 12 h after 1800 UTC 23 July (Fig. 4.11a). This increase corresponded to an increase in the strength of the PV column associated with the TC (Fig. 4.12b) in the 12 h after 1800 UTC 23 July (Fig. 4.11b). PV values of 2 PVU from 950 to 400 hPa and two 3 PVU maxima analyzed near 850 hPa and just above 700 hPa in the PV column (Fig. 4.12b) highlight the strengthening PV column (Fig. 4.12b) in the 12 h after 1800 UTC 23 July (Fig. 4.11b). This increase in PV was associated with an increase in the vertical extent of 15 m s^{-1} wind speed values from 950 to 500 hPa on the south side of TC Danny (Fig. 4.12b) in the 12 h after 1800 UTC 23 July (Fig. 4.11b). A slight southward tilt of the PV column was analyzed in Fig. 4.12b, which was likely a result of the increased effects from vertical wind shear associated with the upstream positive PV anomaly (Fig. 4.12a). A reduction of PV at 200 hPa above and poleward of the PV column associated with TC Danny (Fig. 4.12b) in the 12 h after 1800

UTC 23 July (Fig. 4.11b) was likely associated with diabatic heating arising from convection near the center of TC Danny observed at 0000 UTC 24 July (Fig. 4.8c). This reduction in PV led to an increase of the cross-jet PV gradient (Fig. 4.12b) in the 12 h after 1800 UTC 23 July (Fig. 4.11b). This increased PV gradient led to a strengthening of the upper-tropospheric jet to 35 m s^{-1} at 200 hPa (Fig. 4.12b) compared to 12 h earlier (Fig. 4.11b).

By 1800 UTC 24 July, TC Danny had regained tropical storm status over northeastern North Carolina. The upstream positive PV anomaly, about 600 km from TC Danny, was located over northwestern Pennsylvania at this time and had amplified further (Fig. 4.13a) in the 12 h after 0600 UTC 24 July (Fig. 4.12a). The downstream position of TC Danny with respect to the positive PV anomaly at 1800 UTC 24 July (Fig. 4.13a) continued to place the TC in a favorable location for ascent (Fig. 4.6b). Although the shear vector pattern around TC Danny indicated the shear magnitude had increased to $7.5\text{--}10 \text{ m s}^{-1}$ by 1800 UTC 24 July (Fig. 4.13a) in the 12 h after 0600 UTC 24 July (Fig. 4.12a), the tilt of the PV column associated with the TC became more vertical and the warm-core structure associated with TC Danny from 850 to 200 hPa was maintained (Fig. 4.13b). Diabatically driven PV increases below 500 hPa (Fig. 4.12b–4.13b) likely negated the influence from increased vertical shear near the TC (Fig. 4.13a) in the 12 h after 0600 UTC 24 July (Fig. 4.12a) and allowed the TC-related PV column to remain upright (Fig. 4.13b). A further reduction of the PV above and poleward of TC Danny in the 12 h after 0600 UTC 24 July (Fig. 4.12b) was likely associated with diabatic heating arising from the increased convection observed around TC Danny at 1200 UTC 24 July (Fig. 4.8d) in the 12 h after 0000 UTC 24 July (Fig. 4.8c). The relative vorticity increase

around TC Danny (Fig. 4.13a) in the 12 h after 0600 UTC 24 July (Fig. 4.12a) corresponded to an increase of the PV at 850 hPa to 4 PVU (Fig. 4.13b). An area of 15 m s⁻¹ wind speed values extended down to the surface on the south side of TC Danny at this time (Fig. 4.13b). Maximum wind speed values of 25 m s⁻¹ were located on the south side of TC Danny from 850 hPa to 600 hPa (Fig. 4.13b). Although the upper-tropospheric jet was identified by a 25 m s⁻¹ wind speed maximum at 250 hPa in the cross section (Fig. 4.13b), the wind speed maximum in the upper-tropospheric jet was 35 m s⁻¹ east of the cross section location at 1800 UTC 24 July (Fig. 4.6a).

4.2.4. Low-Level Structure and Moisture Evolution

The low-level structure and moisture evolution of TC Danny was analyzed using maps of precipitable water (PW), 925-hPa geopotential height, 925-hPa wind, 925-hPa potential temperature, and 700-hPa upward vertical motion (Figs. 4.14–4.20). At 1800 UTC 22 July, the location of TC Danny was approximated by a closed 81-dam contour at 925 hPa in northern Alabama (Fig. 4.14). TC Danny was embedded in a highly moist environment (PW > 50 mm) at this time, as was much of the southeastern United States (Fig. 4.14). Values of PW in excess of 50 mm around Florida were likely associated with the northward transport of moisture west of a subtropical anticyclone located over the western Atlantic (Fig. 4.14). A west–east strip of PW values in excess of 50 mm, which extended over the western Atlantic from the Virginia–North Carolina border (Fig. 4.14), was located at the southern edge of a lower-tropospheric baroclinic zone at 925 hPa. This baroclinic zone was associated with the lower-tropospheric baroclinic zone analyzed in Fig. 4.2a. The high values of PW extending over the western Atlantic from the Virginia–

North Carolina border correlate well with the area of stratiform and convective precipitation observed over that area 6 h later (Fig. 4.8a).

Although a closed circulation associated with TC Danny at 925 hPa was not apparent at 0600 UTC 23 July, cyclonic curvature in the 925-hPa wind flow over northeast Alabama denotes the location of TC Danny (Fig. 4.15). PW values greater than 50 mm were analyzed in and around TC Danny at this time, while a plume of moisture ($PW > 50$ mm) extended from Florida toward the 925-hPa baroclinic zone over southern Virginia (Fig. 4.15). The moist conditions analyzed around TC Danny were consistent with the 60 mm values of PW observed in the 1200 UTC 23 July sounding from Atlanta, Georgia (KFFC), taken 6 h later (Fig. 4.16). In addition, low-to-moderate CAPE values (770 J kg^{-1}) and directional shear observed in the KFFC sounding (Fig. 4.16) supported the formation of convection near the TC center (Fig. 4.8b). In Fig. 4.15, broad upward vertical motion was predominately analyzed along the southern edge of the lower-tropospheric baroclinic zone that stretched eastward into the western Atlantic along a confluence zone. This analyzed region of 700-hPa vertical motion correlates well with the area of stratiform and convective precipitation observed 6 h earlier (Fig. 4.8a).

By 1800 UTC 23 July, a closed circulation at 925 hPa was discernible around TC Danny (Fig. 4.17). Values of PW greater than 50 mm continued to be analyzed in and around TC Danny and along the lower-tropospheric baroclinic zone northeast of the TC (Fig. 4.17). A sounding from Greensboro, North Carolina (KGSO), at 0000 UTC 24 July depicts a moist and unstable environment ahead of TC Danny (Fig. 4.18). The KGSO sounding indicates a PW value of 57 mm and CAPE of 1145 J kg^{-1} (Fig. 4.18). In addition, a veering wind profile from the surface to 400 hPa (Fig. 4.18) indicates the

presence of warm-air advection in that layer (Fig 4.4a). This sounding exhibits the favorable conditions for the formation of convection along the inner core of TC Danny 12 h later at 1200 UTC 24 July (Fig. 4.8d).

At 0600 UTC 24 July, a 78-dam closed circulation associated with TC Danny at 925 hPa was located along the South Carolina–North Carolina border (Fig. 4.19). A 3-dam 925-hPa geopotential height decrease (Fig. 4.19) in the 12 h after 1800 UTC 23 July (Fig. 4.18) indicated TC Danny was in the process of reintensification. Analyzed PW values exceeded 60 mm at the center and eastern flank of TC Danny (Fig. 4.19). In addition, vigorous upward motion at 700 hPa ($-20 \times 10^{-3} \text{ hPa s}^{-1}$) helped to develop convection around TC Danny (Figs. 4.8c–d).

By 1800 UTC 24 July, TC Danny approached northeast North Carolina and was characterized by a 78-dam closed circulation at 925 hPa (Fig. 4.20). At 1800 UTC 24 July, the TC started to merge with the lower-tropospheric baroclinic zone (Fig. 4.20), which was anchored along the Virginia–North Carolina border due to the cold-air damming east of the Appalachian Mountains (Fig. 4.20). PW values exceeding 60 mm and 700-hPa upward vertical motion greater than $-20 \times 10^{-3} \text{ hPa s}^{-1}$ continued to be analyzed around TC Danny (Fig. 4.20), and supported the moist convection observed around the TC circulation 6 h earlier (Fig. 4.8d).

4.3. Mesoscale Overview

4.3.1. *Precipitation Evolution*

The purpose of this section will be to discuss the evolution of the rainfall associated with TC Danny prior to and during its inland reintensification during the 42-h

period from 0000 UTC 23 July through 1800 UTC 24 July (Figs 4.21–4.25). A 0.5° base reflectivity image from Birmingham, Alabama (KBMX), at 0013 UTC 22 July displays a “pinwheel” appearance in the rainfall associated with TC Danny (Fig. 4.21a). A GOES-8 visible satellite image one hour earlier shows overshooting cloud tops associated with convection on the eastern and southern quadrants of the TC circulation (Fig. 4.21b). The visible satellite image also shows that TC Danny had the appearance of a midlevel circulation (e.g., mesoscale convective vortex) at 2315 UTC 24 July (Fig. 4.21b).

At 1218 UTC 23 July, a consolidated area of rainfall near the center of TC Danny was evident in a 0.5° base reflectivity image from Atlanta, Georgia (KFFC) (Fig. 4.22a). A large area of stratiform precipitation with embedded convection was located on the northern and eastern sides of the TC center (Fig. 4.22a), consistent with warm-air advection and 700-hPa ascent to the northeast of TC Danny analyzed 6 h later (Figs. 4.4a,b). A dense overcast associated with the organized rainfall was observed in a visible satellite image at about the same time (Fig. 4.22b).

The structure of the rainfall in and around the central circulation of TC Danny at 0015 UTC 24 July (Fig. 4.23a) remained similar to that 12 h earlier (Fig. 4.22a). At this time, most of the rainfall was once again on the northern and eastern sides of the circulation as observed by the Greer, South Carolina (KGSP), radar (Fig. 4.23a). Deep convection was evident on the northeastern side of TC Danny’s inner core at 0015 UTC 24 July (Fig. 4.23a), which is consistent with warm-air advection and 700-hPa ascent to the northeast of TC Danny 6 h later (Figs. 4.5a,b). A corresponding visible image taken one hour earlier displays an overshooting top observed on the northeast side of TC Danny’s inner core (Fig. 4.23b). Other areas of overshooting tops, representative of

additional areas of convection, can be seen further to the east of TC Danny's central circulation (Fig. 4.23b).

A 0.5° base reflectivity image taken from Wakefield, Virginia (KAKQ), at 1318 UTC 24 July (Fig. 4.24a) displays convection on the northern inner core of an eye-like feature that developed (Fig. 4.24a) in about the 13 h after 0015 UTC 24 July (Fig. 4.23a). As will be shown in section 4.3.2, the development of convection near the inner core of TC Danny was important to its inland reintensification. A corresponding visible image at 1315 UTC 24 July shows a well-defined central dense overcast associated with the central circulation of TC Danny (Fig. 4.24b). Cyclonically curved low-level clouds to the west of the central dense overcast suggest that the western side of TC Danny was uncovered by westerly shear (Fig. 4.24b). The $7.5\text{--}10\text{ m s}^{-1}$ vertical wind shear analyzed over TC Danny about 5 h later in Fig. 4.13a is consistent with the implied westerly shear observed in Fig. 4.24b.

A base reflectivity image taken from KAKQ at 1814 UTC 24 July displayed the eye-like feature associated with TC Danny (Fig. 4.25a). The precipitation distribution around TC Danny showed that rainfall was predominately north-northeast of the TC center (Fig. 4.25a), which is expected since the synoptic setup is similar to a LOC precipitation distribution (Atallah et al. 2007). The presence of a positively tilted upper-tropospheric trough approaching a TC from the northwest was the main similarity in the synoptic setup between the TC Danny case and a LOC precipitation distribution (Atallah et al. 2007). The precipitation distribution is also consistent with the analyzed 700-hPa ascent and warm-air advection maximized to the northeast of the TC (Figs. 4.6a,b). A

corresponding visible image taken at 1815 UTC 24 July continued to display the central dense overcast associated with the circulation of TC Danny (Fig. 4.25b).

4.3.2. Diabatic Heating Analysis

The role of diabatic heating in the TC Danny reintensification case will be documented in this section. As mentioned in section 4.3.1, the development of rainfall and deep moist convection was observed near the central circulation of TC Danny as the storm passed over northern Georgia and the Carolinas during 23–24 July. Increased convection around TC Danny during this time period was important in the production of cyclonic relative vorticity and PV near the surface (Figs. 4.10a,b–4.13a,b), and this argument will be supported by analyzing forecast vertical heating profiles prior to and during the inland reintensification of TC Danny in the 36-h period from 0000 UTC 23 July through 1200 UTC 24 July.

Idealized vertical latent heating profiles for different modes of precipitation were presented in Schumacher et al. (2004), and the vertical latent heating profile for convective precipitation was characterized by heating at all levels, with maximum heating at midlevels. Values of diabatic heating were obtained from CFSR 6-h forecasts of diabatic heating at 28 vertical levels from 1000 to 100 hPa and averaged in a $3^\circ \times 3^\circ$ box around the central circulation of TC Danny. The plotted diabatic heating profiles show that heating increased at most levels with time, with maximum heating around 500 hPa (Fig. 4.26). This midlevel warming was likely associated with diabatic heating resulting from deep convection that developed in the approximate 37-h period from 0013 UTC 23 July through 1318 UTC 24 July (Figs. 4.21a–4.24a). These forecast diabatic

heating vertical profiles imply an increase in cyclonic relative vorticity and PV below the level of maximum heating, which was analyzed in Figs. 4.10a,b–4.13a,b.

The effect of a diabatically driven outflow produced from convection associated with TC Danny on the upper-level flow can be assessed using maps of 250-hPa wind speed, 250-hPa PV, 250-hPa relative humidity, 600–400-hPa layer-averaged vertical motion, and 300–200-hPa layered-averaged irrotational winds in a 24-h period from 1800 UTC 23 July through 1800 UTC 24 July (Figs. 4.27–4.29). At 1800 UTC 23 July, the newly developed upper-tropospheric jet and upstream positive PV anomalies were analyzed poleward of the TC (Fig. 4.27). A small area of upward vertical motion on the eastern flank of TC Danny (Fig. 4.27) was associated with the stratiform and convective precipitation observed near the TC circulation about 6 h earlier at 1218 UTC 23 July (Fig. 4.22).

By 0600 UTC 24 July, diabatically driven outflow induced by the convection associated with TC Danny started to impinge on the upper-tropospheric jet poleward of TC Danny (Fig. 4.28). An amplification of the upstream positive PV anomaly over the Great Lakes (Fig. 4.28) in the 12 h after 1800 UTC (Fig. 4.27) put TC Danny in a favorable location for synoptic-scale ascent (Fig. 4.5b). The idea that ascent was favored over TC Danny is also supported by the large values of upward vertical motion averaged from 400 to 600 hPa on the eastern flank of the TC (Fig. 4.28). These values of upward vertical motion were associated with the observed convection seen to the east of TC Danny about 6 h earlier at 0015 UTC 24 July (Fig. 4.23).

At 1800 UTC 24 July, irrotational wind vectors extended from TC Danny toward the poleward upper-tropospheric jet and positive PV anomaly (Fig. 4.29), a pattern

indicative of the diabatically driven outflow induced by the convection associated with TC Danny. Negative PV advection by the irrotational wind, indicated by irrotational wind vectors pointing from lower values toward higher values of PV, acted to strengthen the PV gradient and associated upper-tropospheric jet (Fig. 4.29) in the 12 h after 0600 UTC 24 July (Fig. 4.28). A further amplification of the upper-tropospheric positive PV anomaly 12 h after 0600 UTC 24 July (Fig. 4.28) was the result of ridge building downstream of this feature (Fig. 4.13a). Diabatically induced ridge building analyzed in Fig. 4.13a over New England corresponded with a negative advection of PV by the irrotational wind over that region (Fig. 4.29). An amplification of an upper-tropospheric jet maximum over northern New England (Fig. 4.29) in the 12 h after 0600 UTC 24 July (Fig. 4.28) was a result of this negative PV advection that served to increase the cross-jet PV gradient in that area.

4.3.3. Surface Analysis

The surface environment in and around TC Danny prior to and during its inland reintensification will be presented using surface analyses of MSLP, wind, temperature, and dewpoint in the 24-h period from 1200 UTC 23 July through 1200 UTC 24 July (Figs. 4.30–4.32). At 1200 UTC 23 July, a closed 1012-hPa MSLP contour over northwest Georgia denotes the location of TC Danny and shows that the TC was a relatively small-scale circulation feature (Fig. 4.30). Surface dewpoint values of 23°C in northwestern Georgia indicate that a moist surface environment within which the TC was embedded supported the development of convection (Fig. 4.22a). Dewpoint depression values of 0–1°C in northern Georgia (Fig. 4.30) correspond to the area where rain was

falling 1218 UTC 23 July (Fig. 4.22a). The stationary surface front discussed in section 4.2.1 was identified in Fig. 4.30 by cyclonically curved wind flow and an inverted trough feature located near the Virginia–North Carolina border.

At 0000 UTC 24 July, the location of TC Danny was identified by the position of the 1012-hPa MSLP contour over northwestern South Carolina (Fig. 4.31). The moist surface environment was still in place in and around TC Danny, as indicated by observed dewpoint values from 22 to 24°C (Fig. 4.31). These high dewpoint values indicate the continued favorable conditions for convective development, which was observed in the approximate 12-h period from 1218 UTC 23 July to 0015 UTC 24 July (Figs. 4.22–4.23). Differential surface heating was evident at 0000 UTC 24 July, where a $3^{\circ}\text{C} (100 \text{ km})^{-1}$ baroclinic zone was analyzed south of TC Danny (Fig. 4.31), an area where cloud cover was minimal about one hour earlier (Fig. 4.23b). Dense cloud cover and rainfall observed in Figs. 4.23a,b was responsible for lower observed temperatures, relative to the environment, around the South Carolina–North Carolina border at 0000 UTC 24 July (Fig. 4.31). The stationary surface front identified in Fig. 4.30 is not readily identified in Fig. 4.31 along the Virginia–North Carolina border at 0000 UTC 24 July.

By 1200 UTC 24 July, a closed 1008-hPa MSLP contour around the center of TC Danny was analyzed over east-central North Carolina (Fig. 4.32), indicating that the TC had deepened approximately 4 hPa in the last 12 h. The MSLP field shows that TC Danny continued to be a small and compact system (Fig. 4.32). Dewpoint values of 22–24°C continued to be observed in and around TC Danny, which provided support for the convection around the inner core of the reintensifying TC (Fig. 4.24a). The cold-air damming signature analyzed 6 h earlier in Figs. 4.5a was analyzed in Fig. 4.32, as

indicated by a southwestward bulge of high pressure on the lee side of the Appalachian Mountains and north-northeasterly winds observed over Virginia (Fig. 4.32). As previously mentioned, cold-air damming anchored the stationary surface front over the Virginia–North Carolina border, which was identified by the inverted surface trough stemming from the central circulation of TC Danny (Fig. 4.32). A surface baroclinic zone associated with the stationary surface front served as an additional source for ascent around TC Danny and this feature will be discussed further in the next section.

4.3.4. Frontogenesis and Ageostrophic Circulation Analysis

Vertical cross sections taken through the center of TC Danny prior to and during inland reintensification (1800 UTC 23 July–1800 UTC 24 July) depict Petterssen frontogenesis, potential temperature, horizontal wind speed, and the ageostrophic wind component tangential to the cross section (Figs. 4.33–4.35). At 1800 UTC 23 July, 6 h before TC Danny started its inland reintensification, the newly developed upper-tropospheric jet poleward of TC Danny (Fig. 4.4a) and the TC itself were separate entities, as indicated by a lack of upper-tropospheric diverging ageostrophic winds above TC Danny at this time (Fig. 4.33). The upper-tropospheric jet had a maximum wind speed of 30 m s^{-1} at 200 hPa (Fig. 4.33). Shallow, upward vertical motion that was maximized at 850 hPa on the north side of TC Danny was a result of lower-tropospheric frontogenesis (Fig. 4.33). The lower-tropospheric frontogenesis is inferred to have been produced from differential surface heating as a result of reduced cloud cover to the north of TC Danny observed about 6 h earlier at 1215 UTC 23 July (Fig. 4.22b).

By 0600 UTC 24 July, interaction between the upper-tropospheric jet, which strengthened to 35 m s^{-1} at 200 hPa (Fig. 4.34) in the 12 h after 1800 UTC 23 July (Fig. 4.33), and TC Danny had become more apparent, where diverging ageostrophic winds above the TC were present in the equatorward jet-entrance region (Fig. 4.34). Analyzed diverging ageostrophic winds at upper levels above TC Danny imply ascent below this level, which is confirmed by the tropospheric-deep ascent analyzed over the TC at 0600 UTC 24 July (Fig. 4.34). Compared to Fig. 4.33, values of upward vertical motion had increased over the central circulation of TC Danny (Fig. 4.34). This increase in upward vertical motion appears to be associated with frontogenesis that was maximized at 700 hPa (Fig. 4.34) and deep moist convection observed about 6 h earlier at 0015 UTC 24 July (Fig. 4.23a). In addition, the position of TC Danny underneath the equatorward entrance region of the upper-tropospheric jet (Fig. 4.5a) put the TC in a favorable location for synoptic-scale ascent (Fig. 4.5b).

By 1800 UTC 24 July, increased divergence of ageostrophic winds above TC Danny (Fig. 4.35) compared to 12 h earlier (Fig. 4.34) indicates a strengthening of the interaction between the upper-tropospheric jet and TC Danny. These diverging ageostrophic winds at upper levels are consistent with tropospheric-deep ascent over the TC (Fig. 4.35). In addition to synoptic-scale ascent beneath the equatorward entrance region of the upper-tropospheric jet (Figs. 4.6a,b), frontogenesis that was maximized in the lower-troposphere and at 500 hPa (Fig. 4.35) forced additional ascent around TC Danny and supported deep moist convection at about the same time (Fig. 4.25a). The lower-tropospheric frontogenesis maximum was likely associated with differential

surface heating as result of reduced cloud cover to the south of TC Danny observed about the same time at 1815 UTC 24 July (Figs. 4.25b).

4.4. Summary

After making a second landfall in southern Alabama as a category 1 hurricane early on 19 July, TC Danny subsequently stalled over Mobile Bay, leading to copious amounts of rainfall in the area. Two days later, TC Danny was downgraded to a tropical depression and started its northward movement into northern Alabama. By 0000 UTC 23 July, TC Danny became influenced by the poleward midlatitude flow and accelerated eastward into northern Georgia. TC Danny would continue to accelerate as it made its way into South Carolina at 0000 UTC 24 July, and the TC subsequently began its inland reintensification and tracked towards the northeast. By 1800 UTC 24 July, TC Danny had traveled into northeastern North Carolina and was renamed a tropical storm. The inland reintensification of TC Danny had the second largest decrease in minimum central MSLP and second largest increase in maximum sustained wind speed when compared to nine other TCs that underwent the same process while inland (Table II).

An analysis of the inland reintensification of TC Danny over the Carolinas shows that the redevelopment of the TC can be attributed to several factors. First, tropospheric-deep ascent beneath an equatorward entrance region of a 35 m s^{-1} upper-tropospheric jet (Figs. 4.6a,b) supported deep moist convection associated with TC Danny. Second, a highly moist environment within which TC Danny was embedded provided sufficient instability to support deep moist convection during its inland reintensification (Figs. 4.19). Third, diabatic heating arising from deep moist convection (Fig. 4.26) that

reinforced ascent near the storm center and increased lower-tropospheric PV also contributed to the inland reintensification of TC Danny. Fourth, negative PV advection by diabatically driven upper-tropospheric outflow associated with TC Danny's deep moist convection acted to strengthen a downstream cross-jet PV gradient and the associated upper-tropospheric jet (Fig. 4.29). Fifth, the position of an upstream positive PV anomaly less than 1000 km from the location of TC Danny (Figs. 4.11a–4.13a) placed the TC in a favorable location for tropospheric-deep ascent and supported the development and maintenance of deep moist convection. This setup is consistent with a “favorable distant interaction” (Hanley et al. 2001), where a positive PV anomaly is between 1000 km and 400 km from a TC center and enables the TC to intensify. Sixth, in addition to the ascent beneath the equatorward entrance region of the upper-tropospheric jet (Fig. 4.6a,b), frontogenesis along a lower-tropospheric baroclinic zone associated with a stationary surface front provided additional ascent around TC Danny in its later stage of inland reintensification (Fig. 4.35).

Table I: The 27 TC candidate cases during 1950–2010.

TC Name (Year)	TC Name (Year)
Diane (1955)	Fran (1996)
Cindy (1959)	Josephine (1996)
Brenda (1960)	Danny (1997)
TS #6 (1961)	Earl (1998)
Cleo (1964)	Dennis (1999)
Alma (1970)	Helene (2000)
Doria (1971)	Allison (2001)
Agnes (1972)	Gaston (2004)
Babe (1977)	Ivan (2004)
David (1979)	Arlene (2005)
Diana (1984)	Cindy (2005)
Charlie (1986)	Alberto (2006)
Chris (1988)	Erin (2007)
Allison (1995)	

Table II: The 10 inland reintensifying TCs during 1950–2010. The second column identifies the state(s) over which each reintensification event took place. The third column identifies whether each respective TC was beneath the equatorward entrance region of an upper-tropospheric jet. The fourth and fifth columns document the observed increase in maximum sustained wind speed and decrease in central minimum MSLP, respectively, at the end of each TC’s inland reintensification period.

TC Name (Year)	Location of Reintensification Event	TC in Equatorward Jet-Entrance Region	Increase in Wind Speed (kt)	Decrease in Pressure (hPa)
Cindy (1959)	NC/VA	Yes	10	6
Cleo (1964)	NC	Yes	10	7
Agnes (1972)	SC/NC	Yes	15	4
David (1979)	PA/NY/VT/NH/ME	Yes	5	10
Diana (1984)	NC	No*	10	5
Danny (1997)	SC/NC	Yes	20	12
Helene (2000)	SC/NC	Yes	15	4
Allison (2001)	LA/MS	Yes	10	5
Gaston (2004)	NC/VA	Yes	5	1
Erin (2007)	OK	No	30	13

* TC was located equatorward of an upper-tropospheric jet, but was not underneath the equatorward jet-entrance region

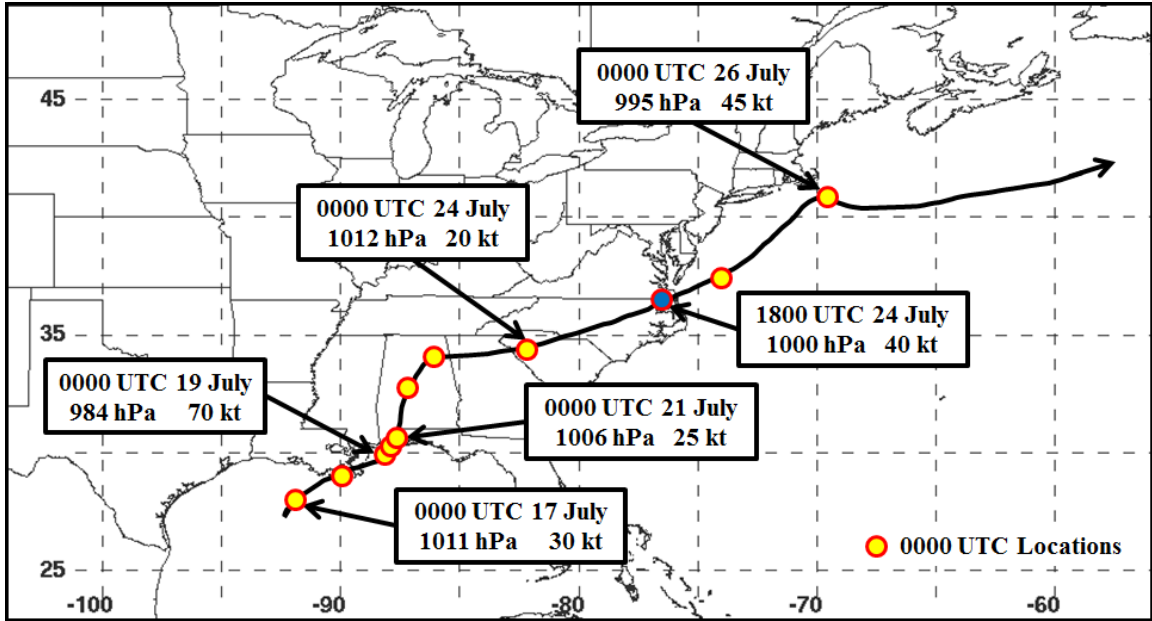


Fig. 4.1. TC Danny track map displaying maximum sustained wind speed and minimum central MSLP observations at 0000 UTC for 17–27 July 1997. 0000 UTC locations are denoted by yellow circles with a red outline. 1800 UTC 24 July locations is denoted by a blue circle with a red outline.

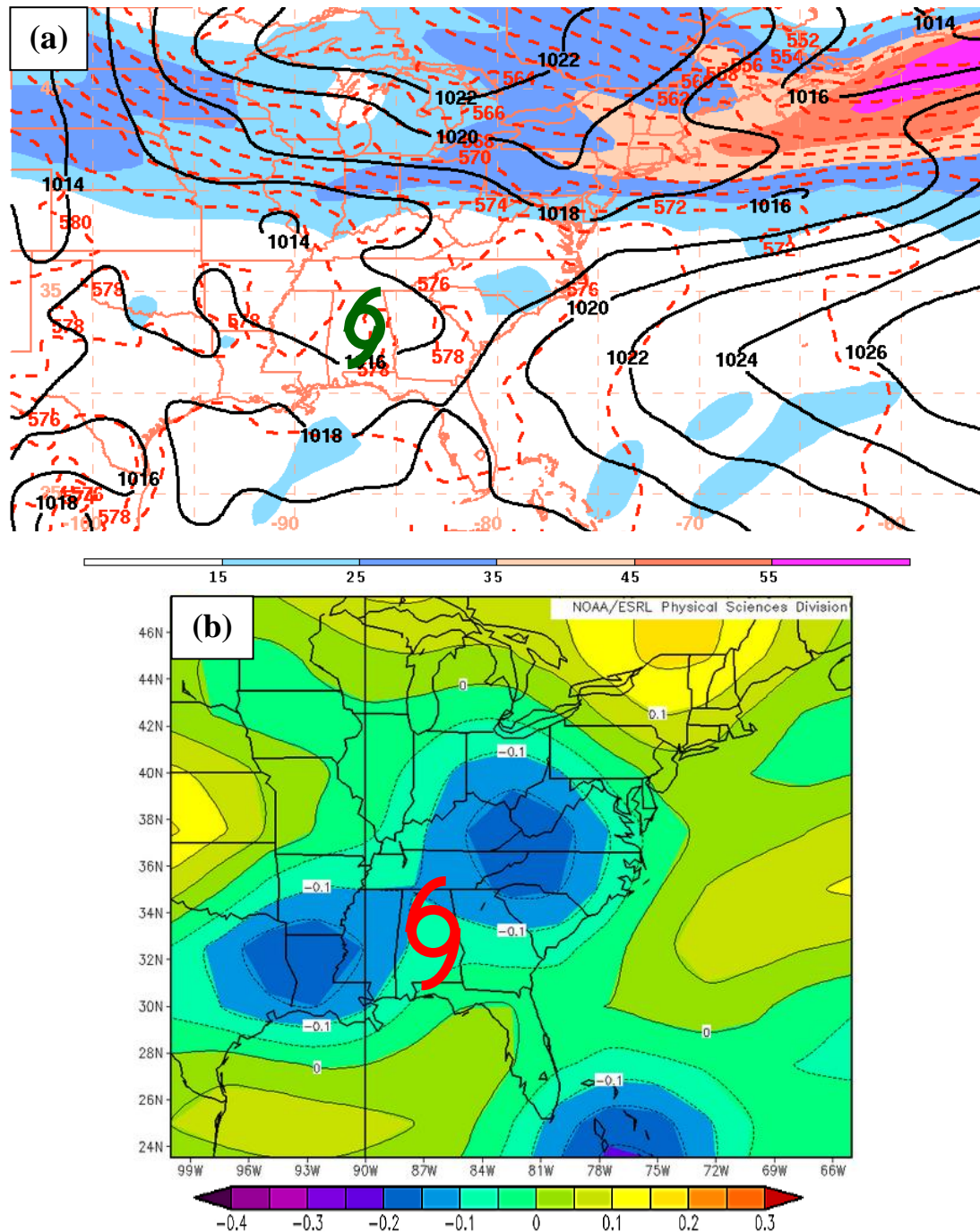


Fig. 4.2. (a) Map of 250-hPa wind speed (shaded, m s^{-1}), 1000–500-hPa thickness (dashed red every 2 dam), and MSLP (solid black every 2 hPa) at 1800 UTC 22 July 1997. The green TC symbol denotes the location of TC Danny as depicted by the CFSR. (b) Map of 700-hPa vertical motion (shaded, Pa s^{-1}) at 1800 UTC 22 July 1997. The red TC symbol denotes the approximate location of TC Danny [Image produced using the ESRL (Earth System Research Laboratory) 6-h NCEP–NCAR Reanalysis Data Composite page available at <http://www.esrl.noaa.gov/psd/data/composites/hour/>.]

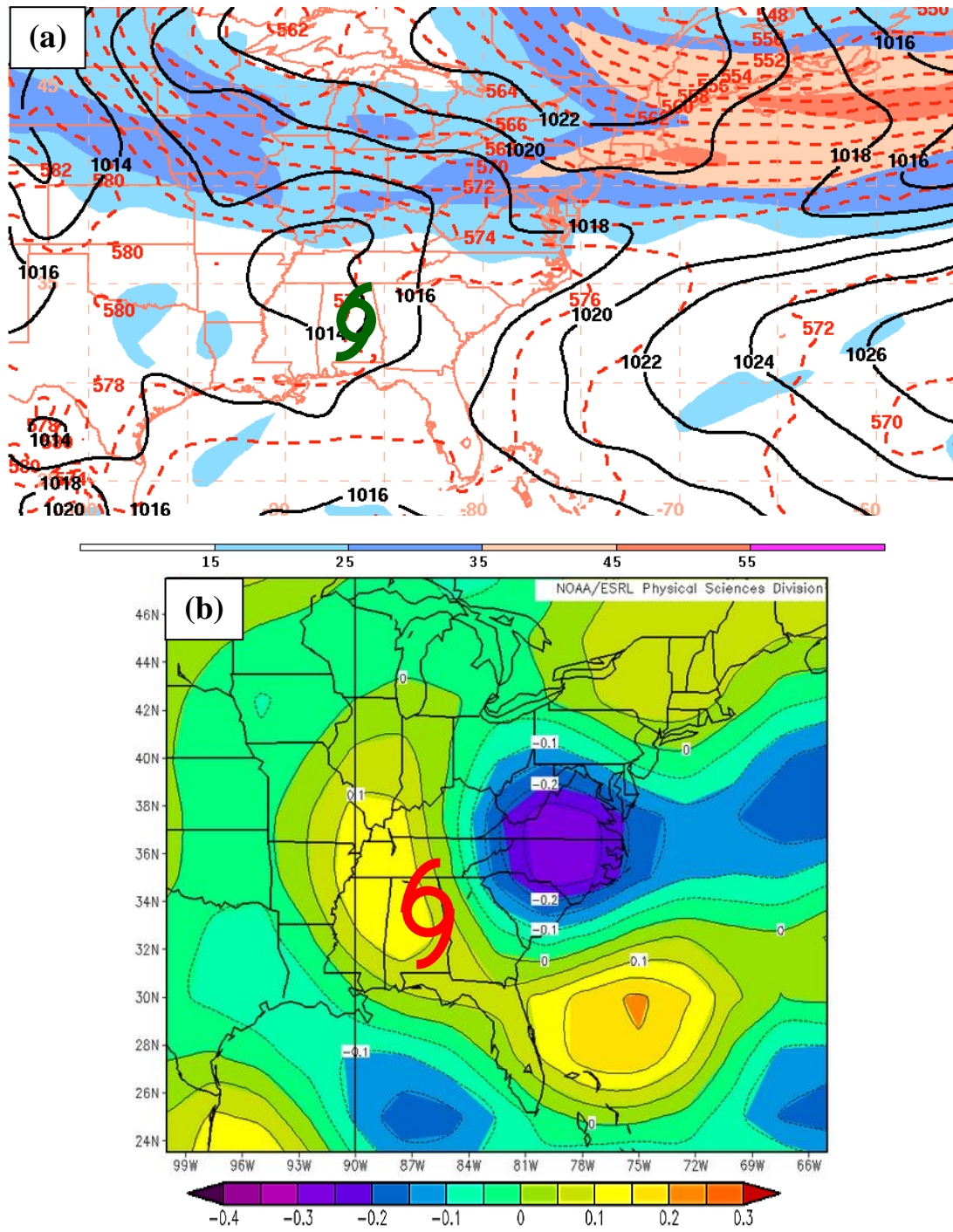


Fig. 4.3. Same as Fig. 4.2, except at 0600 UTC 23 July 1997.

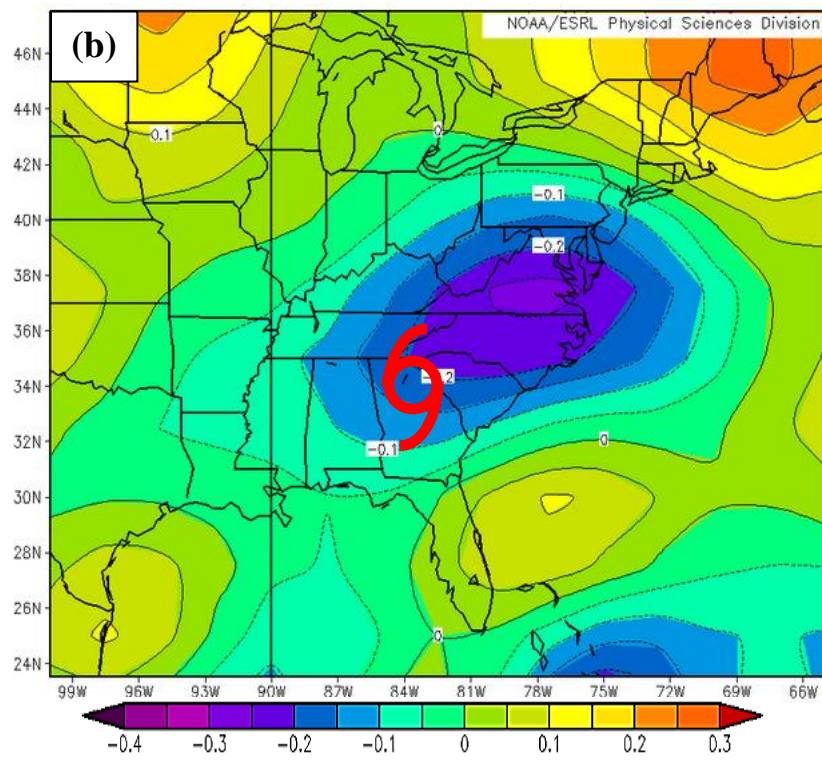
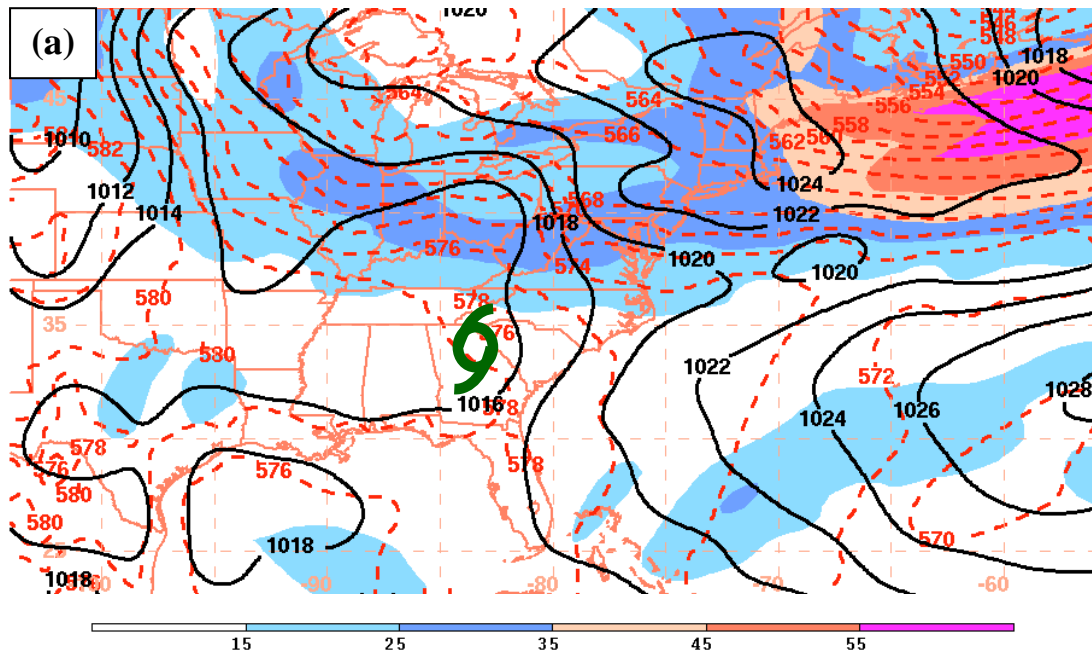


Fig. 4.4. Same as Fig. 4.2, except at 1800 UTC 23 July 1997.

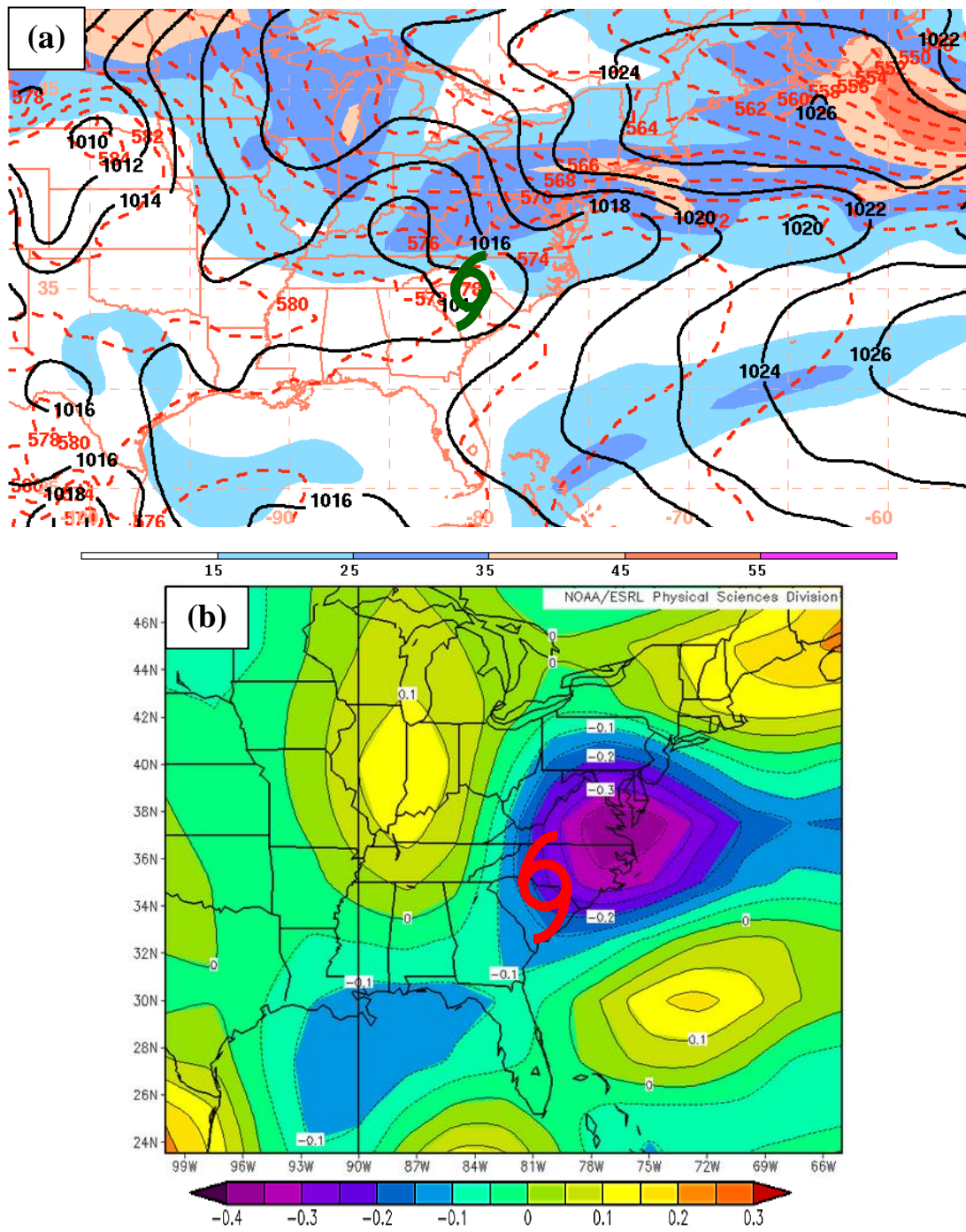


Fig. 4.5. Same as Fig. 4.2, except at 0600 UTC 24 July 1997.

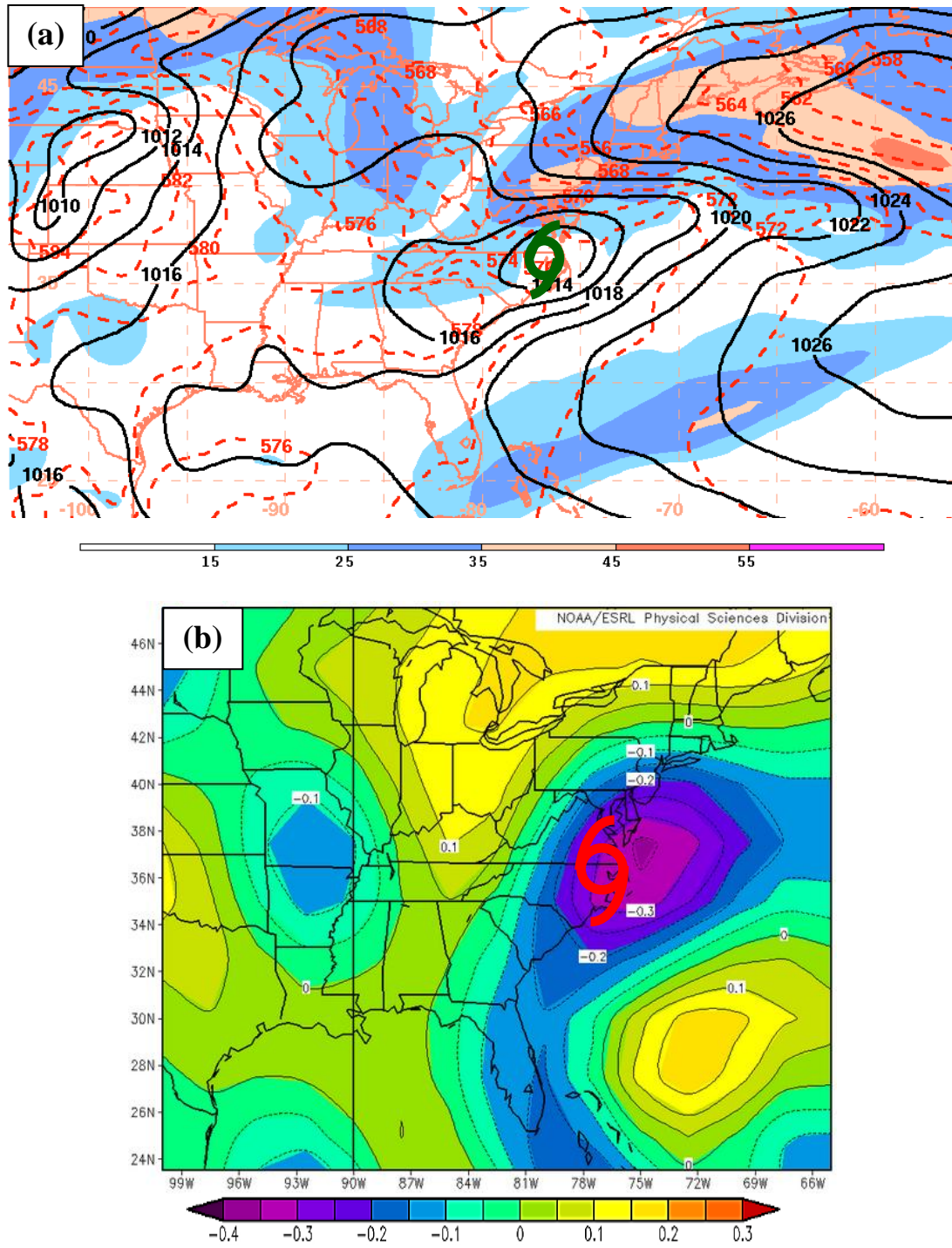


Fig. 4.6. Same as Fig. 4.2, except at 1800 UTC 24 July 1997.

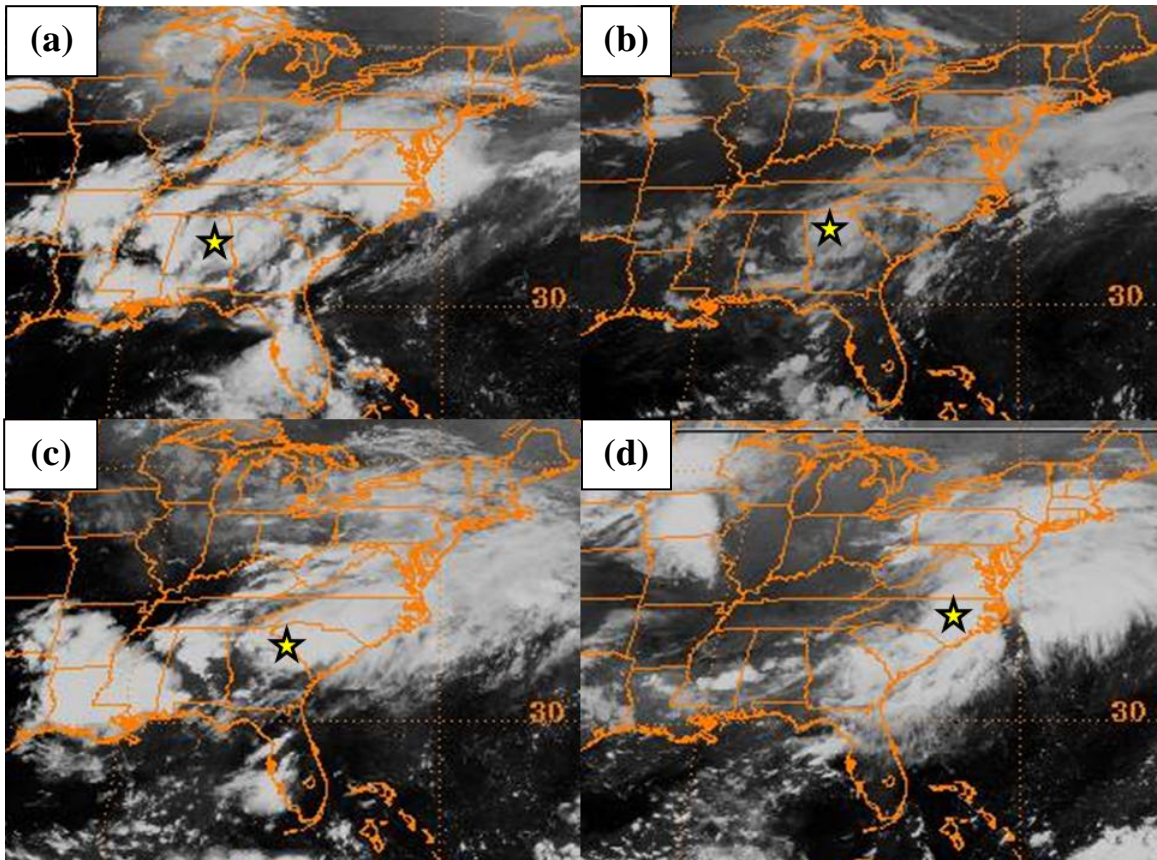


Fig. 4.7. GOES-8 infrared satellite images taken at (a) 2345 UTC 22 July 1997, (b) 1145 UTC 23 July 1997, (c) 2345 UTC 23 July 1997, and (d) 1145 UTC 24 July 1997. The yellow star denotes the approximate location of TC Danny. [Images courtesy of the NCDC GIBBS (Global ISCCP B1 Browse System) page available at [http://www.ncdc.noaa.gov/gibbs/.](http://www.ncdc.noaa.gov/gibbs/)]

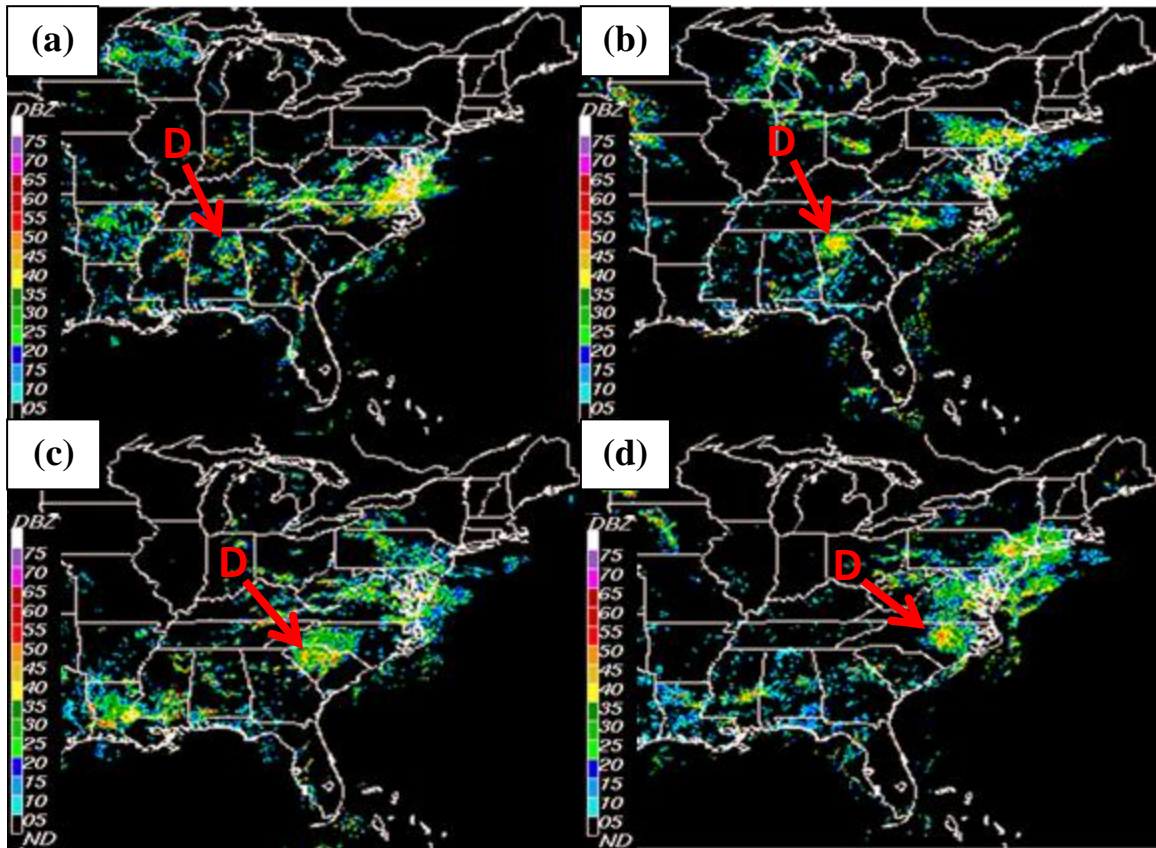


Fig. 4.8. National radar summary composites (shaded every 5 dBZ) at (a) 0000 UTC 23 July 1997, (b) 1200 UTC 23 July 1997, (c) 0000 UTC 24 July 1997, and (d) 1200 UTC 24 July 1997. The “D” symbol denotes the rainfall region associated with TC Danny. [Images available at [http://www.mmm.ucar.edu/imagearchive/.](http://www.mmm.ucar.edu/imagearchive/)]

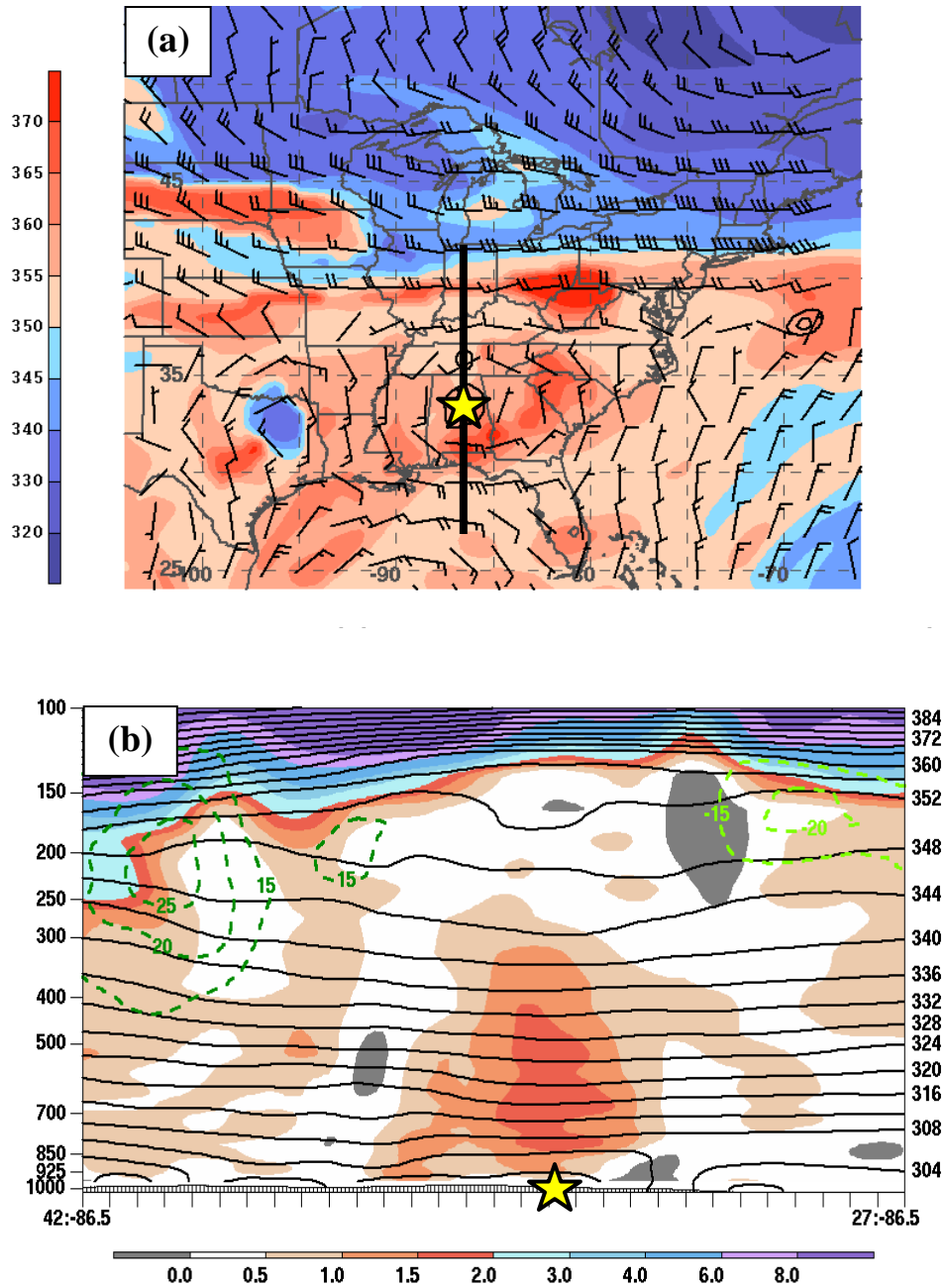


Fig. 4.9. (a) Map of potential temperature on the 2 PVU surface (shaded every 5 K), 850–200-hPa wind shear (barbs, kt), and 925–850-hPa layer-averaged relative vorticity (solid black every $1 \times 10^{-4} \text{ s}^{-1}$ starting at $1 \times 10^{-4} \text{ s}^{-1}$) at 1800 UTC 22 July 1997. The yellow star denotes the position of TC Danny as depicted by the CFSR. The black line denotes the location of the vertical cross section shown in Fig. 3.9b. (b) North–south vertical cross section of PV (shaded every 1 PVU), potential temperature (solid black every 4 K), and horizontal wind speed (dashed green every 5 m s^{-1} starting at 15 m s^{-1}) at 1800 UTC 22 July 1997. The yellow star denotes the location of TC Danny along the cross section.

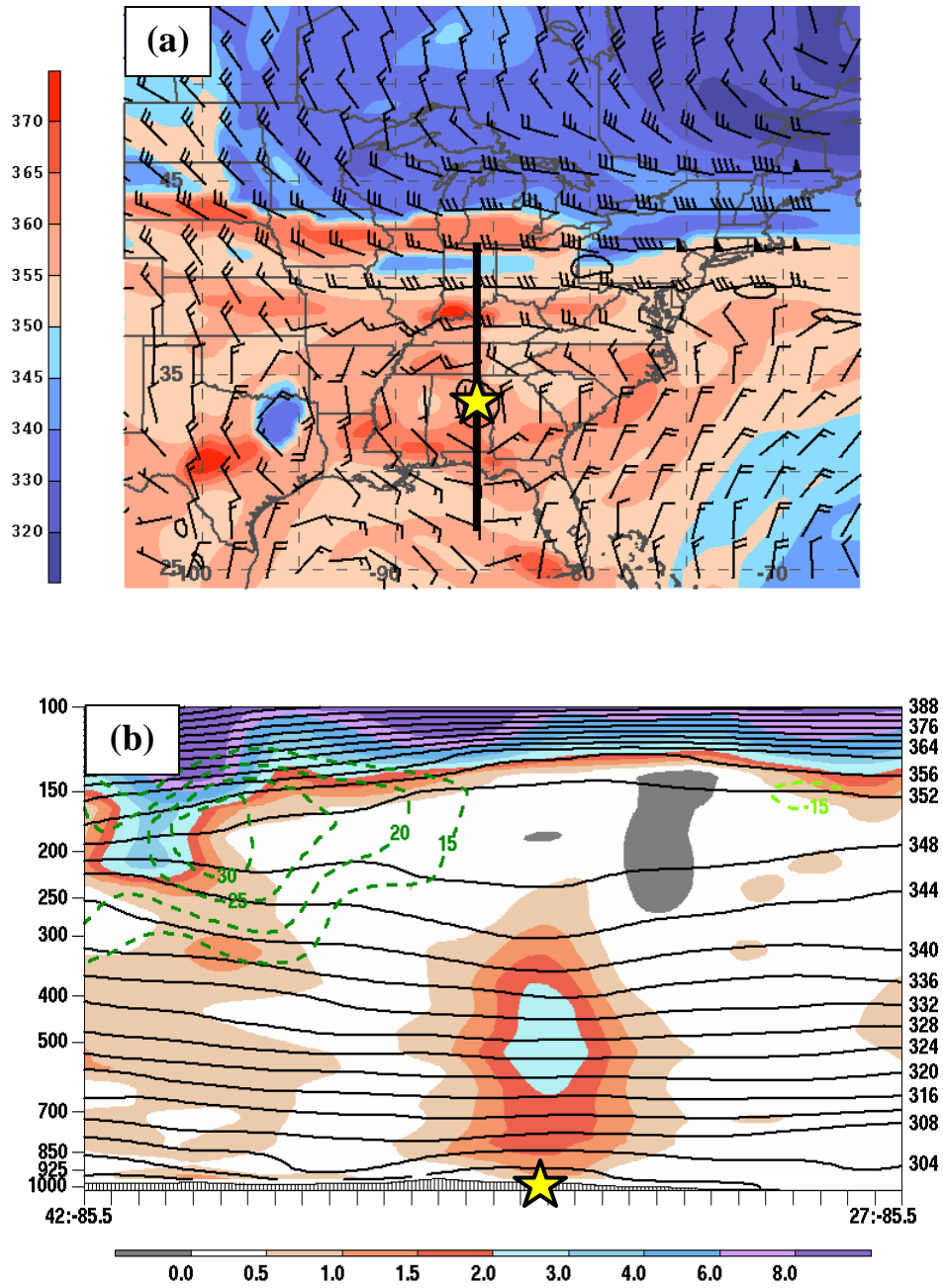


Fig. 4.10. Same as Fig. 4.9, except at 0600 UTC 23 July 1997. The black line in (a) denotes the location of the vertical cross section shown in Fig. 4.10b.

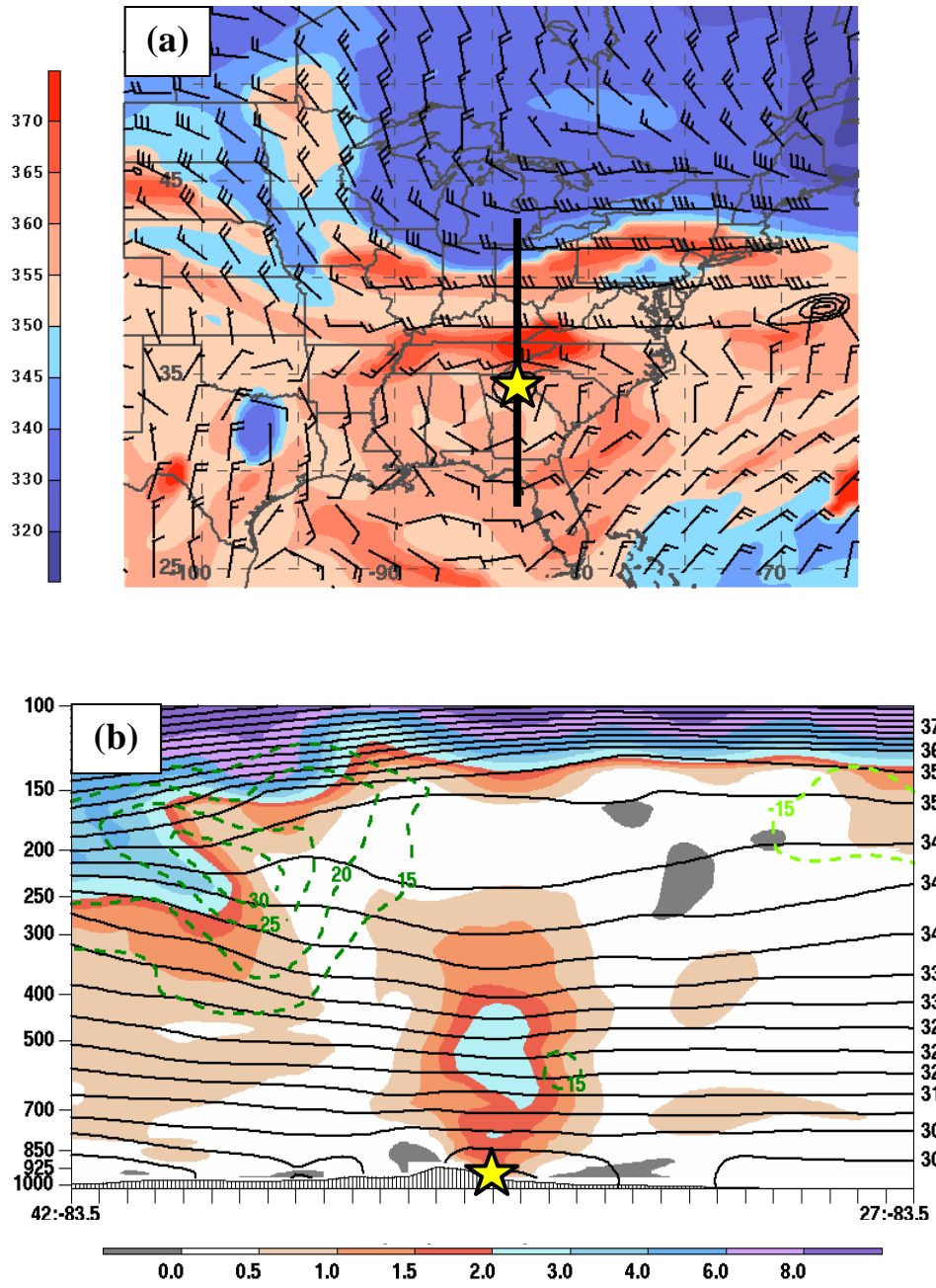


Fig. 4.11. Same as Fig. 4.9, except at 1800 UTC 23 July 1997. The black line in (a) denotes the location of the vertical cross section shown in Fig. 4.11b and Fig. 4.33.

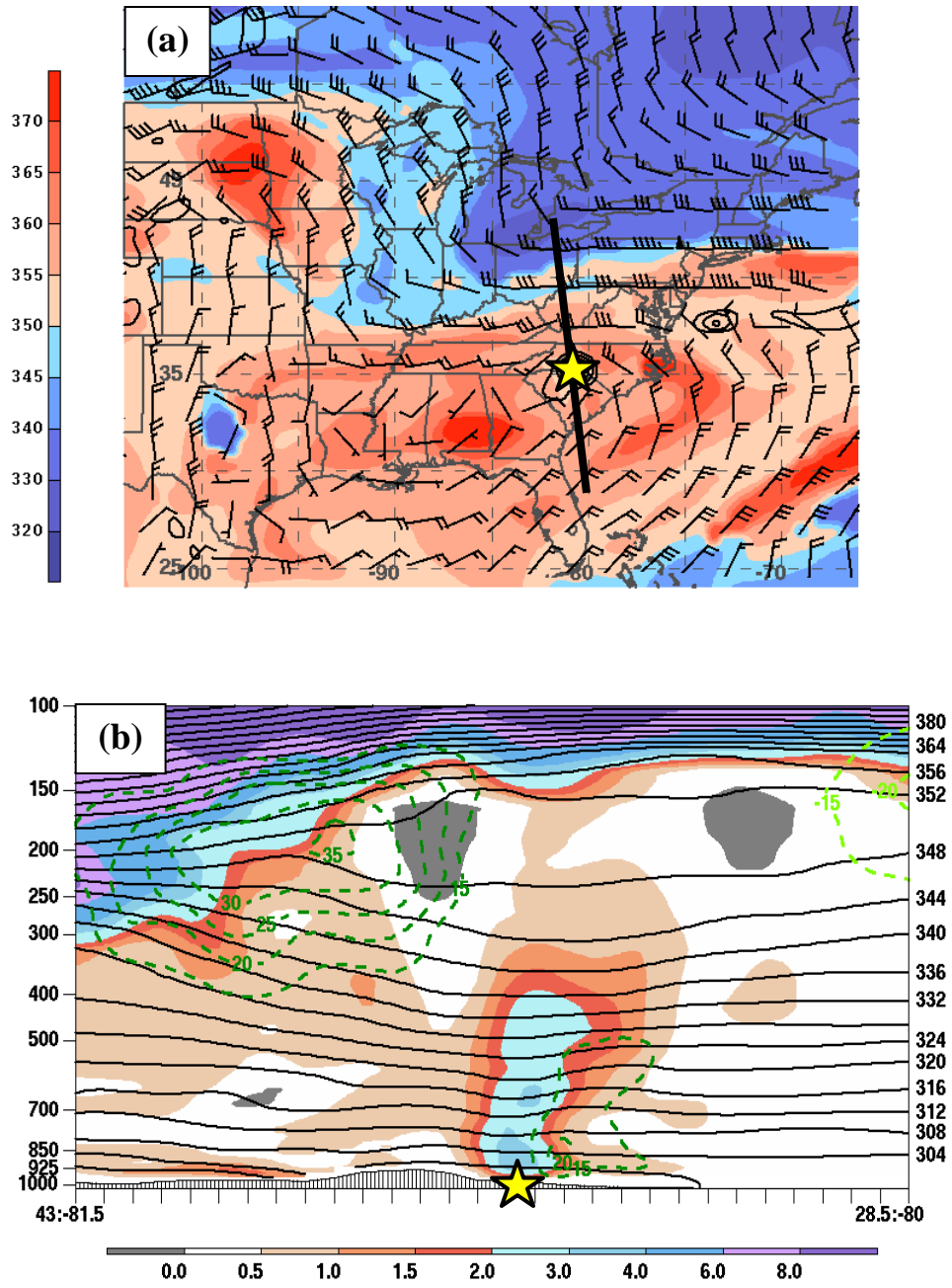


Fig. 4.12. Same as Fig. 4.9, except at 0600 UTC 24 July 1997. The black line in (a) denotes the location of the vertical cross section shown in Fig. 4.12b and Fig. 4.34.

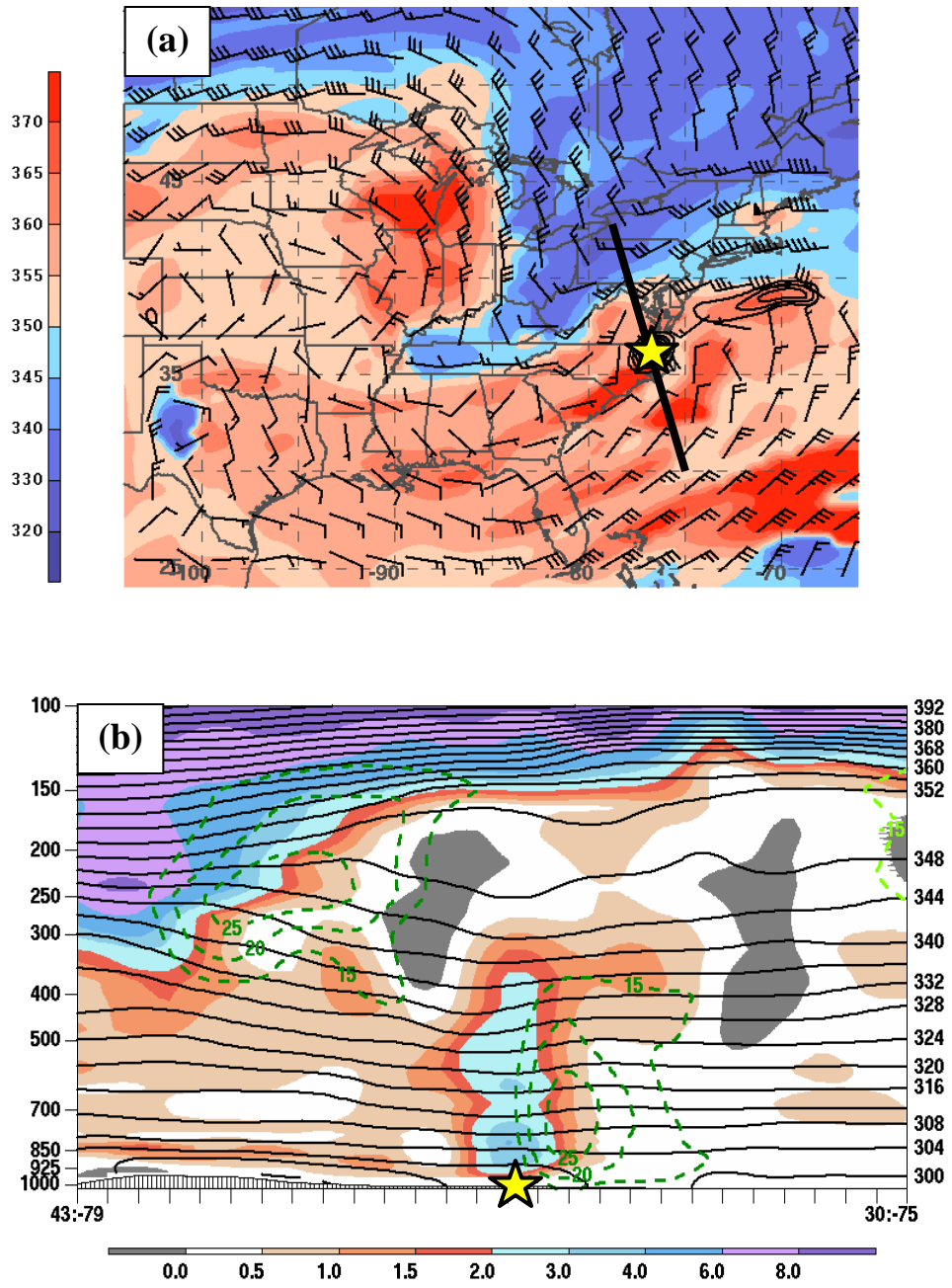


Fig. 4.13. Same as Fig. 4.9, except at 1800 UTC 24 July 1997. The black line in (a) denotes the location of the vertical cross section shown in Fig. 4.13b and Fig. 4.35.

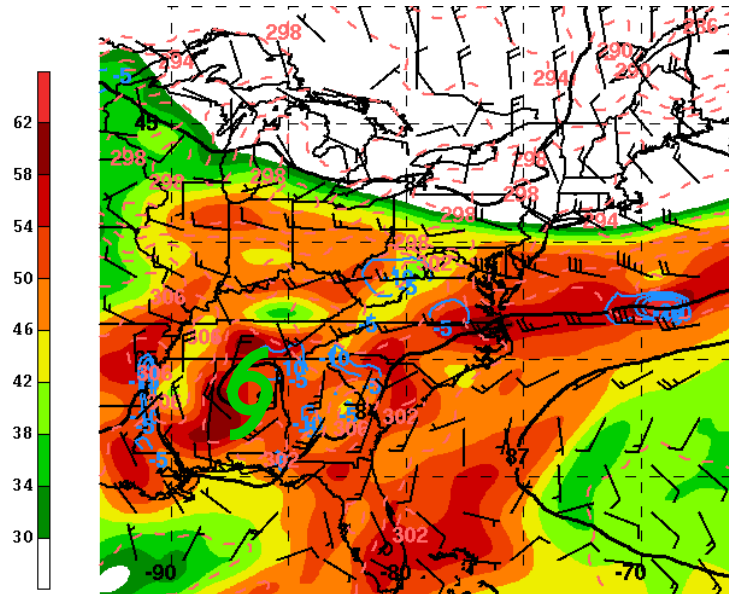


Fig. 4.14. Map of PW (shaded, mm), 700-hPa vertical motion (light blue contour every $5 \times 10^{-3} \text{ hPa s}^{-1}$, negative values only), 925-hPa geopotential height (solid black every 3 dam), 925-hPa potential temperature (dashed pink every 2 K), and 925-hPa winds (barbs, kt) at 1800 UTC 22 July 1997. The green TC symbol denotes the position of TC Danny as depicted by the CFSR.

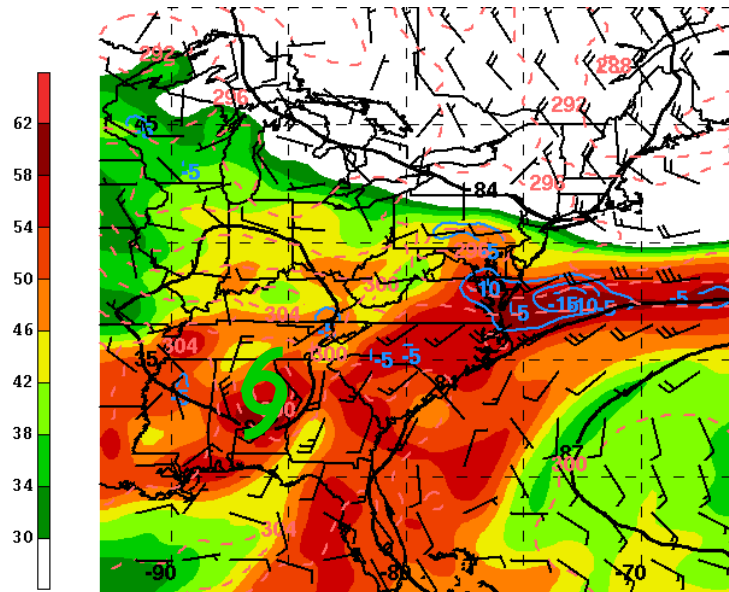


Fig. 4.15. Same as Fig. 4.14, except at 0600 UTC 23 July 1997.

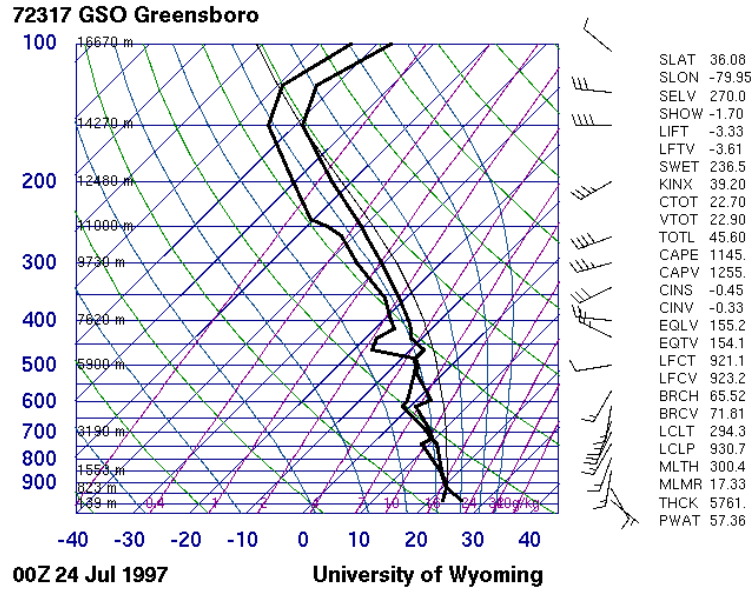


Fig. 4.18. Observed Greensboro, North Carolina (KGSO), sounding valid at 0000 UTC 24 July 1997.

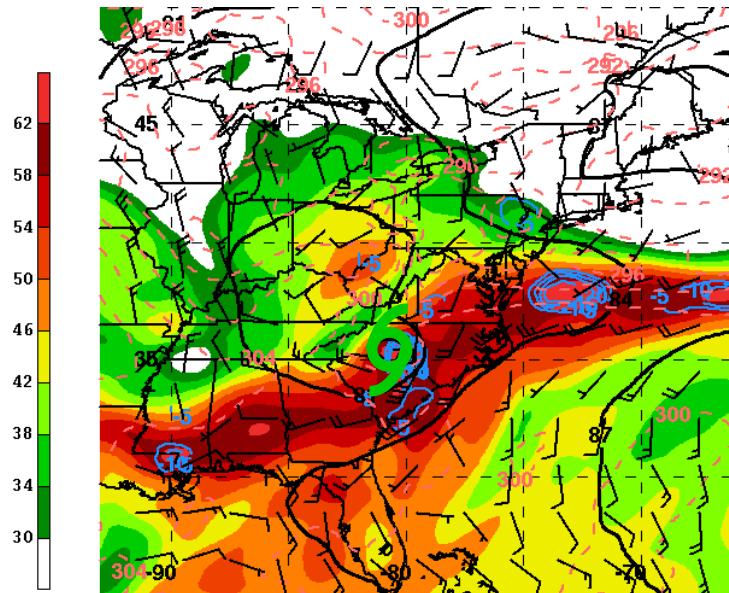


Fig. 4.19. Same as Fig. 4.14, except at 0600 UTC 24 July 1997.

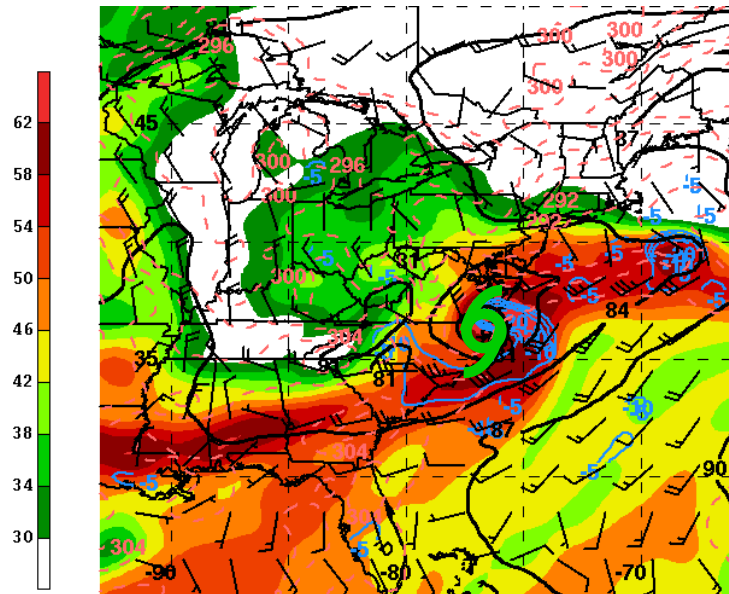


Fig. 4.20. Same as Fig. 4.14, except at 1800 UTC 24 July 1997.

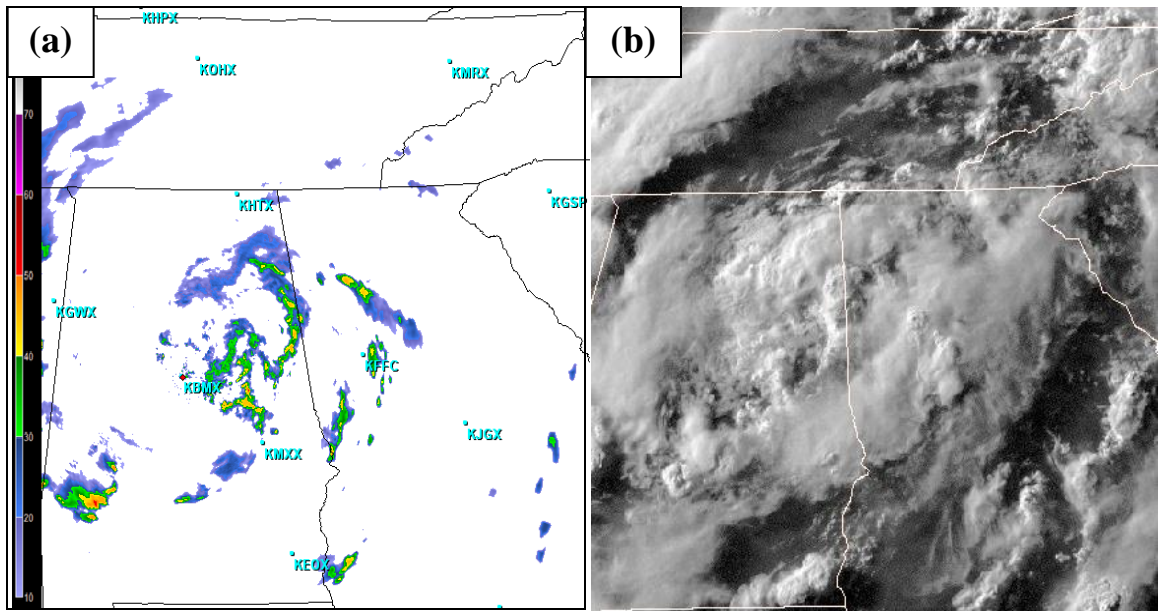


Fig. 4.21. (a) WSR-88D 0.5° base reflectivity image from Birmingham, Alabama (KBMX), taken at 0013 UTC 23 July 1997. (b) GOES-8 visible satellite image taken at 2315 UTC 22 July 1997.

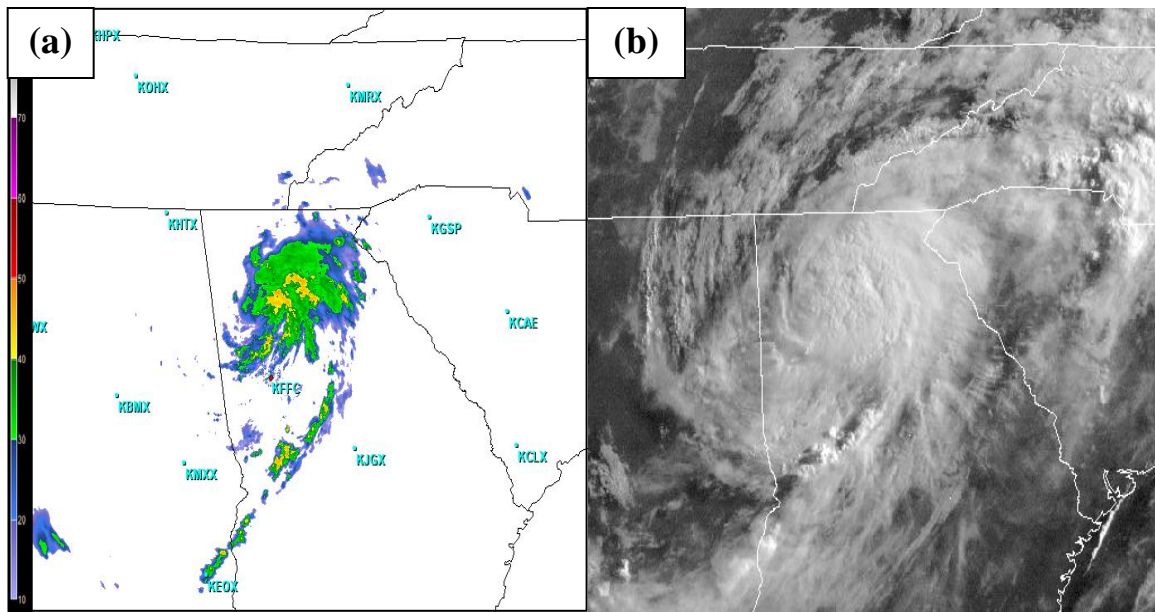


Fig. 4.22. (a) WSR-88D 0.5° base reflectivity image from Atlanta, Georgia (KFFC), taken at 1218 UTC 23 July 1997. (b) GOES-8 visible satellite image taken at 1215 UTC 23 July 1997.

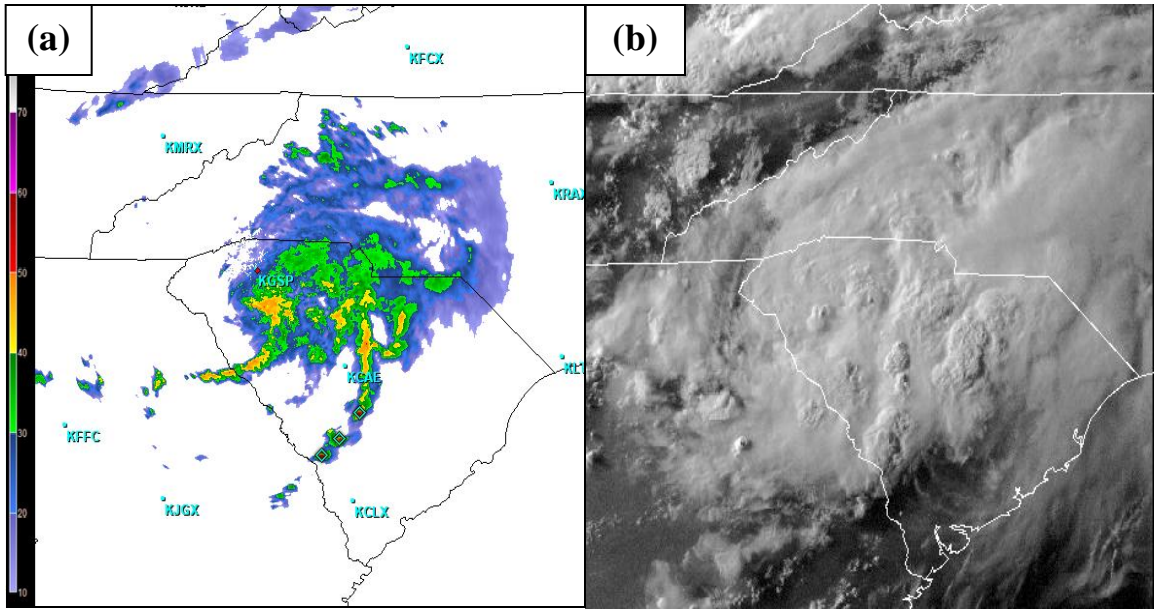


Fig. 4.23. (a) WSR-88D 0.5° base reflectivity image from Greer, South Carolina (KGSP), taken at 0015 UTC 24 July 1997. (b) GOES-8 visible satellite image taken at 2315 UTC 23 July 1997.

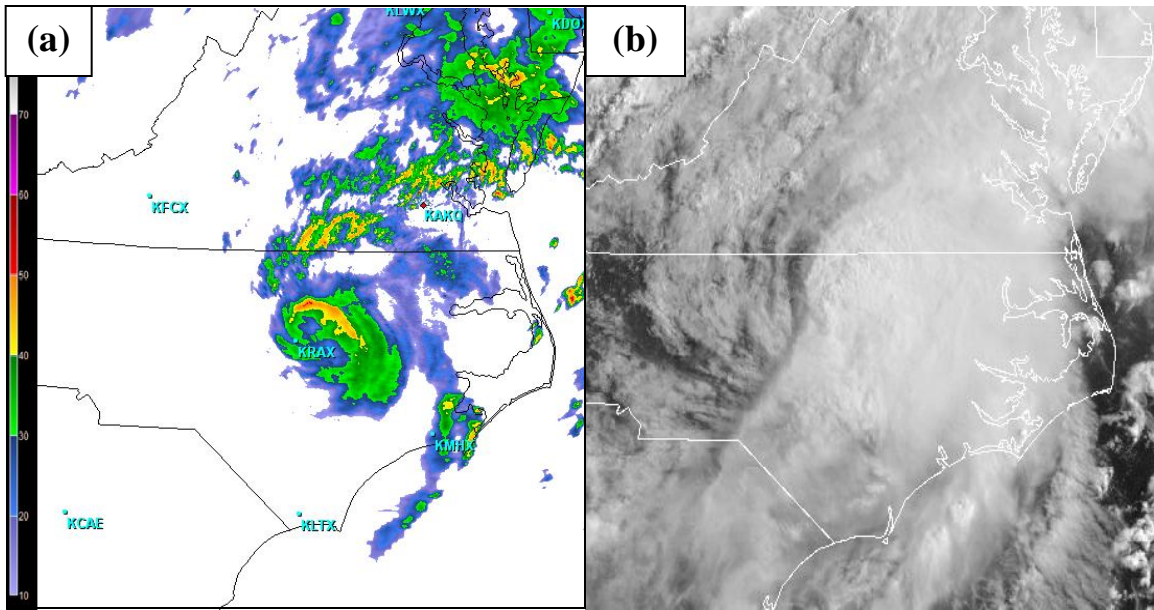


Fig. 4.24. (a) WSR-88D 0.5° base reflectivity image from Wakefield, Virginia (KAKQ), taken at 1318 UTC 24 July 1997. (b) GOES-8 visible satellite image taken at 1315 UTC 24 July 1997.

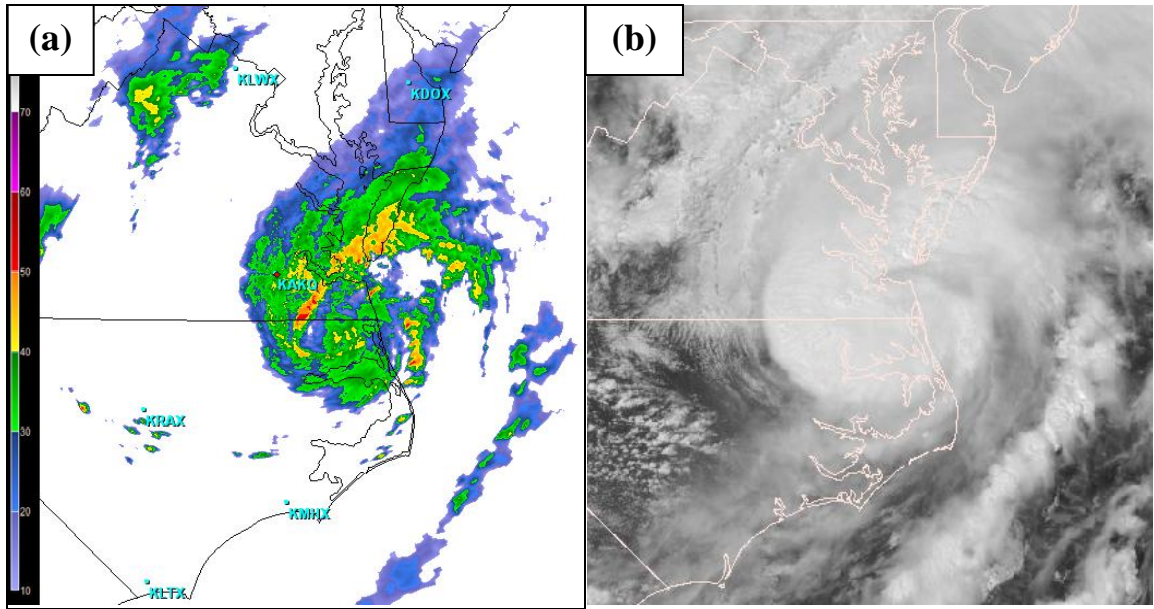


Fig. 4.25. (a) WSR-88D 0.5° base reflectivity image from Wakefield, Virginia (KAKQ), taken at 1814 UTC 24 July 1997. (b) GOES-8 visible satellite image taken at 1815 UTC 24 July 1997.

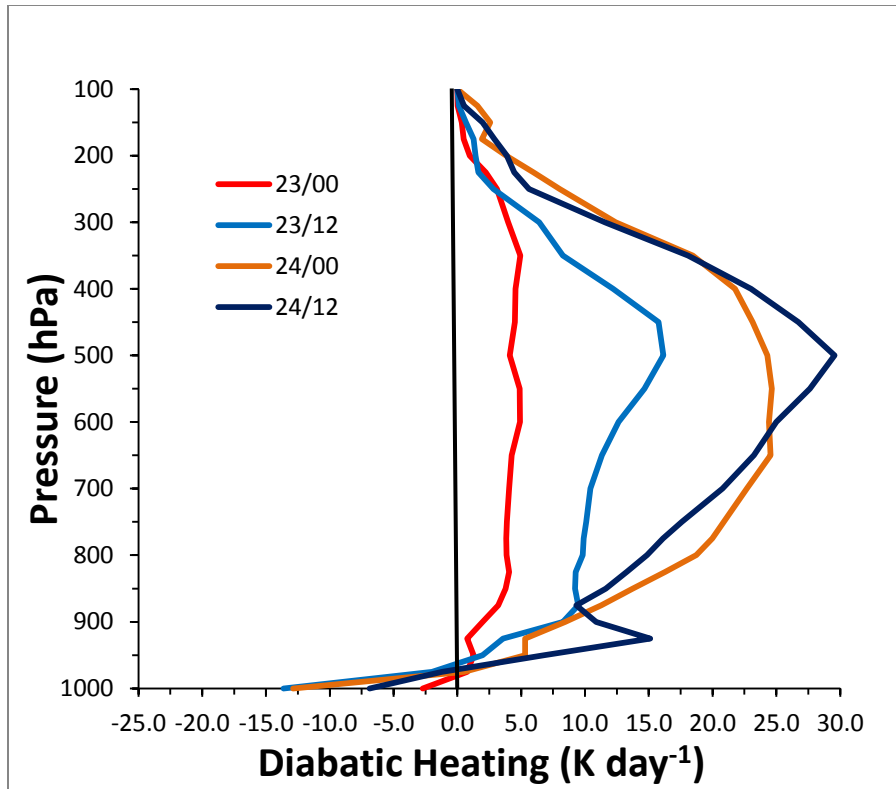


Fig. 4.26. Vertical profiles of diabatic heating averaged in a $3^\circ \times 3^\circ$ box around TC Danny valid between 0000 UTC 23 July and 1200 UTC 24 July. Each colored line represents the valid forecast time (DD/HH format).

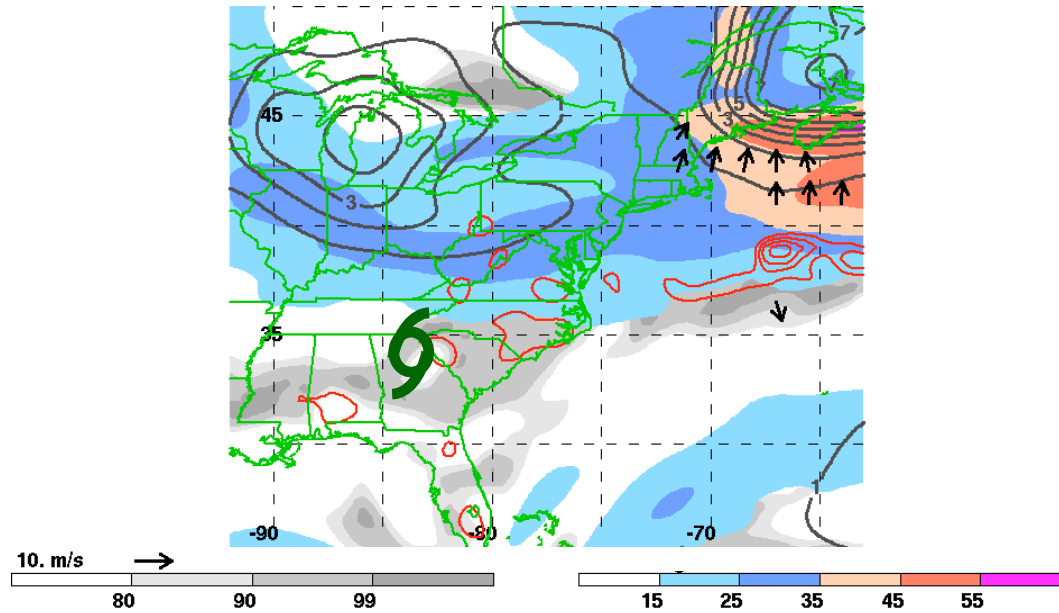


Fig. 4.27. Map of 250-hPa wind speed (shading, kt), 250-hPa PV (solid gray every 1 PVU), 250-hPa relative humidity (gray shading, %), 600–400-hPa layer-averaged vertical motion (solid red every $4 \times 10^{-3} \text{ hPa s}^{-1}$, negative values only), and 300–200-hPa layer-averaged irrotational wind (vectors starting at 5 m s^{-1}) at 1800 UTC 23 July 1997. The green TC symbol denotes the position of TC Danny as depicted by the CFSR.

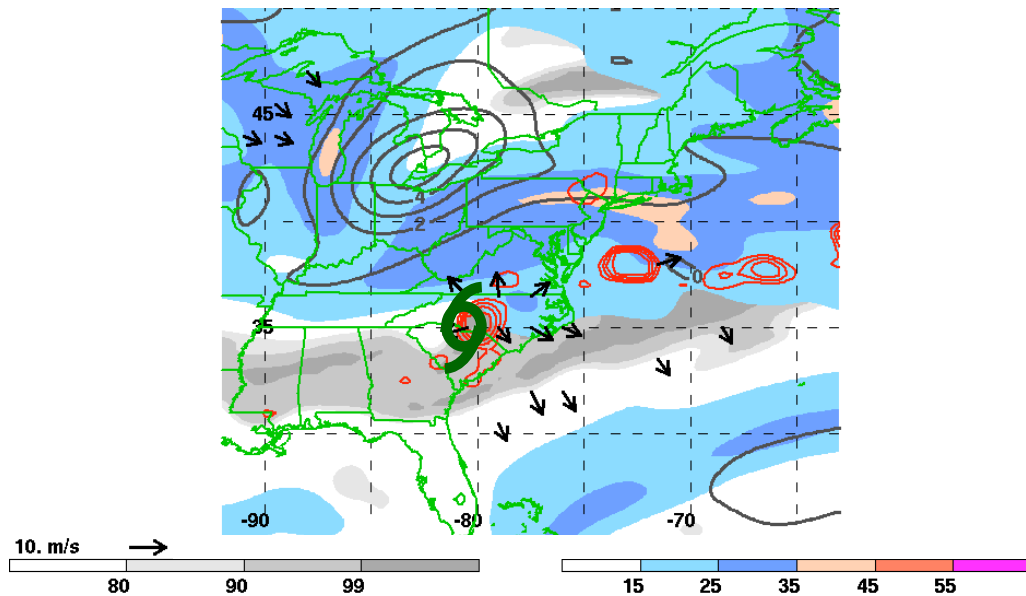


Fig. 4.28. Same as Fig. 4.27, except at 0600 UTC 24 July 1997.

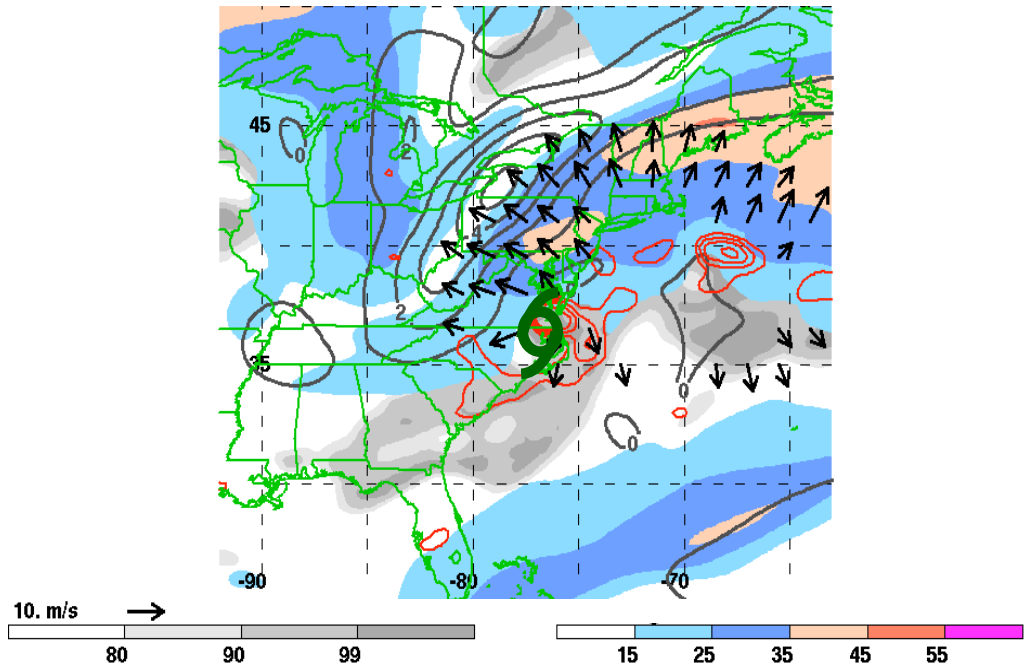


Fig. 4.29. Same as Fig. 4.27, except at 1800 UTC 24 July 1997.

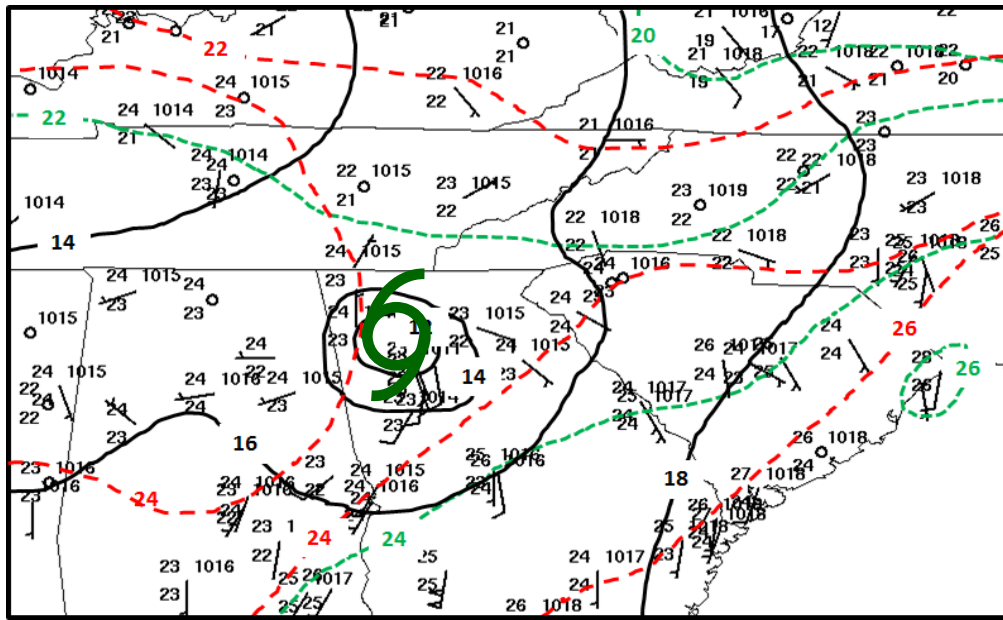


Fig. 4.30. Surface analysis at 1200 UTC 23 July 1997 displaying MSLP (solid black every 2 hPa), winds (barbs, kt), dewpoint (dashed green every 2°C), and temperature (dashed red every 2°C). The green TC symbol denotes the position of TC Danny as depicted by the CFSR.

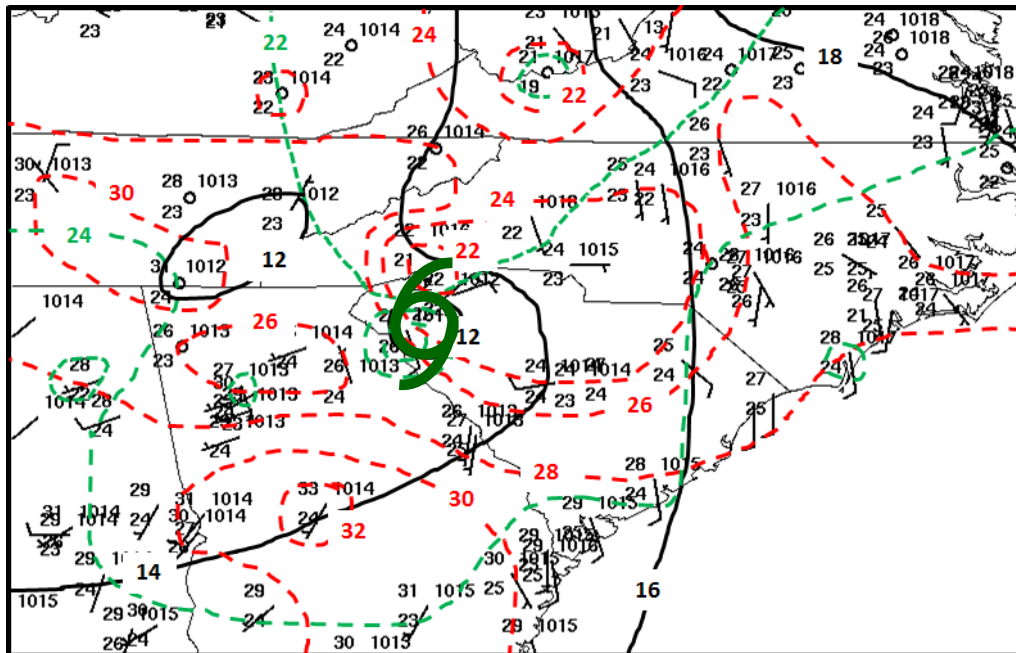
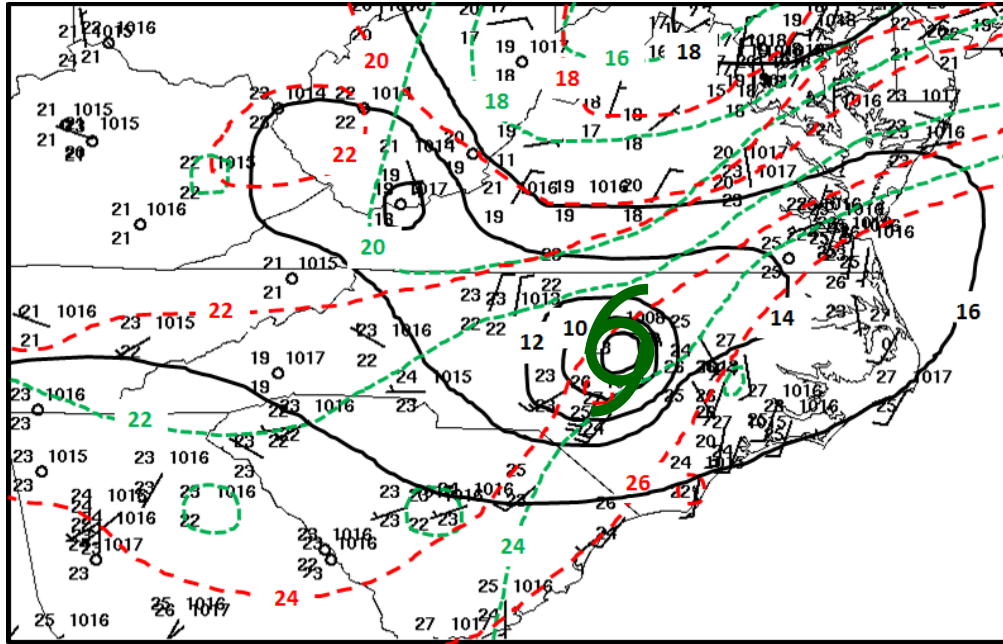


Fig. 4.31. Same as Fig. 3.30, except at 0000 UTC 24 July 1997.



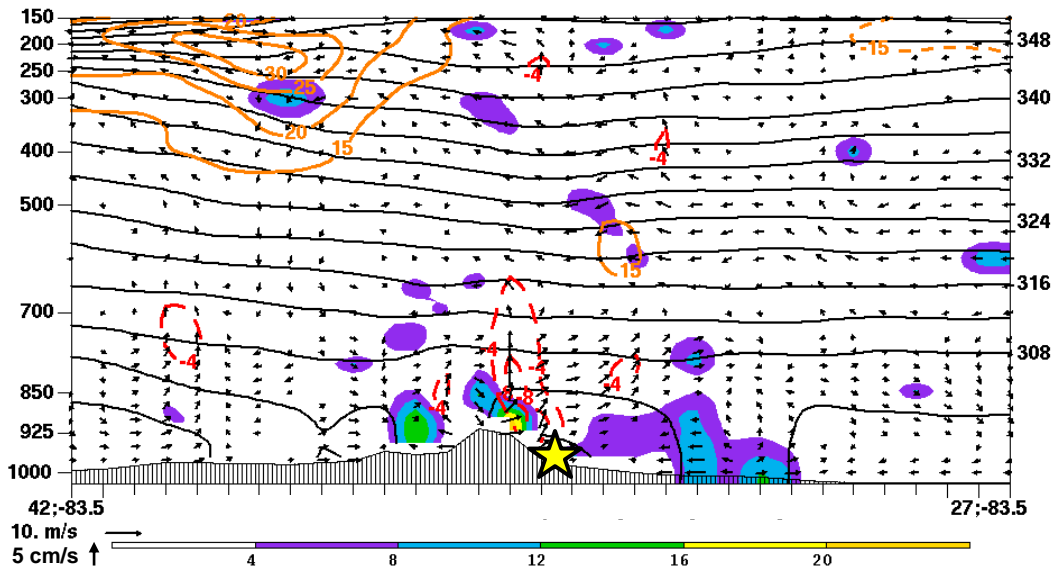


Fig. 4.33. North–south vertical cross section of Petterssen frontogenesis [shaded, $\text{K} (100 \text{ km})^{-1} (3 \text{ h})^{-1}$], potential temperature (solid black every 4 K), vertical motion (dashed red every $4 \times 10^{-3} \text{ hPa s}^{-1}$, negative values only), horizontal wind speed (solid orange every 5 m s^{-1} starting at 15 m s^{-1}), and the ageostrophic wind component tangential to the cross section (arrows, m s^{-1}) at 1800 UTC 23 July 1997. The yellow star denotes the position of TC Danny as depicted by the CFSR. The location of the vertical cross section is shown in Fig. 4.11.

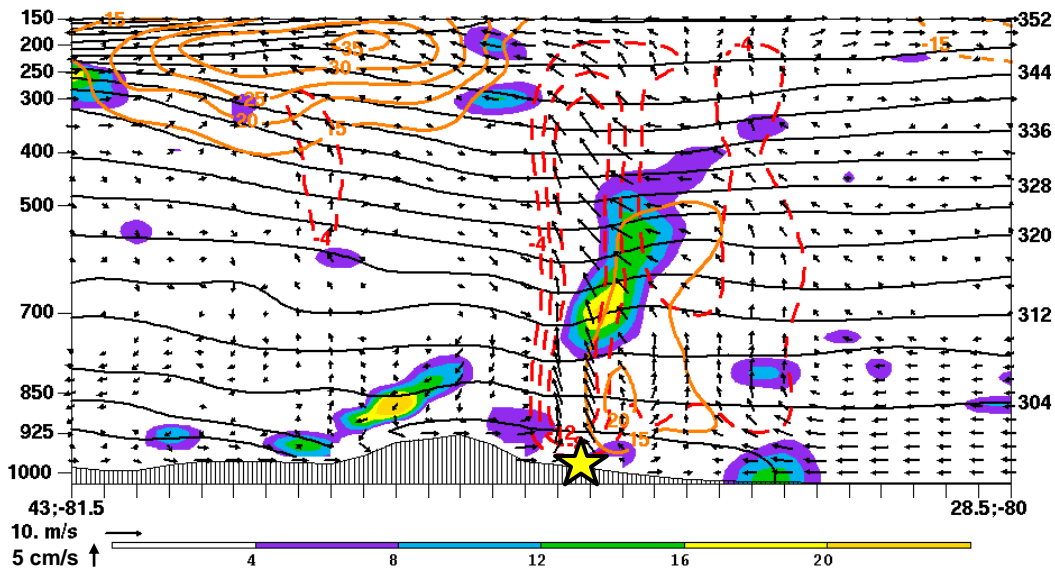


Fig. 4.34. Same as Fig. 4.33, except a north–northwest–south–southeast vertical cross section at 0600 UTC 24 July 1997. The location of the vertical cross section is shown in Fig. 4.12.

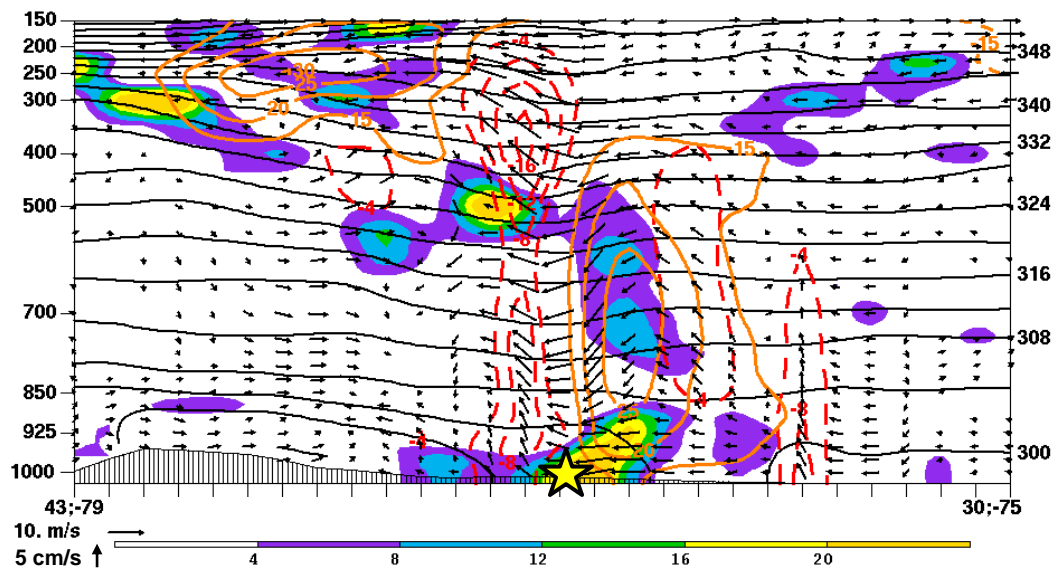


Fig. 4.35. Same as Fig. 4.33, except a north-northwest–south-southeast vertical cross section at 1800 UTC 24 July 1997. The location of the vertical cross section is shown in Fig. 4.13.

5. Discussion, Conclusions, and Suggestions for Future Work

5.1 Discussion of Multiscale Analyses

Similarities and differences between the two multiscale analyses [TC Camille (1969) and TC Danny (1997)] will be presented in this section. As was documented earlier in this thesis, TC Camille produced a high-impact flooding event over west-central Virginia in the 12-h period starting 0000 UTC 20 August, whereas TC Danny underwent inland reintensification while moving across the Carolinas on 24 July 1997. The most notable similarity between the two TCs is that both storms crossed the Appalachian Mountains and interacted with an equatorward entrance region of an upper-tropospheric jet located poleward over the northeast United States. Although a maximum wind speed in the upper-tropospheric jet poleward of TC Camille and TC Danny was 45 m s^{-1} and 35 m s^{-1} , respectively, TC Danny was situated closer to the equatorward entrance region of the weaker upper-tropospheric jet than TC Camille was to the stronger upper-tropospheric jet. Accordingly, TC Danny was able to interact with the equatorward entrance region of the weaker upper-tropospheric jet more directly.

The presence of a lower-tropospheric baroclinic zone associated with a surface frontal boundary was observed in both TC cases as well. A surface cold front associated with the TC Camille case was important throughout the inland flooding event over west-central Virginia. In addition to the synoptic-scale ascent beneath the equatorward entrance region of the upper-tropospheric jet poleward of TC Camille, frontogenesis along the lower-tropospheric baroclinic zone associated with the surface front forced additional ascent over Nelson County, the area that received copious amounts of rainfall during the inland flooding event (maximum rainfall of 690 mm over Massies Mill,

Virginia, during the 12-h period stated in section 3.1.2). A stationary surface front observed in the TC Danny case had an associated lower-tropospheric baroclinic zone that was located over Virginia. In addition to synoptic-scale ascent in the equatorward entrance region of the upper-tropospheric jet, frontogenesis along the lower-tropospheric baroclinic zone forced additional ascent around the circulation of TC Danny as the TC moved into northeastern North Carolina on 24 July.

A highly moist environment ($PW > 50$ mm) was an additional similarity between the two TC cases, but the moist conditions played different roles in each case. A moist, southerly flow ahead of TC Camille likely provided sufficient instability in west-central Virginia to promote the development and maintenance of heavy rainfall and convection. In the case of TC Danny, PW values exceeding 50 mm were located around the TC circulation and promoted the initiation and maintenance of convection prior to and during its inland reintensification. Available observed soundings exhibited a moist and unstable environment within which TC Danny was embedded.

One of the main differences between the TC Camille and TC Danny cases was the orientation of the midlatitude flow poleward of each TC. A broad, closed-off upper-level low associated with a quasi-stationary extratropical cyclone to the northeast of TC Camille prohibited inland reintensification from occurring. In addition, a quasi-stationary positive PV anomaly was coincident with the broad upper-level low. This synoptic setup is similar to the “northeast” pattern described by Harr et al. (2000), in that it is characterized by a quasi-stationary midlatitude system to the northeast of a poleward-moving TC. The strong confluent zonal flow into which a TC enters was a determining factor explaining why the TC does not intensify significantly (Harr et al. 2000). In this

setup, minimal baroclinic development occurs, which leads to a minimal strengthening of the TC (Harr et al. 2000). Conversely, TC Danny had an upper-tropospheric trough to the northwest, which was coincident with an upper-tropospheric positive PV anomaly. Hanley et al. (2001) found that this setup could produce a “favorable distant interaction” between a TC and an upper-tropospheric positive PV anomaly. The comparable size of the positive PV anomaly and TC Danny was important in minimizing adverse effects of vertical wind shear on the TC circulation. Bosart et al. (2000) showed that ascent associated with a positive PV anomaly likely acts to organize deep convection, thereby resulting in an upscale development of convection into clusters. As a result of this upscale development, the positive PV anomaly becomes comparable in size to the clustered area of deep convection (Molinari et al. 1995, 1998; Bosart et al. 2000). The comparably sized positive PV anomaly would likely exhibit less vertical wind shear and would therefore be more favorable for TC intensification (Molinari et al. 1995, 1998; Bosart et al. 2000).

Another difference between the TC Camille and TC Danny cases was a thermal advection pattern in the equatorward entrance region of an upper-tropospheric jet. Cold-air advection in the lower-troposphere analyzed poleward of TC Camille acted to oppose ascent in the middle and upper troposphere beneath an equatorward entrance region of an upper-tropospheric jet. This situation suggests that the ascent associated with frontogenesis observed along a lower-tropospheric baroclinic zone was an important forcing mechanism in the inland flooding that occurred during TC Camille’s transit across the central Appalachian Mountains. In the TC Danny case, on the other hand, lower-tropospheric warm-air advection, although weak, was analyzed northeast of TC

Danny and acted to force ascent beneath an equatorward entrance region of an upper-tropospheric jet. The ascent associated with this area of warm-air advection not only favored the development of rainfall and convection around TC Danny's inner core, but also to the northeast of TC Danny as well. The area of rainfall to the northeast of TC Danny contributed to a diabatically driven upper-tropospheric outflow. Negative PV advection by the irrotational wind in this diabatically driven outflow acted to strengthen the cross-jet PV gradient poleward of TC Danny. This strengthened PV gradient was associated with a strengthening of the upper-tropospheric jet poleward of TC Danny and with increased ascent over the storm.

Effects of vertical wind shear were an important difference between the two cases as well. Within several days after making landfall, TC Camille had weakened into a tropical depression and headed into an environment where vertical wind shear started to tilt the TC circulation. A broad positive PV anomaly to the northeast of TC Camille strongly influenced the TC circulation as the storm traversed the Appalachian Mountains. As previously mentioned, the reduced vertical wind shear associated with the comparably sized positive PV anomaly affecting TC Danny was favorable for its inland reintensification. In the case of TC Camille, a broad PV anomaly meant that stronger shear was present, which prevented the redevelopment of the TC. Prior to its inland reintensification, TC Danny spent several days in an environment that was characterized by low shear. This environment was very important in preserving the preexisting vortex of the TC and the associated rainfall and convection. As TC Danny moved toward the Carolinas, vertical wind shear values increased from 2.5 m s^{-1} to 5 m s^{-1} and were coincident with an organization and development of convection near the center of the TC

circulation. Diabatic heating associated with the convection favored the development of PV and cyclonic relative vorticity toward the surface, which strengthened the TC vortex and subsequently led to its inland reintensification. By the time TC Danny encountered higher vertical shear than when the TC was over Alabama and Georgia, the diabatically driven outflow associated with the TC negated the effects of vertical wind shear.

A process unique to the TC Camille case was an orographic enhancement of rainfall induced by upslope flow across the Blue Ridge Mountains over west-central Virginia during the inland flooding event associated with the storm. Locations in Nelson County that received copious amounts of rainfall were on south- and southeast-facing slopes, indicative of the importance of orography in this inland flooding event. An analysis of the Big Thompson flood from 31 July 1976 (Caracena et al. 1979) showed that mountainous terrain was key to that inland flooding event. Physical mechanisms leading to its severity were a prolonged upslope flow and a continuous replenishment of moisture and instability by the larger-scale flow (Caracena et al. 1979). These physical mechanisms were similar to the TC Camille case, and the flooding associated with TC Camille was exacerbated by frontogenetically forced ascent along a lower-tropospheric baroclinic zone.

The TC Camille inland flooding case closely resembled a “frontal” pattern for flash-flooding-producing MCSs (Maddox et al. 1979), where warm, moist air is transported by a lower-tropospheric jet toward a west–east quasi-stationary lower-tropospheric baroclinic zone. In addition, the synoptic setup in the TC Camille case was similar to a DC category PRE described by Moore (2010). A DC category PRE develops beneath an equatorward entrance region of an upper-tropospheric jet positioned within a

region of upper-level confluent flow associated with a trough-over-ridge pattern situated downstream of a TC (Moore 2010). This type of PRE is associated with deep moist southerly flow on the eastern flank of the TC circulation that is transported into the PRE region (Moore 2010). Synoptic-scale ascent beneath the equatorward entrance region of the upper-tropospheric jet is reinforced by subsynoptic-scale ascent associated with frontogenetical forcing and warm-air advection (Moore 2010).

Conceptual models of the aforementioned similarities and differences between the two TC–jet interaction cases, in addition to other important tropospheric features and processes unique to each case, are found in Figs. 5.1a,b. The conceptual model in Fig. 5.1a that characterizes the TC Camille heavy rain event could be used as a source of forecast guidance for future events that may resemble a “Camille-like” situation. If upper-level flow poleward of a TC that crosses the central Appalachian Mountains is characterized by an upper-tropospheric jet located within a region of upper-level confluent flow across the northeast United States, a heavy rain event is likely, with the rainfall especially heavy in orographically favored regions (Fig. 5.1a). This confluent flow also contains an upper-tropospheric positive PV anomaly coincident with a broad, upper-level low located over southeastern Quebec and an upper-level high off the southeastern United States coast (Fig. 5.1a). Cold air-advection upstream of this confluent flow and beneath an equatorward entrance region of an upper-tropospheric jet (Fig. 5.1a) acts to suppress ascent beneath this jet-entrance region. This cold air-advection is located on the cold side of a west–east oriented quasi-stationary lower-tropospheric baroclinic zone located across the Mid-Atlantic region. The warm side of this quasi-stationary lower-tropospheric baroclinic zone is characterized by moist, low-

level southerly flow on the eastern flank of the TC circulation (Fig. 5.1a). Forcing for ascent in the area of heaviest rainfall is associated with frontogenesis along this lower-tropospheric baroclinic zone. Additional ascent is forced by an upslope flow induced by mountainous terrain across the central Appalachian Mountains (Fig. 5.1a).

Prognoses of future events that may resemble a “Danny-like” situation could benefit from using the conceptual model displayed in Fig. 5.1b. Prior to interacting with the poleward midlatitude flow, a TC is embedded within a low-shear and moist environment (Fig. 5.1b) that acts to help preserve a preexisting vortex and convection associated with a TC. As the TC moves toward the east, convection around the TC circulation starts to organize and develop as a result of a favorable moist thermodynamic environment characterized by deep instability. This organization of convection leads to an increase in maximum heating at midlevels. Below the level of maximum heating, cyclonic relative vorticity and PV increases, which enables the TC vortex to strengthen. The TC subsequently reintensifies as upper-level features (e.g., upstream positive PV anomaly and poleward upper-tropospheric jet) provide forcing for favorable synoptic-scale ascent over the TC circulation (Fig. 5.1b). Negative PV advection by the irrotational wind in diabatically driven outflow associated with the TC (Fig. 5.1b) acts to enhance a cross-jet PV gradient poleward of the TC. This enhanced PV gradient strengthens an upper-tropospheric jet and increases ascent over the TC. Frontogenesis along a lower-tropospheric baroclinic zone and warm-air advection northeast of the TC (Fig. 5.1b) provide additional forcing for ascent around the TC circulation.

5.2 Conclusions

The main objectives of this research were to: (1) document the synoptic-scale environment and underlying mesoscale processes responsible for inland flooding associated with TC Camille (1969) and the inland reintensification of TC Danny (1997); (2) explain similarities and differences between the TC Camille and TC Danny cases; and (3) document important physical mechanisms and processes that lead to various impacts associated with inland TC–midlatitude jet interactions. To accomplish these objectives, important tropospheric features and processes were identified in each case using reanalysis datasets, observational data, and a PV analysis perspective. TC Camille produced a high-impact inland flooding event over west-central Virginia on 20 August 1969, where 690 mm of rain fell over Massies Mill, Virginia, in the 12-h period starting 0000 UTC 20 August. TC Danny, on the other hand, underwent significant inland reintensification over the Carolinas on 24 July 1997, where its minimum central MSLP decreased from 1012 hPa to 1000 hPa and its maximum sustained wind speed increased from 20 kt to 40 kt in the 18-h period starting 0000 UTC 24 July.

Documentation of both TC–jet interaction cases showed that each TC was situated underneath an equatorward entrance region of an upper-tropospheric jet. In addition to being positioned beneath an equatorward entrance region of an upper-tropospheric jet, both TCs interacted with a lower-tropospheric baroclinic zone associated with a surface frontal boundary. Furthermore, TCs Camille and Danny were embedded within a highly moist environment, which likely provided instability that supported the initiation and maintenance of convection.

Important differences between the TC Camille and TC Danny cases included the orientation of the upper-level flow poleward of each TC. Specifically, the location and large spatial scale of a quasi-stationary upper-tropospheric positive PV anomaly to the northeast of TC Camille was deemed to have a negative influence on the TC. This negative influence was due to strong vertical wind shear induced by the quasi-stationary positive PV anomaly, which acted to tilt and weaken the circulation of the storm. A positive PV anomaly to the northwest of TC Danny interacted favorably with the TC by forcing synoptic-scale ascent over the TC circulation. The effects of increased vertical wind shear over TC Danny were negated by diabatically driven upper-tropospheric outflow from TC-related heavy rainfall that acted to build a ridge near the storm center. Furthermore, a thermal advection pattern beneath the equatorward entrance region of an upper-tropospheric jet poleward of TC Camille acted to suppress ascent in the region where cold-air advection was indicated. In the TC Danny case, warm-air advection acted to force ascent beneath the equatorward entrance region of an upper-tropospheric jet.

Conceptual models characterizing the two case studies show important synoptic-scale and mesoscale mechanisms and processes that lead to various inland impacts associated with TC–midlatitude jet interactions. “Camille-like” events, which can lead to severe inland flooding, are characterized by a synoptic setup where warm, moist southerly flow ahead of a TC is directed toward a lower-tropospheric baroclinic zone beneath an equatorward entrance region of an upper-tropospheric jet located within an upper-level confluent flow. Synoptic-scale ascent over the area of heaviest rainfall is reinforced by frontogenetically forced ascent along a lower-tropospheric baroclinic zone and in the equatorward entrance region of the upper-tropospheric jet. An upslope

component of the wind induced by mountainous terrain leads to orographic enhancement of rainfall in the area of heaviest precipitation.

“Danny-like” events, which can reintensify inland, are characterized by a prior low-shear environment that helps to preserve the preexisting vortex and convection associated with a TC. The presence of moisture and instability can help to organize and reinvigorate deep convection around the TC. An increase in the convection can be linked to an increase in diabatic heating at midlevels and to an increase of cyclonic relative vorticity and PV below the level of maximum diabatic heating. Synoptic-scale ascent ahead of an upstream positive PV anomaly and in the equatorward entrance region of an upper-tropospheric jet poleward of the TC can provide a favorable environment for the TC to reintensify. Negative PV advection by the irrotational wind strengthens a poleward cross-jet PV gradient and the associated upper-tropospheric jet and enhances ascent over a TC. Frontogenesis and warm-air advection northeast of the TC also force ascent around the TC circulation.

5.3 Suggestions for Future Work

Although this thesis documented insight into mechanisms and processes associated with TC–midlatitude jet interactions, future opportunities remain to better understand relative contributions from important tropospheric features and processes associated with these interactions. For the TC Camille case, high-resolution modeling would offer an effective method for determining the relative contributions of the orography of the Blue Ridge Mountains, an upper-tropospheric jet, and a lower-tropospheric baroclinic zone. For the TC Danny case, high-resolution modeling would

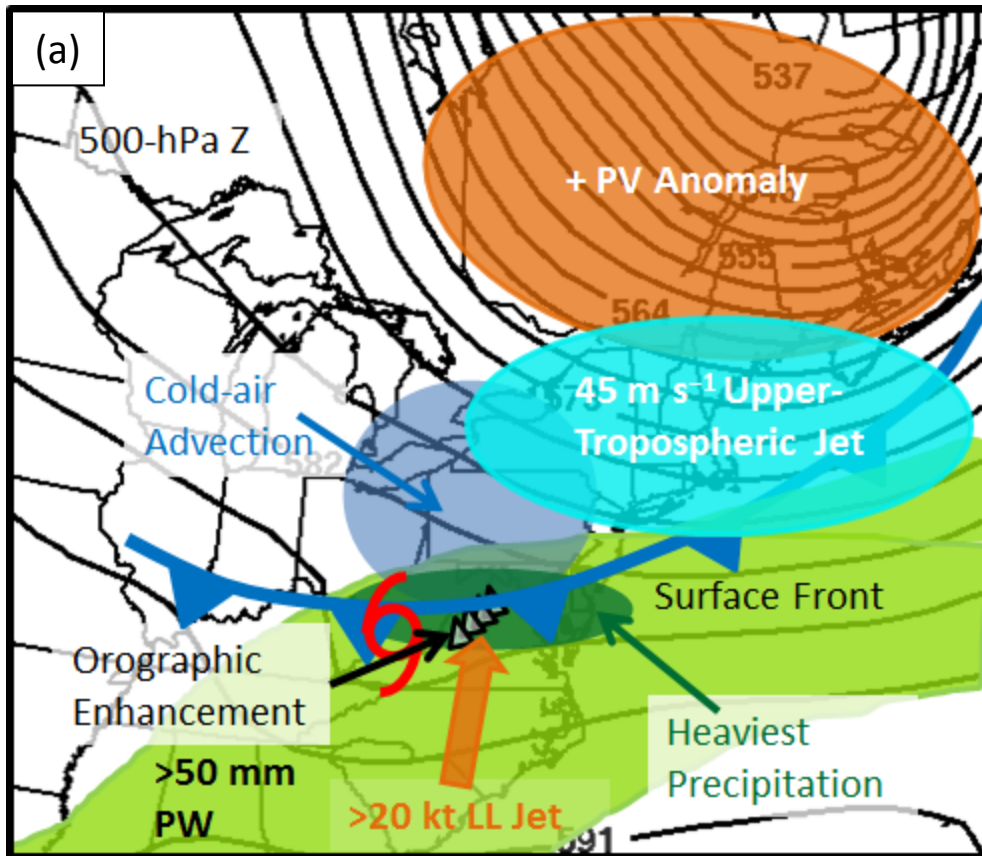
offer an effective method for determining the relative contributions of diabatic heating, an upper-tropospheric jet, and an upper-tropospheric positive PV anomaly.

As was used in a previous study (Hanley et al. 2001), EFC calculations of angular momentum quantified an interaction between a TC and an upper-tropospheric trough. Particularly for the TC Danny case, EFC calculations over a 300–600-km radial range would quantify the strength of the interaction between the TC and the upstream upper-tropospheric trough and associated positive PV anomaly. Then calculations could confirm the “favorable distant interaction” between TC Danny and the positive PV anomaly hypothesized to have taken place during the TC’s inland reintensification. A similar analysis using EFC calculations for the TC Camille case could provide insight into the factors that prevented the TC from undergoing inland reintensification.

Recalling the Evans et al. (2011) study documented in section 1.4, the inland reintensification of TC Erin over Oklahoma was found to have been impacted by anomalous wet months preceding the event. As found by Shen et al. (2002), inland reintensifying TCs have occurred in situations where the underlying surface has high heat conductivity and is relatively moist. In light of these two studies, analysis of the soil moisture along the track of TC Danny may prove to be important in explaining its inland reintensification. The PRE observed over North Carolina (section 4.1.2), a day prior to TC Danny moving across the area, may have led to favorable surface latent heat fluxes that served as an important element in the inland reintensification of the TC.

A list of inland reintensifying TCs (Table II) presented in section 4.1.3 provided a first-order historical perspective of the TC Danny case, but a further analysis of this case list provides the opportunity for future research. Specifically, a documentation of all

important tropospheric features and processes in each TC case could reveal similarities between these cases.



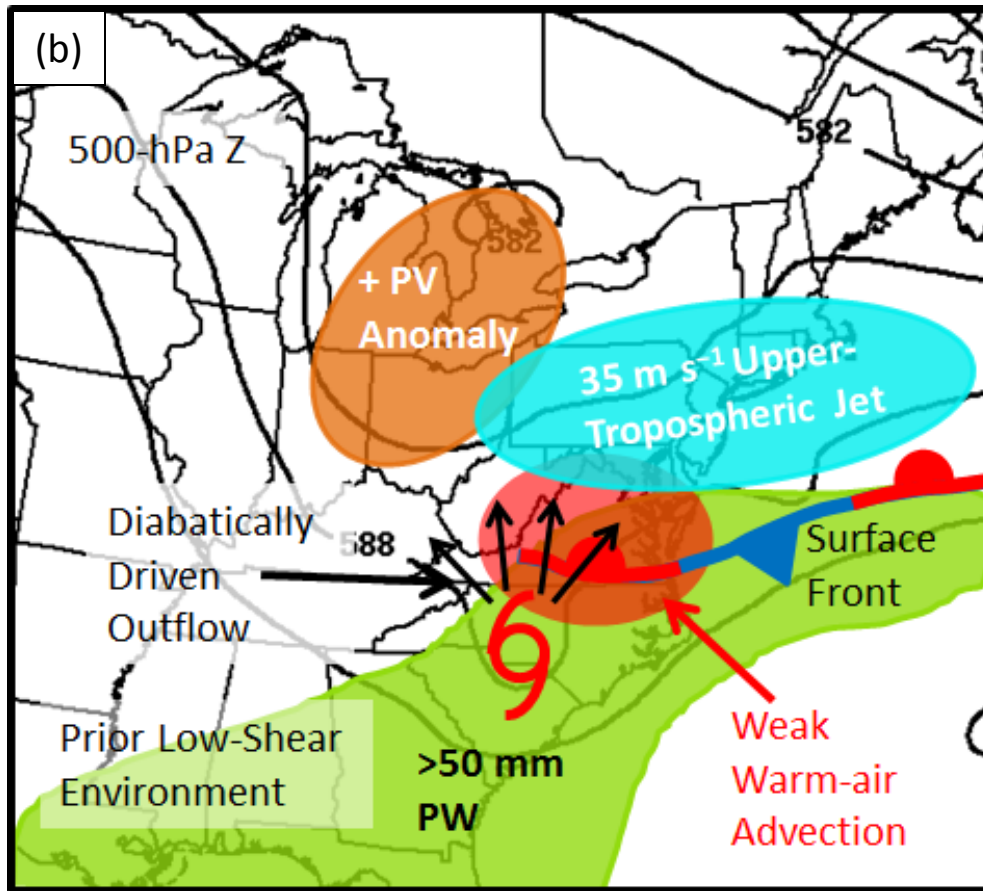


Fig. 5.1. Conceptual models depicting important mechanisms and processes leading to (a) “Camille-like” and (b) “Danny-like” events. For both conceptual models, 500-hPa geopotential height is indicated by solid black contours, the positive PV anomaly is shaded in orange, the upper-tropospheric jet is shaded in light blue, regions of warm-air advection and cold-air advection are indicated by red and blue shaded regions, respectively, and areas of PW exceeding 50 mm are shaded in light green. The red TC symbol indicates the position of the TC. (a) Low-level jet is indicated by the orange arrow. The placement of orography is indicated by the triangular symbols. The approximate area of heaviest rainfall is indicated by dark green shading. (b) Diabatically driven outflow is indicated by the black arrows emanating from the TC.

REFERENCES

- Arndt, D. S., J. B. Basara, R. A. McPherson, B. G. Illston, G. D. McManus, and D. B. Demko, 2009: Observations of the overland reintensification of Tropical Storm Erin (2007). *Bull. Amer. Meteor. Soc.*, **90**, 1079–1093.
- Atallah, E. H., and L. F. Bosart, 2003: The extratropical transition and precipitation distribution of Hurricane Floyd (1999). *Mon. Wea. Rev.*, **131**, 1063–1081.
- , ———, and A. R. Aiyyer, 2007: Precipitation distribution associated with landfalling tropical cyclones over the eastern United States. *Mon. Wea. Rev.*, **135**, 2185–2206.
- Archambault, H. M., 2011: The downstream extratropical flow response to recurring western North Pacific tropical cyclones. Ph.D. dissertation, University at Albany, State University of New York, 212 pp.
- Bassill, N. P., and M. C. Morgan, 2006: The overland reintensification of Tropical Storm Danny (1997). Preprints, *27th Conf. on Hurricanes and Tropical Meteorology*, Monterey, CA, Amer. Meteor. Soc., 6A.6. [Available online at <http://ams.confex.com/ams/pdfpapers/108676.pdf>.]
- Bosart, and D. B. Dean, 1991: The Agnes rainstorm of June 1972: Surface feature evolution culminating in inland storm redevelopment. *Wea. Forecasting*, **6**, 515–537.
- , and G. M. Lackmann, 1995: Postlandfall tropical cyclone reintensification in a weakly baroclinic environment: A case study of Hurricane David (1979). *Mon. Wea. Rev.*, **123**, 3268–3291.
- , L. F., C. S. Velden, W. E. Bracken, J. Molinari, and P. G. Black, 2000: Environmental influences on the rapid intensification of Hurricane Opal (1995) over the Gulf of Mexico. *Mon. Wea. Rev.*, **128**, 322–352.
- , J. M. Cordeira, T. J. Galarnau, B. J. Moore, and H. M. Archambault, 2012: An analysis of multiple predecessor rain events ahead of Tropical Cyclones Ike and Lowell: 10–15 September 2008. *Mon. Wea. Rev.*, **140**, 1081–1107.
- Caracena, F., R. A. Maddox, L. R. Hoxit, C. F. Chappell, 1979: Mesoanalysis of the Big Thompson storm. *Mon. Wea. Rev.*, **107**, 1–17.
- Carr, F. H., and L. F. Bosart, 1978: A diagnostic evaluation of rainfall predictability for Tropical Storm Agnes, June 1972. *Mon. Wea. Rev.*, **106**, 363–374.

- Chien, H. H., and P. J. Smith, 1977: Synoptic and kinetic energy analyses of Hurricane Camille (1969) during transit across the southeastern United States. *Mon. Wea. Rev.*, **105**, 67–77.
- Colle, B. A., 2003: Numerical simulations of the extratropical transition of Floyd (1999): Structural evolution and responsible mechanisms for heavy rainfall over the northeast United States. *Mon. Wea. Rev.*, **131**, 2905–2926.
- Cote, M. R., 2007: Predecessor rain events in advance of tropical cyclones. M.S. Thesis, Department of Earth and Atmospheric Sciences, University at Albany, State University of New York, 200 pp.
- DeLuca, D. P., 2004: The distribution of precipitation over the Northeast accompanying landfalling and transitioning tropical cyclones. M.S. Thesis, Department of Earth and Atmospheric Sciences, University at Albany, State University of New York, 178 pp.
- desJardins, M. L., K. F. Brill, and S. S. Schotz, 1991: GEMPAK 5 Part I-GEMPAK 5 programmer's guide. National Aeronautics and Space Administration, 176 pp. [Available from Scientific and Technical Information Division, Goddard Space Flight Center, Greenbelt, MD 20771.].
- DiMego, G. J., and L. F. Bosart, 1982a: The transformation of Tropical Storm Agnes into an extratropical cyclone. Part I: The observed fields and vertical motion computations. *Mon. Wea. Rev.*, **110**, 385–411.
- , and ———, 1982b: The transformation of Tropical Storm Agnes into an extratropical cyclone. Part II: Moisture, vorticity, and kinetic energy budgets. *Mon. Wea. Rev.*, **110**, 412–433.
- Dunn, G. E., W. R. Davis, and P. L. Moore, 1955: Hurricanes of 1955. *Mon. Wea. Rev.*, **83**, 315–326.
- Emanuel, K., J. Callaghan, and P. Otto, 2008: A hypothesis for the redevelopment of warm core cyclones over northern Australia. *Mon. Wea. Rev.*, **136**, 3863–3872.
- Evans, C., R. S. Schumacher, and T. J. Galarneau, 2011: Sensitivity in the overland reintensification of Tropical Cyclone Erin (2007) to near-surface soil moisture characteristics. *Mon. Wea. Rev.*, **139**, 3848–3870.
- Galarneau, T. J., Jr., L. F. Bosart, and R. S. Schumacher, 2010: Predecessor rain events ahead of tropical cyclones. *Mon. Wea. Rev.*, **138**, 3272–3297.

- Hanley, D., J. Molinari, and D. Keyser, 2001: A composite study of the interactions between tropical cyclones and upper-tropospheric troughs. *Mon. Wea. Rev.*, **129**, 2570–2584.
- , 2002: The evolution of a hurricane–trough interaction from a satellite perspective. *Wea. Forecasting*, **17**, 916–926.
- Harr, P. A., and R. L. Elsberry, 2000: Extratropical transition of tropical cyclones over the western North Pacific. Part I: Evolution of structural characteristics during the transition process. *Mon. Wea. Rev.*, **128**, 2613–2633.
- , ———, and T. F. Hogan, 2000: Extratropical transition of tropical cyclones over the western North Pacific. Part II: The impact of midlatitude circulation characteristics. *Mon. Wea. Rev.*, **128**, 2634–2653.
- Hart, R. E., 2003: A cyclone phase space derived from thermal wind and thermal asymmetry. *Mon. Wea. Rev.*, **131**, 585–616.
- Hart, R. E., J. L. Evans, and C. Evans, 2006: Synoptic composites of the extratropical transition life cycle of North Atlantic tropical cyclones: factors determining posttransition evolution. *Mon. Wea. Rev.*, **134**, 553–578.
- Hoskins, B. J., M. E. McIntyre, and A. W. Robertson, 1985: On the use and significance of isentropic potential vorticity maps. *Quart. J. Roy. Meteor. Soc.*, **111**, 877–946.
- Jones, S. C., and Coauthors, 2003: The extratropical transition of tropical cyclones: Forecast challenges, current understanding, and future directions. *Wea. Forecasting*, **18**, 1052–1092.
- Kalnay, E., and Coauthors, 1996. The NCEP/NCAR 40-year reanalysis project. *Bull. Amer. Meteor. Soc.*, **77**, 437–471.
- Kimball, S. K., and J. L. Evans, 2002: Idealized numerical simulations of hurricane–trough interaction. *Mon. Wea. Rev.*, **130**, 2210–2227.
- Kistler, R., and Coauthors, 2000: The NCEP–NCAR 50-Year Reanalysis. *Bull. Amer. Meteor. Soc.*, **82**, 247–267.
- Klein, J., 2007: Mesoscale precipitation structures accompanying landfalling and transitional tropical cyclones in the Northeast United States. M.S. Thesis, Department of Atmospheric and Environmental Sciences, University at Albany, State University of New York, 139 pp.

- Klein, P. M., P. A. Harr, and R. L. Elsberry, 2000: Extratropical transition of western North Pacific tropical cyclones: An overview and conceptual model of the transformation stage. *Wea. Forecasting*, **15**, 373–395.
- , ———, and ———, 2002: Extratropical transition of western North Pacific tropical cyclones: Midlatitude and tropical cyclone contributions to reintensification. *Mon. Wea. Rev.*, **130**, 2240–2259.
- Maddox, R. A., C. F. Chappell, L. R. Hoxit, 1979: Synoptic and meso- α scale aspects of flash flood events. *Bull. Amer. Meteor. Soc.*, **60**, 115–123.
- Martin, J. E., 2006: *Mid-latitude Atmospheric Dynamics: A First Course*. John Wiley and Sons, 336 pp.
- Miller, J. E., 1946: Cyclogenesis in the Atlantic Coastal region of the United States. *J. Meteor.*, **3**, 31–44.
- Molinari, J., and D. Vollaro, 1989: External influences on hurricane intensity. Part I: Outflow layer eddy momentum fluxes. *J. Atmos. Sci.*, **46**, 1093–1105.
- , and ———, 1990: External influences on hurricane intensity. Part II: Vertical structure and response of the hurricane vortex. *J. Atmos. Sci.*, **47**, 1902–1918.
- , J., S. Skubis, and D. Vollaro, 1995: External influences on hurricane intensity. Part III: Potential vorticity structure. *J. Atmos. Sci.*, **52**, 3593–3606.
- , ———, ———, F. Alsheimer, and H. E. Willoughby, 1998: Potential vorticity analysis of tropical cyclone intensification. *J. Atmos. Sci.*, **55**, 2632–2644.
- Monteverdi, J. P., and R. Edwards, 2010: The redevelopment of a warm-core structure in Erin: A case of inland tropical storm formation. *Electron. J. Severe Storms Meteor.*, **5** (6), 1–18.
- Moore, B. J., 2010: Synoptic-scale environments and dynamical mechanisms associated with predecessor rain events ahead of tropical cyclones. M.S. Thesis, Department of Atmospheric and Environmental Sciences, University at Albany, State University of New York, 150 pp.
- Morgan, M. C., and J. W. Nielsen-Gammon, 1998: Using tropopause maps to diagnose midlatitude weather systems. *Mon. Wea. Rev.*, **126**, 2555–2579.
- Namias, J., and C. R. Dunn, 1955: The weather and circulation of August 1955. *Mon. Wea. Rev.*, **83**, 163–170.
- Pasch, R. J., L. A. Avila, 1999: Atlantic hurricane season of 1996. *Mon. Wea. Rev.*, **127**, 581–610.

- Pasch, R. J., cited 2011: Preliminary report: Hurricane Danny (16–26 July 1997). National Hurricane Center. [Available online at <http://www.nhc.noaa.gov/1997danny.html>.]
- Rappaport, 1999: Atlantic Hurricane Season of 1997. *Mon. Wea. Rev.*, **127**, 2012–2026.
- , E. N., 2000: Loss of life in the United States associated with recent Atlantic tropical cyclones. *Bull. Amer. Meteor. Soc.*, **81**, 2065–2073.
- Rappin, E. D., M. C. Morgan, and G. J. Tripoli, 2011: The impact of outflow environment on tropical cyclone intensification and structure. *J. Atmos. Sci.*, **68**, 177–194.
- Ritchie, R. A., and R. L. Elsberry, 2003: Simulations of the extratropical transition of tropical cyclones: Contributions by the midlatitude upper-level trough to reintensification. *Mon. Wea. Rev.*, **131**, 2112–2128.
- , and ——, 2007: Simulations of the extratropical transition of tropical cyclones: phasing between the upper-level trough and tropical cyclones. *Mon. Wea. Rev.*, **135**, 862–876.
- Saha, S., and Coauthors, 2010: The NCEP Climate Forecast System Reanalysis. *Bull. Amer. Meteor. Soc.*, **91**, 1015–1057.
- Schwarz, F. K., 1970: The unprecedented rains in Virginia associated with the remnants of Hurricane Camille. *Mon. Wea. Rev.*, **98**, 851–859.
- Schumacher, C., R. A. Houze Jr., and I. Kraucunas, 2004: The tropical dynamical response to latent heating estimates derived from the TRMM precipitation radar. *J. Atmos. Sci.*, **61**, 1341–1358.
- Schumacher, R. S., and R. H. Johnson, 2005: Organization and environmental properties of extreme-rain-producing mesoscale convective systems. *Mon. Wea. Rev.*, **133**, 961–976.
- , T. J. Galarneau, and L. F. Bosart, 2011: Distant effects of a recurving tropical cyclone on rainfall in a midlatitude convective system: A high-impact predecessor rain event. *Mon. Wea. Rev.*, **139**, 650–667.
- Shen, W., I. Ginis, and R. E. Tuleya, 2002: A numerical investigation of land surface water on landfalling hurricanes. *J. Atmos. Sci.*, **59**, 789–802.
- Shi, J.-J., S. W.-J. Chang, and S. Raman, 1990: A numerical study of the outflow layer of tropical cyclones. *Mon. Wea. Rev.*, **118**, 2042–2055.

- , ——, and ——, 1997: Interaction between Hurricane Florence (1988) and an upper-tropospheric westerly trough. *J. Atmos. Sci.*, **54**, 1231–1247.
- Simpson, R. H., A. L. Sugg and Staff, 1970: The Atlantic hurricane season of 1969. *Mon. Wea. Rev.*, **98**, 293–306.
- Sinclair, M. R., 1993: A diagnostic study of the extratropical precipitation resulting from Tropical Cyclone Bola. *Mon. Wea. Rev.*, **121**, 2690–2707.
- , 2002: Extratropical transition of southwest Pacific tropical cyclones. Part I: Climatology and mean structure changes. *Mon. Wea. Rev.*, **130**, 590–609.
- , 2004: Extratropical transition of southwest Pacific tropical cyclones. Part II: Midlatitude circulation characteristics. *Mon. Wea. Rev.*, **132**, 2145–2168.
- Srock, A. F., and L. F. Bosart, 2009: Heavy precipitation associated with southern Appalachian cold-air damming and Carolina coastal frontogenesis in advance of weak landfalling Tropical Storm Marco (1990). *Mon. Wea. Rev.*, **137**, 2448–2470.
- Uccellini, L. W., and P. J. Kocin, 1987: The interaction of jet streak circulations during heavy snow events along the east coast of the United States. *Wea. Forecasting*, **2**, 289–308.
- Uppala, S. M., and Coauthors, 2005: The ERA-40 Re-Analysis. *Quart. J. Roy. Meteor. Soc.*, **131**, 2961–3012.
- Yu, H., and H. J. Kwon, 2005: Effect of tc–trough interaction on the intensity change of two typhoons. *Wea. Forecasting*, **20**, 199–211.